5

Geodetic Observations of Tectonic Deformation in Alaska and Western Canada: The EarthScope Revolution

Julie Elliott[1], Jeffrey T. Freymueller[1], and Ronni Grapenthin[2]

ABSTRACT

The number of GPS sites in Alaska and western Canada has exploded over the past 15 years, largely due to the PBO/NOTA stations installed as part of the NSF-funded EarthScope project. This expanded geodetic data set has provided an unprecedented view of deformation along the north Pacific margin. The entire region moves in ways distinct from stable North America. Long-term motion of the upper plate includes northwestward motion in southeast Alaska and the St. Elias region, a clockwise rotation from the southeast Alaska coast into the Northern Cordillera of Canada, a series of counterclockwise rotations south of the Denali Fault, and southerly motion in northern Alaska. Geodetically determined coupling along the subduction interface varies greatly, with correlations between past earthquakes, areas of high and moderate coupling, and lateral coupling boundaries. GPS data from a number of large earthquakes have captured complex slip patterns, evolution of slip during events, and interactions between earthquakes. Postseismic deformation from several large earthquakes, including the 1964 M9.2 Great Alaska and the 2002 M7.9 Denali earthquakes, is ongoing. Transient slow slip events along the subduction interface may accommodate part or most of the slip budget in areas of partial coupling.

5.1. INTRODUCTION

Surface deformation in Alaska and western Canada is highly variable and complex, far-reaching, and driven by a number of different tectonic and nontectonic processes. Deformation contributors include major plate boundary faults in southern Alaska, other fault networks that transfer and accommodate relative plate motion far inboard of the main plate boundary, and expansive glacier systems experiencing substantial change (Figure 5.1). This active natural laboratory has long been a target for geodetic measurements, from terrestrial triangulation networks beginning in the early 1980s (e.g., Lisowski et al., 1987;

[1]Department of Earth and Environmental Sciences, Michigan State University, East Lansing, MI, USA
[2]Geophysical Institute and Department of Geosciences, University of Alaska Fairbanks, Fairbanks, AK, USA

Savage et al., 1981), to Very Long Base Interferometry (VLBI) starting in the early 1980s (e.g., Ma et al., 1990), and the Global Positioning System (GPS) starting with the first survey conducted by the National Geodetic Survey in 1984. GPS surveys and sites rapidly expanded throughout the 1990s and 2000s, revealing new information about large-scale tectonic motions, fault slip rates, deformation during the various parts of the earthquake cycle, and nontectonic processes such as glacial isostatic adjustment (GIA) as detailed in a summary of geodetic studies 15 years ago (Freymueller et al., 2008).

Over the past 15 years since that study, the quantity and quality of geodetic measurements in Alaska has greatly increased. New networks of both campaign and continuous GPS sites have been installed and generated mature data sets. The enhanced spatial coverage of these sites has allowed both opportunities for broad, synoptic studies and more detailed evaluations of plate motions, slip
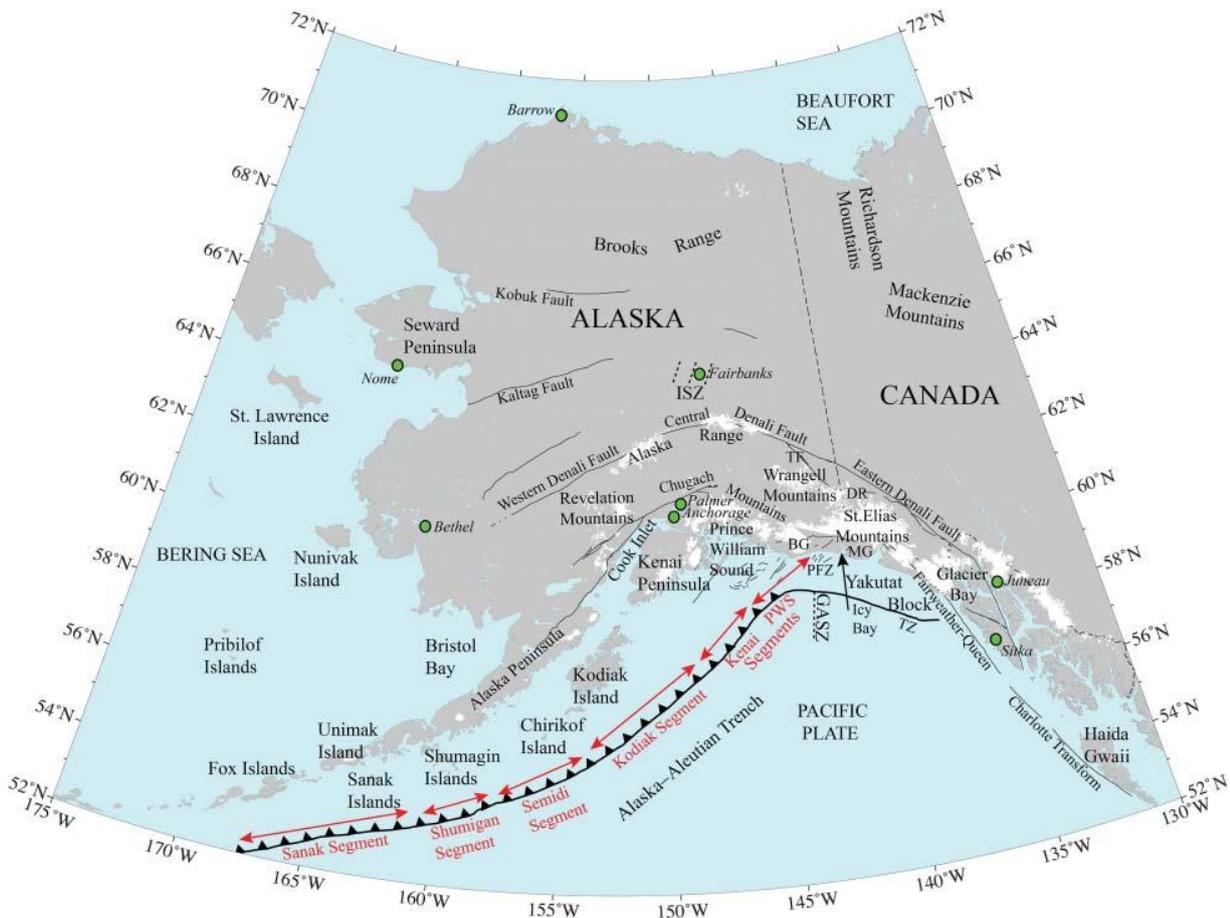
Figure 5.1 Tectonic Setting for Alaska and Western Canada. PFZ, Pamplona Fault Zone; TF, Totschunda Fault; MG, Malaspina Glacier; DR, Duke River fault; GSZ, Gulf of Alaska Shear Zone; TZ, Transition fault; ISZ, interior seismic zones. Red arrows and text demark different segments of the Alaska–Aleutian subduction zone. The area labeled Yakutat block marks out the portion of that block that has not been subducted.

rates on faults, and distributed deformation. Increased temporal coverage from continuously operating GPS sites (cGPS) has enabled precise characterization of slip during earthquakes and more thorough characterization of time-variable tectonic phenomena such as slow slip events (SSEs) and postseismic deformation. Long, in some cases, multidecadal, time series allow the investigation of signals such as seasonal snow loading and the evaluation of the different processes contributing to the observed deformation.

In this study, we explore in detail the changes in the geodetic data and processing and what these new data sets have taught us about active tectonic processes in Alaska and western Canada. After discussing the changes in networks and processing techniques, we outline the various contributing signals typically found in Alaska geodetic data and strategies for isolating a desired target signal. Major findings over the past 15 years about

steady-state tectonic motion, earthquakes (both recent and re-evaluations of past events), postseismic deformation, transient slow slip events along the subduction interface, and geodynamics in Alaska are summarized. Finally, we discuss the implications of these results for Alaska tectonics and highlight developing data sets and techniques that will likely lead to more exciting geodetic discoveries over the next 15 years.

5.2. GEODETIC SITES AND NETWORKS IN ALASKA

The state of geodetic data and infrastructure has changed dramatically over the past 15 years. At the time of the publication of the previous AGU monograph (Freymueller et al., 2008), most of the GPS data was collected episodically at campaign sites. The number of cGPS was less than three dozen. Large areas of Alaska had very sparse or no campaign or continuous GPS
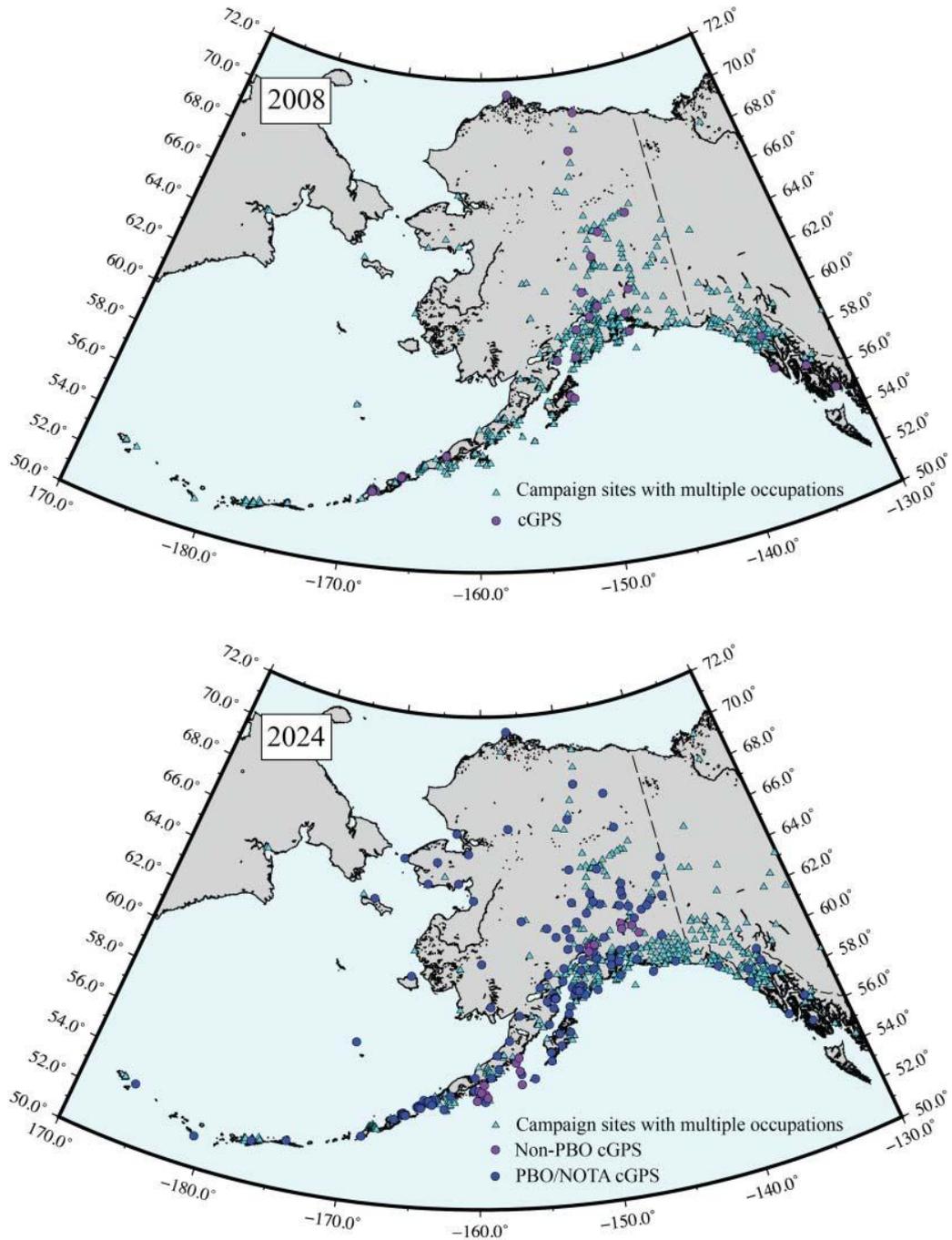
Figure 5.2 Comparison between GPS/GNSS sites in 2008 at the time Freymueller et al. (2008) was published and the present day.

sites at all (Figure 5.2). While the continuous sites of the Plate Boundary Observatory (PBO, now Network of the Americas or NOTA) had begun to be installed in 2004 as part of the EarthScope project (funded by the National Science Foundation), the data time series at most sites were too short (<2–3 years) to produce reliable

steady-state velocities by the time that study's data set was finalized.

When the network installation was completed in 2008, the PBO/NOTA network in Alaska contained almost 150 cGPS, and the majority of sites remain in operation. The network increased station density in southcentral,

southeast, and interior Alaska as well as along the Alaska Peninsula and the Aleutian Islands (Figure 5.2). New stations were installed in previously uninstrumented regions in western and northern Alaska. In addition to the PBO/NOTA network, other research projects (primarily focused on long-term tectonics, earthquake-related deformation, and GIA) added new cGPS sites in the Wrangell Mountains and Copper River Valley, the Matanuska-Susitna Valley, the Shumagin and Semidi Islands, and the Mackenzie Mountains. The number of cGPS sites in Alaska will be continuing to expand, as the state is planning its own network (Alaska Continuously Operating Reference Network, ACORN). The number of both new campaign (or episodic) sites and occupations at existing campaign sites also significantly increased over the past 15 years. Campaign sites have only a permanent benchmark, and GPS equipment is typically set up to collect data over the benchmark for a few days each year or every few years. The main drivers of the new campaign data have been individual and collaborative research projects funded by a variety of entities including the National Science Foundation, the Geological Survey of Canada, the University of Victoria, Michigan State University, the University of Alaska Fairbanks, and Purdue University. These projects investigated long-term tectonic motions (including in the Mackenize and the Chugach-St. Elias Mountains), earthquakes (including the 2018 M7.1 Anchorage, 2020 M7.8 Simeonof, and 2021 M8.2 Chignik earthquakes), postseismic deformation (including from the 2002 M7.9 Denali earthquake as well as from the Anchorage, Simeonof, and Chignik earthquakes), and GIA.

As the networks have expanded, navigation satellite constellations and hardware developments have also undergone significant changes. GPS, while often used as a generic term for satellite navigation systems, refers to the U.S. operated navigation satellite system. Other systems are now operational, including GLONASS (Russia), Beidou (China), and Galileo (European Union), which along with GPS are collectively referred to as "Global Navigation Satellite Systems" (GNSS), and modern GNSS equipment can receive and record signals from multiple satellite constellations. In the case of the results discussed below, however, the vast majority of the data is GPS only. For this reason, we use GPS rather than the more broadly encompassing term GNSS. Another recent, major advance is the advent of seafloor or acoustic GPS/GNSS systems. These systems, consisting of acoustic transponders installed on the seafloor and receivers and antennas that are episodically positioned over the transponders at the sea surface, are capable of ~ centimeter level accuracy (e.g., Chadwell & Spiess, 2008). While this is an order of magnitude lower accuracy than land-based GPS measurements, the acoustic systems can provide invaluable information in the offshore regions of subduction zones and transform fault systems. The first three acoustic sites in Alaska were installed offshore the Alaska Peninsula in 2018, and measurements were taken several times between 2018 and 2021 (Brooks et al., 2023; DeSanto et al., 2023). A new community experiment will install several additional sites offshore the Alaska Peninsula starting in 2024.

Data from both the cGPS and the campaign sites play critical roles in evaluating deformation in Alaska. Campaign sites require only a benchmark as infrastructure, making them an economical way to densify sites in a region or making sites possible in areas in which permitting for more permanent structures may be difficult. Episodic data from campaign sites is valuable for determining long-term steady-state motions, earthquake offsets, longer-term postseismic signals, GIA, and longer-term uplift and subsidence signals. cGPS requires additional infrastructure (including antenna mounts, enclosures, power systems, and ideally communications), but their daily or subdaily positioning capabilities allow the investigation of short-lived or rapidly varying signals (such as seasonal hydrologic loading, slip developing during earthquakes, or rapid postseismic deformation) in addition to the signals captured by the episodic campaign measurements. The combination of the campaign and cGPS sites provides both spatial and temporal measurement densities. The new results enabled by the expanded networks shown in Figure 5.2 are discussed below.

5.3. A BRIEF HISTORY OF UAF/MSU GPS DATA ANALYSIS

Almost all results described or shown in this chapter come from the GPS time series analyzed at the University of Alaska Fairbanks and Michigan State University over the past 28 years. Data analysis methods have evolved considerably over that time, so this section updates the description of data analysis presented in Freymueller et al. (2008). In this section, we summarize the current approach and briefly discuss how the older analysis results that appear in the cited papers differ. Over time, we used different versions of the NASA/JPL GIPSY/OASIS data analysis package (Bertiger et al., 2010; Zumberge et al., 1997). In all cases, daily position solutions were estimated, with all data from a given UTC day being combined to estimate a single position for each site, and all solutions were aligned to the International Terrestrial Reference Frame (ITRF) (e.g., Altamimi et al., 2016), with the version of ITRF used changing over time. Displacements or velocities were then estimated from those daily position time series. The methods used to estimate displacements or velocities have changed very little over time, being standard least-squares methods.

Since about 2010, all of our published results (with rare exceptions) have used the precise point positioning (PPP) method, in which satellite orbit and clock parameters from a global solution are held fixed, and each individual site is processed one at a time. This method is highly scalable and allows large networks of sites to be analyzed. Older work used network solutions, in which a regional group of sites are processed together each day, in a single estimation step. Network solutions are computationally burdensome for large numbers of sites due to the computational time needed to invert the very large matrices involved.

The different analysis approaches over time have been given (internal) version numbers, which are referenced below. In general, estimated site velocities changed very little from version to version, except for unusual cases where sites had very few observations, used unusual antennas, or antenna calibrations changed. However, the noise level of the solutions decreased substantially with each version, so the displacement and velocity uncertainties have tended to decrease with each reanalysis.

All individual daily solutions are aligned to the ITRF (ITRF2014 [Altamimi et al., 2016] for the current solutions). The frame alignment involves using the ITRF coordinate model to compute the position of all sites in the ITRF model for the day in question and then computing a seven-parameter similarity transformation (translation, rotation, and scale) to align our (frame-free) solution to the ITRF. Over time, accumulating forward projection error, earthquakes, antenna changes, and other events or offsets invalidate the ITRF coordinate model for certain sites. Therefore, we maintain a time-dependent list of the sites that should be used to compute the transformation.

5.3.1. Current Analysis (Version 4, 2020 to Present)

The current analysis uses the goa-6.4 version of GIPSY and the second Jet Propulsion Laboratory (JPL) reprocessed set of orbit and clock products (IGS repro2) for the International GNSS Service (IGS) for 1995–2014, along with the current JPL operational products for all later times. We apply correction models for subdaily displacements due to solid earth tides and ocean tidal loading. Models for atmospheric loading are not currently removed. Loading models are computed in the center of mass of Earth System (CM) frame, which is the center of mass of the solid Earth plus all fluids and atmosphere. We apply the second-order ionospheric correction, using the IGS Final IONEX file as the daily ionospheric model. We apply azimuth and elevation-dependent antenna phase center corrections and estimate the site position, receiver clock error, and atmospheric delay.

The antenna phase center models are azimuth and elevation-dependent models, based on the IGS14 phase center models (Rebischung & Schmid, 2016; https://files.igs.org/pub/station/general/igs14.atx), augmented by models published by the National Geodetic Survey for non-IGS antennas. The IGS14 models include many more antenna types than older models and are overall more self-consistent. These models also differ in scale from the IGS08 models, part of an iterative process to measure an accurate scale for GPS positioning. The issues with the definition of scale result from the fact that the GPS spacecraft antennas had no published calibrations from before launch and thus had to be empirically estimated given an assumed set of ground antenna calibrations.

We model atmospheric path delays using the VMF1GRID wet and dry tropospheric path delays and mapping functions provided by TU Wien (Böhm et al., 2006). VMF1GRID values are provided on a 2° × 2° global grid each day based on ECMWF global weather models, and these are interpolated to each site's location accounting for site elevation above the ellipsoid. We apply the VMF1GRID a priori values for both wet and dry troposphere zenith delays and the day- and location-specific mapping function. We then estimate a correction to the wet delay that includes the time-varying value at zenith and a constant gradient with azimuth.

After estimating point positioning solutions for all sites of interest, locally and global, we construct a global solution by concatenating coordinate solutions for all sites. This includes the globally distributed sites that are included in the ITRF2014 coordinate model, which are primarily used for the frame alignment. Global solutions are then aligned to ITRF2014 as described above. Our software also has the capability to define one or more regional subsets of sites. In older work using the version 3 solutions, the results always came from these regional subsets, but in the version 4 solutions we use the full global set.

5.3.2. Older Point Positioning Methods (Version 3, ~2010–2020)

In most respects, our older point positioning solutions (Fu & Freymueller, 2012; Fu et al., 2012) were done in largely the same way as the current analyses. Those solutions used an older version of the GIPSY software, goa-5.1 (Zumberge et al., 1997), which lacked a few important modeling capabilities present in goa-6.4. The two most important differences are that the older solutions did not use single-station ambiguity resolution (Bertiger et al., 2010) as in the current version 4 solutions, and the older version 3 solutions used the Global Pressure and Temperature (GPT) model (Böhm et al., 2007) for tropospheric mapping functions and a priori parameter

values rather than VMF1GRID. GPT is a seasonalized average of VMF1, but the VMFGRID model currently used is significantly better, and results in about a 25% reduction in the short-term scatter of vertical positions. The older version 3 solutions also lacked second-order ionospheric corrections, but this makes only a very small improvement to the current solutions. The version 3 solutions used the JPL-reprocessed set of orbit and clock products (now called "IGS repro1") for 1996–2008, along with the JPL operational products for all later times. The repro1 campaign was the first systematic reprocessing of all IGS data with updated models, and the orbit and clock products were substantially improved and more self-consistent over the older operational products. The daily solutions were aligned to the ITRF2008 realization of ITRF, which was the current version at that time.

The antenna phase center models applied azimuth and elevation-dependent corrections, based on the IGS08 phase center models or models published by the National Geodetic Survey for non-IGS antennas. These phase center models are "absolute" models although based on assumed values for the transmitter phase center variations.

5.3.3. Network Solutions (Version 2, 2002–2010)

The network solution strategy used prior to about 2010 was also based on GIPSY goa-5.1 software, but with a set of up to 250 sites processed together in a single network solution. The network solution included all sites within Alaska, plus all IGS sites within ~4000 km of Alaska. After the construction of the Plate Boundary Observatory network, the continued use of network solutions became impractical due to the large number of sites present. This set of solutions used orbits from the JPL operational submission to the IGS for all dates. As a result, there were changes over time in the orbit quality as models and JPL's analysis center procedures were improved. Because these were network solutions, we did not use the JPL clock solutions but instead estimated the satellite clock errors.

The network solution strategy was more fully described in Freymueller et al. (2008). In network solutions, the clock at one site must be held fixed as a reference clock, and all estimated clock errors are relative to that clock's value. The specific site chosen does not matter too much as long as its clock is well behaved, but receivers such as Trimble receivers that include millisecond offsets in their clock to account for drift cannot be used as a reference clock. Typically, we used the site ALGO (Algonquin Park, Canada) because it had an ultrastable clock. Those solutions were aligned to either the ITRF2000 or ITRF2005 reference frames, depending on the date each given study was done, although all work always referenced all solutions to the same frame. The network

solutions used ocean tidal loading models computed using the TPXO.2 ocean tidal model, in the center of mass of solid Earth frame.

Antenna phase center corrections were applied using the IGS05 calibration models or models published by the National Geodetic Survey for non-IGS antennas. These models did not correct for azimuthal variations, only variations with elevation angle. These calibrations were based on relative antenna elevation models, in which the Dorn-Margolin with choke ring antenna was taken as the reference for all phase center models, and thus had zero elevation-dependent variation. An error in applying the antenna phase center models was present in this solution series and was discovered and corrected in preparing for the version 3 solution series (the elevation angle and angle from nadir were accidentally swapped). This caused biases in the computed site positions but had little impact on displacements or velocities except in the case of a few unusual antennas with large elevation-dependent corrections.

5.3.4. Estimating Velocities and Displacements

Each previously published study described how velocities and displacements were computed from the time series, in varying detail. The general process is described in this section, and the methods used in individual studies can be assumed to reflect this description except as noted in any individual paper.

Currently, velocities are estimated on a site-by-site basis (independently). We first extract all solutions for a given site from our complete set of global solutions and store these values in a site time series file using software written in MATLAB. We do not apply a regional filter for common mode errors for velocity solutions but do apply such a filter for estimating displacements from smaller earthquakes. The velocities are estimated along with other parameters in a standard least-squares solution, assuming a colored noise model (Mao et al., 1999) for the time correlations in the data. Additional parameters include the position at a reference time and optionally may include seasonal (annual and semi-annual) terms, offsets for antenna changes or earthquakes, and postseismic transient terms (exponential and/or logarithmic relaxation). For large earthquakes, we have typically based velocities on only the pre-earthquake data rather than trying to fit both the pre-earthquake and the postseismic time series accurately.

We build a data covariance matrix by scaling the formal uncertainties from the position solution (variance scaled by a factor of 3) and adding flicker noise of an uncertainty of 1 mm for the horizontal components and 2 mm for the vertical. The default variance scaling is based on the typical short-term (day-to-day) repeatability of

coordinate estimates, and the flicker noise uncertainties are based on typical values from a noise analysis of many sites. After the model fit, the final parameter variance is rescaled so that the reduced chi-square statistic is equal to 1. This rescales both components of the noise model by the same value. Older estimates did not use colored noise but compensated for the time-correlated errors by adding an additive uncertainty proportional to $1/T$, where T is the total time span of data for the site. In practice, the use of a white noise or colored noise model for episodic campaign data gives almost the same results, but the velocity and other parameter uncertainties for continuous sites are much more realistic when a colored noise model is used.

New coseismic displacements presented here are based on the difference between the pre- and post-earthquake positions in ITRF. For each earthquake, we averaged the 5 days prior to the earthquake to get the pre-earthquake position and the 5 days after to get the post-earthquake position. This strategy is appropriate for continuous sites. The solutions on the day of the earthquake were not used. We scaled the uncertainties of each of the pre- and post-earthquake positions so that the reduced chi-square of the 5-day average would be equal to 1; this is assessed over the whole network considered. The post-earthquake positions likely include some postseismic deformation. The choice of a 5-day average reflects a trade-off between improved noise reduction by averaging against some early postseismic deformation leaking into the coseismic displacements. In some cases (e.g., Hreinsdóttir et al., 2006), we have instead fit a linear trend plus offset (and potentially postseismic terms) to the time series to compute a coseismic displacement that does not include any postseismic deformation or to allow inclusion of data from sites (like campaign sites) that were not recording right at the time of the earthquake. Among the earthquakes presented in this chapter, only the October 2020 M7.2 Sand Point earthquake was treated this way due to the fact that it occurred within the middle of an ongoing postseismic transient.

For the new results shown below, we extracted a subset of our global solution that includes all sites within 1,500–2,500 km from each earthquake, depending on its magnitude. The pre- and post-earthquake solutions with scaled errors were differenced to get the displacements and their covariance matrix. For some of the smaller earthquakes, we applied an additional local reference frame stabilization step. In this step, we first extracted all sites within our initial subset that were far enough from the event to have zero displacement. We averaged the pre- and post-earthquake positions for those sites only and re-aligned each daily solution with those average coordinates. We then recomputed the pre- and post-earthquake solutions from the stabilized solutions and computed the displacements. The difference between the stabilized and original globally aligned solutions was negligible for the horizontal components, but biases in the vertical are smaller after stabilization. We hypothesize that the stabilization is mainly compensating for unmodeled time-dependent loading, likely atmospheric pressure loading.

5.3.5. North American Reference Frame

Velocities and displacements are computed (above) in the ITRF, reflecting the underlying reference frame definition of the solutions. By convention, the ITRF is defined such that there is no net rotation of the lithosphere due to ongoing plate motions (Altamimi et al., 2007). This is a geologically arbitrary definition but one that can be precisely defined and accurately computed. To analyze tectonic motions relative to a plate, we must estimate the motion of the plate in ITRF or use such an estimate from a previous study. We subtract the predicted motion of North America (Argus et al., 2010) from the estimated ITRF velocities, which results in velocities relative to the North American plate that we can use for modeling tectonic processes. We add an uncertainty to the velocity relative to North America that reflects the uncertainty in the definition of North America. Currently that uncertainty is ~1 mm/year, but in our pre-2010 network solutions, it was 2–3 mm/year (Freymueller et al., 2008). In the case of abrupt displacements (e.g., earthquakes), we can simply use displacements computed in ITRF directly because the displacement of North America relative to ITRF is negligible over time periods of a few days or even a few weeks.

In the case of the North American plate, the plate motion estimate is complicated by the combination of broad tectonic deformation over the western part of the continent and GIA deforming the eastern part of the continent (Ding et al., 2019; Kreemer et al., 2018). Although the GIA strains are small, they are nonzero and ignoring the horizontal motion due to GIA causes biases in the estimated plate motion, with the bias varying with the choice of sites used to define the plate. As a result, different estimates of North America motion can result in motion differences that can reach the level of 1–3 mm/year over Alaska. In most of our published results over the past several years, we adopted the estimate of the motion of North America from the GEODVEL model of Argus et al. (2010), updated to the ITRF2014 frame. The difference between ITRF and a North America fixed frame is a rotation about an axis that passes through the Earth surface offshore of Ecuador so that the motion of stable North America in ITRF shows a broad counterclockwise rotation. The GEODVEL model also includes a small frame origin shift, with the most recent estimate being that the center of plate rotation is moving at a rate of

~0.6 mm/year relative to the center of mass of Earth system (Argus et al., 2014). Ding et al. (2019) showed that this frame origin shift, in combination with GIA horizontal motions (Peltier et al., 2015), can explain the observed strain across eastern North America.

5.4. SIGNALS IN GPS DATA

Alaska's extremely active and complex geologic environment, which includes active tectonics, volcanism, and current and past cryosphere change, results in a superposition of signals in geodetic observations. We briefly discuss the signals that are most influential in Alaska, how they impact the geodetic data and can influence data interpretation, and strategies to isolate target signals in the data.

5.4.1. Tectonic Signals

Tectonic signals can be broadly divided into those related to earthquake cycle deformation and those related to transient tectonic deformation, although some behavior crosses boundaries and cannot be neatly categorized. The simplest version of an earthquake cycle model consists of the interseismic, coseismic, and postseismic phases (e.g., Scholz, 2002; Figure 5.3). The interseismic phase is characterized by steady-state or linear motion over time periods of decades or centuries depending on the region or individual fault. During the interseismic phase, the sides of a fault will be locked, or stuck together, due to frictional forces while the crustal blocks on either side of the fault continue to move. This results in the accumulation of stress and strain. Eventually, the frictional forces along the fault are exceeded, and the coseismic phase begins as the fault abruptly slips in an earthquake. The coseismic slip on a fault loads stress onto the crust and mantle which in turns leads to the postseismic phase. During the postseismic phase, stress imposed by the earthquake may be released through afterslip along the fault plane, poroelastic deformation, or viscoelastic relaxation of the ductile lower crust and upper mantle (e.g., Bürgmann & Thatcher, 2013). Postseismic deformation is time-dependent and nonlinear and may last months to decades (and in rarer cases, a century or more) depending on the local material properties of the solid Earth and the characteristics of the earthquake (e.g., Bürgmann & Dresen, 2008). During the postseismic phase, the fault becomes frictionally locked again, and strain begins accumulating toward the next earthquake. Eventually, the nonlinear postseismic signals decay to an insignificant rate, steady-state motion resumes, and a new interseismic phase begins.

Transient tectonic signals, such as SSEs along subduction interfaces, do not fit neatly within the simple model of the earthquake cycle. Slow slip events release strain over a period of days to years instead of seconds to minutes. Characteristics of the SSEs, including duration, depth, reoccurrence interval, and size, vary by location, but SSEs appear to primarily occur within areas of the fault plane that are not strongly locked (e.g., Bartlow et al., 2021). Multiple SSEs have been recorded along the Alaska subduction zone and are discussed in detail below.

5.4.2. Nontectonic Signals

Geodetic data often also contain nontectonic signals. In Alaska and western Canada, the most impactful of these signals are GIA, seasonal hydrologic loading, and volcano deformation. Glacial isostatic adjustment is the response of the solid Earth to changing ice loads, including an immediate elastic response and a longer-term viscoelastic response if the change in ice mass is large. Although GIA produces the largest signals in the vertical component, significant horizontal deformation is also possible and can bias tectonic interpretations (e.g., Larsen et al., 2005; Kreemer et al., 2018). In Alaska and Canada, the loss of the Laurentide and Cordilleran ice sheets since the Last Glacial Maximum produces vertical signals (dominantly subsidence) of 1–3 mm/year (DeGrandpre & Freymueller, 2019; Peltier et al., 2015). The largest ongoing GIA signals in the region are along the Gulf of
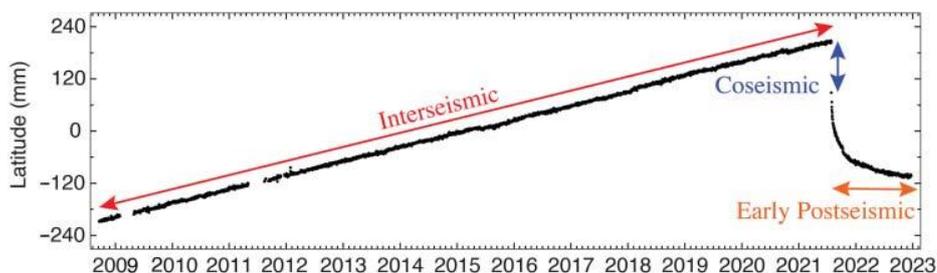

Figure 5.3 North–South component of GPS time series for site AC13 on Chirikof Island (Figure 5.1), illustrating how deformation during different phases of the earthquake cycle is recorded in geodetic data. The horizontal axis is shown as years.
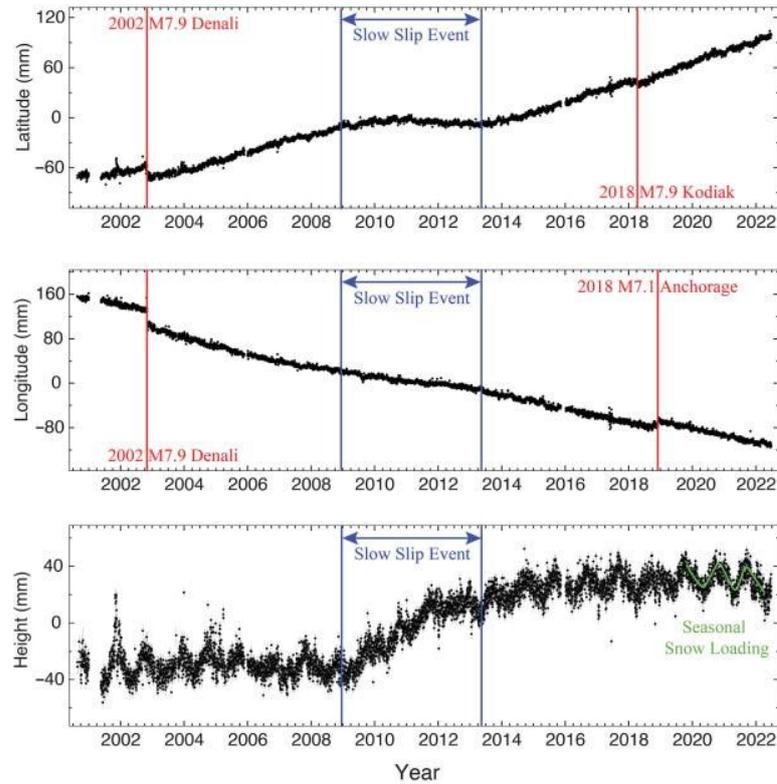
Figure 5.4 Time series for site ATW2 in Palmer, Alaska (Figure 5.1), showing different sources of signal at a single site. Latitude shows north–south motion with north being positive. Longitude shows east–west motion with east being positive. Each dot represents a daily averaged position.

Alaska coast (especially southeast Alaska) and are due to the massive ice loss since the end of the Little Age less than 300 years ago. In southeast Alaska, GIA produces uplift rates of 30–35 mm/year and horizontal rates of >5 mm/year (Elliott et al., 2010; Larsen et al., 2005). Over the past two decades, time-varying GIA signals have been observed in GPS data as ice loss in the region has accelerated (Hu & Freymueller, 2019).

Seasonal deformation due to hydrologic loading is widespread across the region and is particularly important in areas that receive heavy snow (Figure 5.4). The hydrologic seasonal signals primarily not only occur in the vertical component of the signal but can also impact the horizontal signals. Permafrost change can also produce signals in the GPS data. Liu and Larson (2018) documented seasonal freeze–thaw cycles in permafrost at a continuous GPS site along the Arctic Alaska coast. The influence of permafrost signal on GPS data may increase as warming continues.

Volcano-related deformation due to crustal magma transfer, eruptive activity, or surface processes is generally constrained to the vicinity of the volcano. Surface deformation patterns depend on the depth and volume of the magmatic activity and the shape of the magma reservoir (e.g., Segall, 2010; Sigmundsson et al., 2018). Episodes of magma intrusion are generally accompanied by horizontal motion directed away from the volcano and uplift while eruptions generally result in a revered pattern. Alaska's frequent volcanic activity and large number of volcanoes means that signals may be present in data at a significant number of GPS sites along the subduction zone boundary (Figures 5.1 and 5.2). During the 2009 Redoubt eruption, pre- and co-eruptive deformation of about 1 cm was observed at a GPS site almost 30 km from the vent (Grapenthin et al., 2013). Expanded geodetic data sets have shown that volcano deformation is rarely constant during or between eruptions. Okmok Caldera in the central Aleutian Islands is a textbook example of pulsing behavior that is modulated onto relatively steady inflation since its 2008 eruption (e.g., Xue et al., 2020).

5.4.3. Signal Superposition in GPS Data

Given the high rate of geological activity in Alaska, GPS sites are likely to contain a number of different signals including the possibility of multiple earthquakes

and transient events. Interpretating such data requires a careful evaluation of the data set and strategies for isolating the signal or signals desired. Failing to fully evaluate possible signals in the data and account for them can result in severe biases in models and interpretations. A site in Palmer, Alaska, located over the subduction interface, shows some of the complexity that can occur in a GPS time series (Figure 5.4). This site has several long-wavelength signals including interseismic deformation, postseismic deformation from the 1964 earthquake, and GIA. Offsets from the 2002 M7.9 Denali, 2018 M7.9 Offshore Kodiak, and 2018 M7.1 Anchorage earthquakes are readily apparent in the time series, and there is also some degree of postseismic deformation from these events. An SSE in upper Cook Inlet strongly impacted the time series from 2009 to 2013, especially in the North–South (latitude) and vertical components. Seasonal signals, largely due to snow loading, cause the vertical signal to oscillate by more than 20 mm.

In Alaska and western Canada, strategies for isolating a desired target signal vary depending on the signal in question. For the case of the long-term interseismic signal, multiple strategies are involved. As discussed above, earthquake offsets and periodic seasonal signals can be addressed during processing. When available, models can be applied to account for signals such as postseismic deformation from the 1964 earthquake and GIA. No model yet exists that can explain all of the postseismic deformation observed after the 2002 Denali earthquake, so in some regions an empirical correction for the postseismic deformation is applied to the data (Elliott et al., 2013) while in other areas (such as near the fault) data is limited to that collected before the earthquake. In southeast Alaska, we only use data collected before October 2012 to avoid the overlapping coseismic and postseismic effects of the 2012 M7.8 Haida Gwaii and 2013 M7.5 Craig earthquakes. In some areas around Cook Inlet, data from some sites are entirely excluded as SSEs that are difficult to model and remove impact the majority of the time series. Moving forward, GPS data along the Alaska Peninsula will need to be limited to pre-July 2020 time periods to avoid the overlapping coseismic and postseismic signals from the M7.8 2020 Simeonof and M7.6 Sand Point earthquakes and the 2021 M8.2 Chignik earthquake. Signals due to volcanic activity can be removed through the use of deformation models if they exist or by exclusion of data impacted by magmatic processes.

5.5. EARTHQUAKE CYCLE DEFORMATION

Much of the deformation observed in Alaska is due to earthquake cycle deformation. In the sections below, we discuss how the expanded geodetic data coverage in Alaska and western Canada has provided new insights into these processes.

5.5.1. Interseismic Deformation

Interseismic tectonic signals in the GPS data can be evaluated and modeled in a variety of ways including investigating deformation across individual fault strands, analysis of strain fields, and block modeling. Block modeling simultaneously estimates slip rates on faults and block rotations and thus avoids possible kinematic inconsistencies over larger regions. The exact block modeling scheme varies depending on the software used, but the general method assumes that the interseismic velocity at a GPS site is due to a combination of block motion and elastic effects from strain accumulation along block bounding faults. The block motion is dependent on the GPS site location. The elastic effects depend on the site location, fault geometry, and fault slip rate. The block motion and elastic effects can be described in terms of the block angular velocity, Ω:

$$\vec{d} = (\vec{v}_{\text{Block}} - \vec{v}_{\text{Elastic}}) = \mathbf{R}\vec{\Omega}$$

where $\vec{d}$ is the GPS data vector, and the block motion and elastic effects have been combined into a single term $\mathbf{R}$. A weighted least-squares inversion is then used to solve for the block angular velocities. Details on the particular modeling schemes used in the results discussed below can be found in Elliott et al. (2010, 2013) and McCaffrey (2002).

Isolating the interseismic signal in GPS data can be challenging given other tectonic and nontectonic signals discussed above and requires the use of both models of nonsteady-state signals and exclusion of data that contain signals with particularly complex signals. Interseismic deformation (Figure 5.5) is discussed by region in the sections below.

Southeast Alaska and the St. Elias Orogen

The southeastern Alaska panhandle and the St. Elias orogen of Alaska and Canada contain the transition from a translational margin with a rapidly moving transform fault to a collisional margin that accommodates several cm/year of convergence, and the GPS velocity field reflects this complexity (Figures 5.5 and 5.6). Previous geodetic studies in southeast Alaska relied on small geodetic networks and were limited in scope. The expanded number of campaign and continuous sites (Figure 5.2) have allowed more detailed evaluations through the use of block models and the analysis of strain fields (Elliott & Freymueller, 2020a; Elliott et al., 2010, 2013; Marechal et al., 2015).

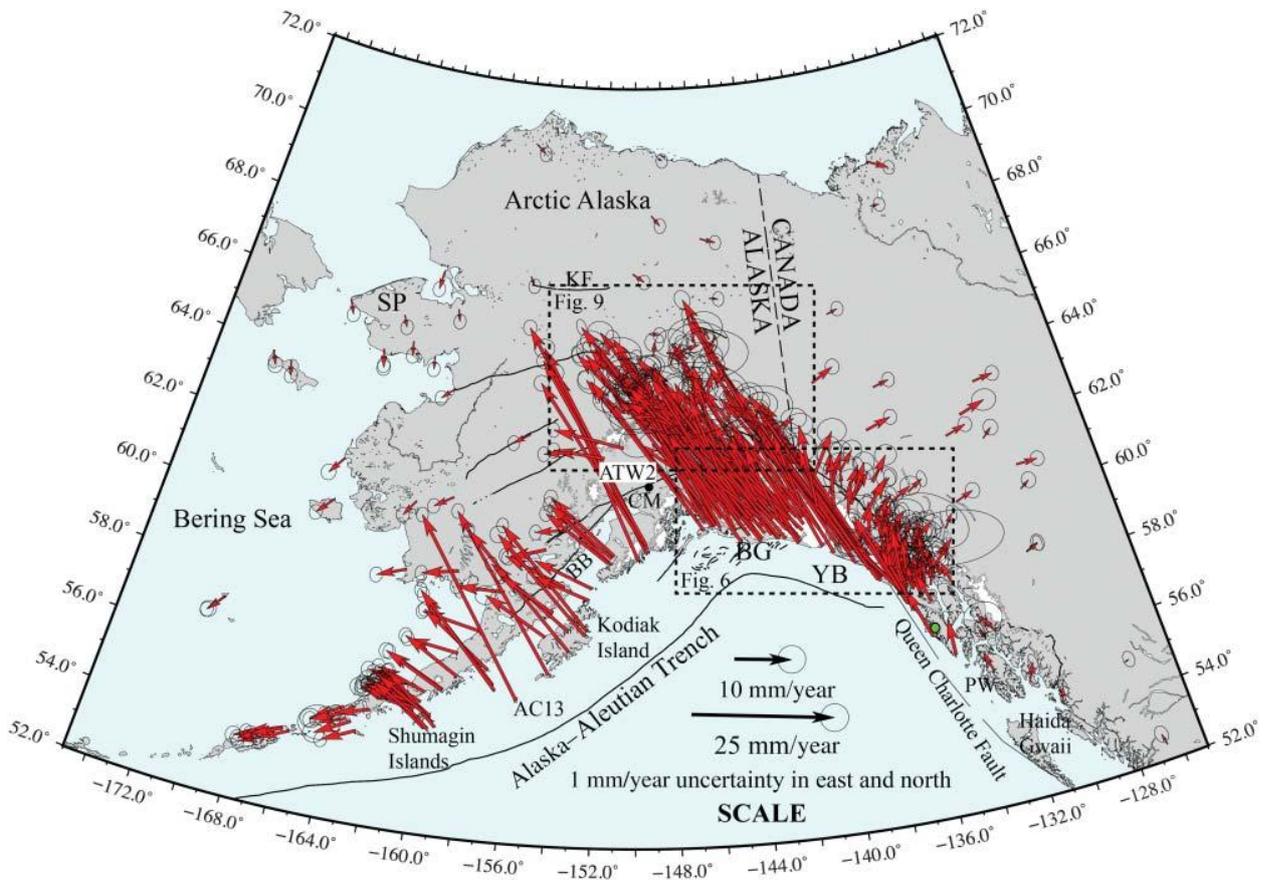South of Glacier Bay, the margin is dominantly translational, with GPS velocities that are parallel to the

Figure 5.5 Interseismic velocities are from Elliott and Freymueller (2020a) and Drooff and Freymueller (2021) (in the Shumagin region only). Velocities are relative to the GEODVEL estimate of North America motion (Argus et al., 2010) and have had estimates of glacial isostatic adjustment and postseismic relaxation from the M9.2 1964 earthquake removed. An empirical correction for postseismic deformation from the 2002 M7.9 Denali earthquake has been applied at far field sites in the Chugach-St. Elias region (Elliott et al., 2013) while sites closer to the fault only use pre-earthquake data. SP, Seward Peninsula; BG, Bering Glacier; KF, Kaltag fault; YB, Yakutat block; PW is Prince of Wales Island. The green dot marks the location of Sitka. AC13 is the site shown in Figure 5.3, and ATW2 is the site shown in Figure 5.4. Dashed line boxes show extent of areas shown in Figures 5.6 and 5.9. CM; Castle Mountain fault and BB; Bruin Bay fault.

coastline and largest near the coast and the Queen Charlotte fault. Margin parallel motion continues well inboard of the Queen Charlotte fault (Figure 5.5), demonstrating that not all of the Pacific–North America plate motion is accommodated on the main plate boundary fault. Estimating slip rates along the Queen Charlotte fault is complicated by its offshore location. Based on the onshore GPS data and predicted motion of the Pacific Plate, the average geodetic slip rates for the northern Queen Charlotte fault (outboard of Sitka, Figure 5.5) are 48 ± 0.4 mm/year of right-lateral strike slip and 4 ± 0.3 mm/year of fault normal motion while the central Queen Charlotte fault (outboard of Prince of Wales Island) has 46 ± 0.4 mm/year right-lateral strike slip and 11 ± 0.3 mm/year of fault normal motion (Elliott

& Freymueller, 2020a). Utilizing high-resolution seafloor bathymetry data, Brothers et al. (2020) analyzed fault locations and offsets to estimate average right-lateral strike-slip rates of 54 ± 8 mm/year and <3 mm/year fault normal motion along the northern and central Queen Charlotte fault. While the geodetic and geomorphic strike-slip rates agree within uncertainties, the fault normal rates are significantly higher for the geodetic estimates. In an attempt to reconcile the geologic and geodetic data, Elliott and Freymueller (2020b) used the geomorphic fault normal rates as loose slip constraints in a revised geodetic block model for southeast Alaska. This revised model predicted average model slip rates along the northern and central Queen Charlotte fault of 49 ± 0.6 mm/year right-lateral strike slip and
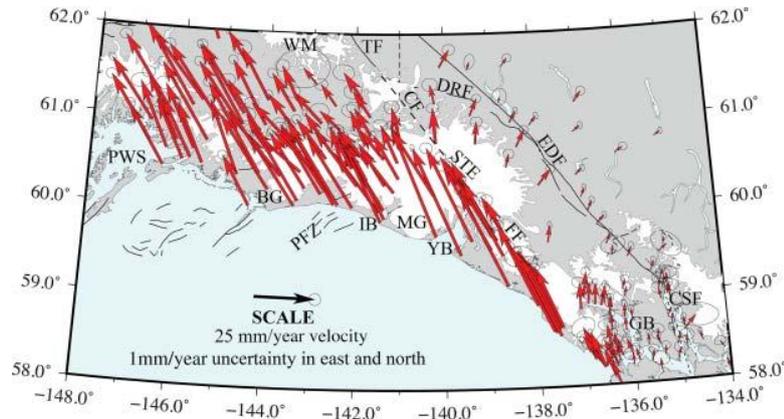
Figure 5.6 Interseismic velocities in the Chugach-St. Elias region and southeast Alaska from Elliott and Freymueller (2020a). Models and corrections used are the same as those detailed in Figure 5.5. PWS, Prince William Sound; WM, Wrangell Mountains; TF, Totschunda fault; DRF, Duke River fault; EDF, eastern Denali Fault; CSF, Chatham Strait fault; GB, Glacier Bay; FF, Fairweather fault; YB, Yakutat Bay; STE, St. Elias Mountains; MG, Malaspina Glacier; IB, Icy Bay; PFZ, Pamplona fault zone; BG, Bering Glacier; CF, proposed Totschunda–Fairweather connector fault.

3 ± 0.6 mm/year fault normal motion, values that are compatible with both the geodetic and geomorphic data. The revised block model also predicts a few mm/year of extension along the fault segment offshore of Mt. Edgecumbe volcano (west of Sitka), which has recently showed renewed activity (Grapenthin et al., 2022). The overall regional pattern of GPS velocities continues across the Chatham Strait fault without any discernable change (Figure 5.6). This, in combination with offshore seismic data across the fault that shows undisturbed sediment layers, suggests that the Chatham Strait fault is no longer an active structure accommodating significant relative plate motion (Brothers et al., 2018). North of Glacier Bay, the deformation is strongly influenced by the Yakutat block, an oceanic plateau that is currently translating along, colliding with, and subducting beneath southern Alaska (Christeson et al., 2010; Worthington et al., 2012). It is important to note that the geodetic definition of the Yakutat block is not exactly the same as the geologic definition of the Yakutat terrane (e.g., Plafker & Berg, 1994). The Yakutat block in the most recent geodetic models (Elliott & Freymueller, 2020; Elliott et al., 2013) consists of a wedge bounded by the Transition fault and the Pamplona fault zone to the west (Figure 5.1) attached to a shallowly subducting slab that extends beneath much of southcentral Alaska. The motion of all of the Yakutat block (wedge and slab) is defined by a single rotation pole.

The surface extent of the geologically defined Yakutat terrane extends farther west and north, but that region moves distinctly from the Yaktuat block and thus is not included in the geodetic definition. Based on the GPS data, the Yakutat block moves an average of 53 mm/year oriented at 23°W of N relative to North America (Elliott

& Freymueller, 2020a). The speed of the Yakutat block in this region is almost identical to the predicted speed of the Pacific Plate (Argus et al., 2010), but the orientation of the Yakutat motion is almost 10° more westerly than the orientation of the Pacific motion. The azimuth of the Yakutat block motion is about 10° more easterly than the average azimuth of the Fairweather fault, leading to convergence that is largely accommodated across two faults and two crustal slivers immediately outboard of the Fairweather fault (Elliott et al., 2010). Average right-lateral strike-slip rates on the Fairweather fault decrease from 45 mm/year in the south to 36 mm/year in the north (Elliott & Freymueller, 2020a). There are limited areas of predicted convergence along the southern portion of the fault, but as GPS velocities close to the fault are parallel to the fault, it is likely any convergence is accommodated through off-fault deformation. Inboard of the Fairweather fault, the GPS velocities show a clockwise rotation that results in transpression across the eastern Denali Fault (Figures 5.6 and 5.7).

Moving north into the St. Elias orogen, the tectonic regime is dominated by the collision of the Yakutat block with southern Alaska, and the effects of this collision and indentation are reflected in the GPS velocities (Figure 5.6). A fan-shaped pattern of GPS velocities surrounds the St. Elias syntaxis (Elliott & Freymueller, 2020a; Marechal et al., 2015). The relative motion is accommodated in several ways. Part of the motion is transferred inboard to the Totschunda and Duke River fault systems, with a portion likely localized on a Fairweather–Totschunda connector fault (Figure 5.6). A connector fault was first proposed based the alignment between the Fairweather and Totschunda faults (Richter & Matson, 1971; Lahr &
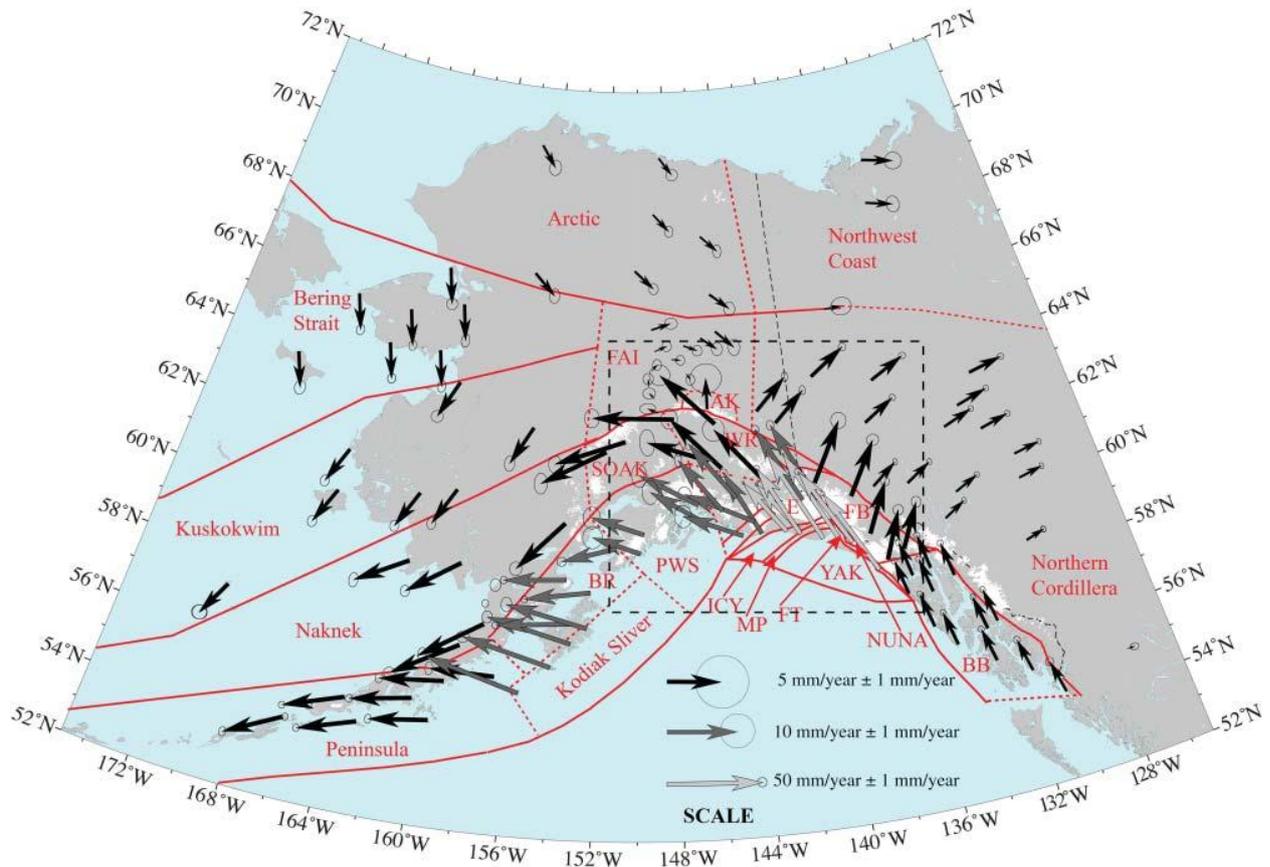
Figure 5.7 Blocks and model predictions of block motions for Alaska and western Canada. Note the three different scales for the velocities. BB, Baranof block; NUNA, Nunatak block; FT, Foothills block; YAK, Yakutat block; MP, Malaspina block; ICY, Icy Bay block; FB, Fairweather block; E, Elias block; WR, Wrangell block; AK, Alaska Range block; FAI, Fairbanks block; SOAK, Southern Alaska; BR, Bruin Bay block; PWS, Prince William Sound block. Dashed box shows area of Figure 5.8. Modified from Elliott and Freymueller (2020a).

Plafker, 1980). Using data from a network of GPS sites in the Yukon and a few sites in Alaska, Marechal et al. (2015) concluded that motion along a discrete structure such as a connector fault was not required by the deformation observations. A much larger data set spanning both sides of the proposed fault found evidence of right-lateral strike slip across a discrete structure along with possible diffuse deformation (Elliott & Freymueller, 2020a). Some motion in the collisional corner is accommodated through the clockwise block rotation inboard of the Fairweather fault discussed above (Figures 5.7 and 5.8). The majority of the motion is accommodated to the west of Yakutat Bay and the Malaspina Glacier. Here, the GPS velocities show a sharp gradient from the coast northward (Figure 5.6), indicating convergence of almost 40 mm/year over a relatively narrow region (Elliott et al., 2013). This high rate of convergence is accommodated along a series of north-to-northwest-dipping onshore–offshore crustal thrust faults, leading to the development of one

of the highest coastal mountain ranges on Earth (Elliott et al., 2013). The highest percentage of the relative motion is focused on the Yakataga-Chaix Hills fault, with smaller amounts distributed across the Malaspina fault through Ice Bay and the Foreland Fault zone, the latter of which is modeled as a creeping blind thrust and may be the newly developing deformation front for the Yakutat collision with southern Alaska (Figure 5.8; Worthington et al., 2012; Elliott et al., 2013). There is an abrupt change from the sharp gradient in GPS velocity magnitude in the thrust belt to larger, more broadly uniform velocities to the west of the Bering Glacier (Figures 5.5 and 5.6). This correlates to a transition from 20 to 30 km thick Yakutat oceanic crust east of the Pamplona zone to ~17 km thick Yakutat crust to the west (Worthington et al., 2012), which, while still very thick, is able to shallowly subduct. The transition between deformation regimes and crustal thicknesses aligns with the Gulf of Alaska shear zone (Figure 5.1), suggesting that the
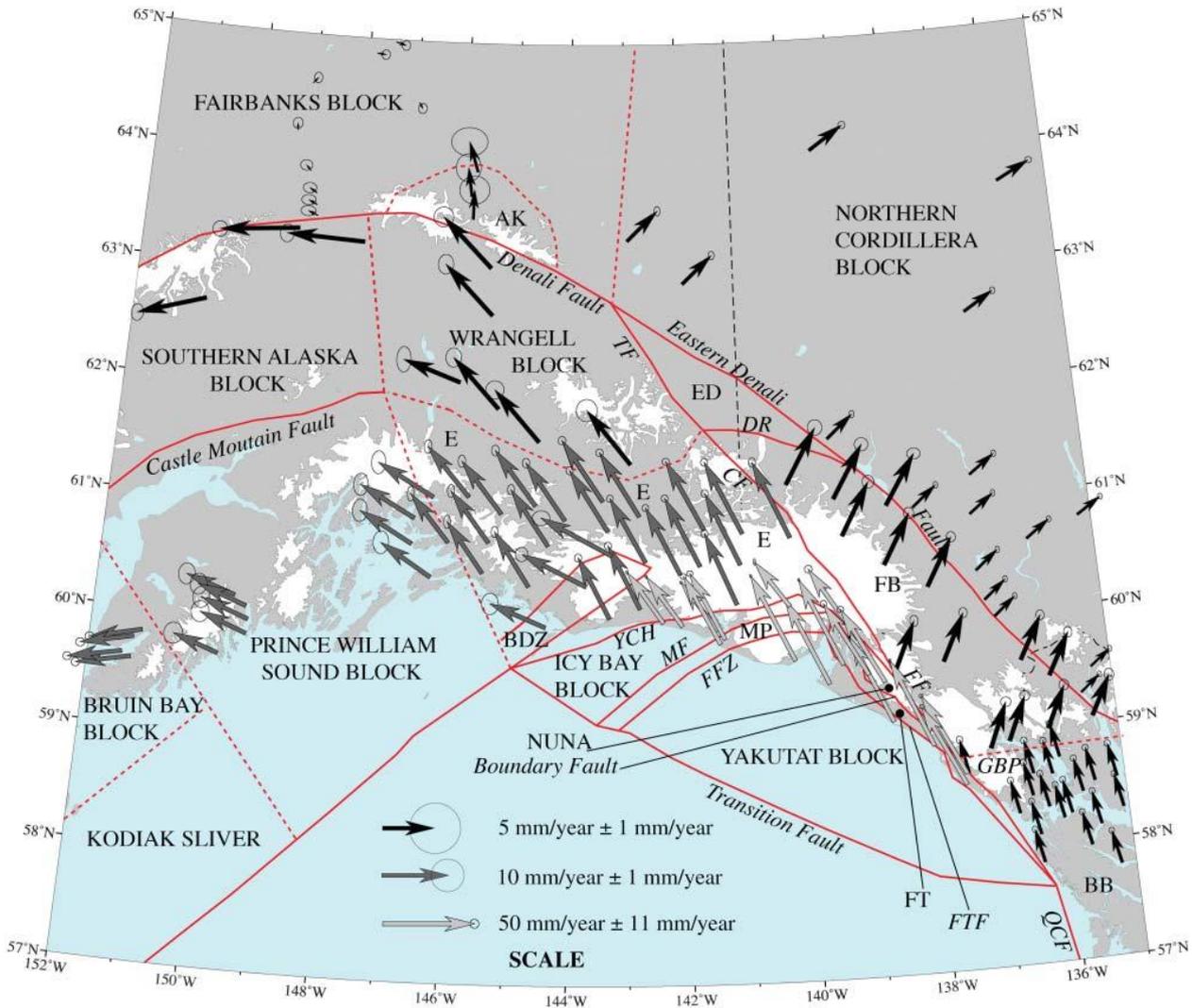
Figure 5.8 Blocks and model predictions of block motions for the southeast part of our study area. Note the three different scales for the velocities. Capital text denotes block names while italicized text denotes fault names. AK, Alaska Range block; TF, Totschunda fault; ED, Eastern Denali block; DR, Duke River fault; CF, Totschunda–Fairweather connector fault; FB, Fairweather block; GBP, Glacier Bay Partition; BB, Baranof block; FTF, Foothills thrust fault; FT, Foothills block; NUNA, Nunatak block; FFZ, Foreland fault zone; MP, Malaspina block; MF, Malaspina fault; YCH, Yakataga-Chaix Hills fault; E, Elias block; BDZ, Bering Deformation Zone.

differential stresses between collision and subduction of the Yakutat block may be transferred outboard to cause deformation in the Pacific Plate (Elliott et al., 2013).

The areas immediately surrounding the Yakutat block share two major characteristics: small or narrow blocks and relatively high data-model residuals. The inclusion of the Foothills, Nunatak, Icy Bay, and Malaspina blocks (Figure 5.8) provides statistically significant improvements to the data-model fit, but the blocks are less than 50 km in width, which is close to the crustal thickness in much of this region (Elliott et al., 2010; Elliott et al., 2013; Miller & Moresi, 2018) and much less than the lithospheric thickness. While known discrete structures,

including major plate boundary faults, bound these narrow blocks, these areas may be more aptly called zones of distributed deformation. Residuals in northernmost southeast Alaska and the St. Elias are higher than in other parts of Alaska, such as western Alaska, which is discussed below. The higher residuals suggest that the deformation observed through the GPS data cannot be fully explained through the rigid block rotations and elastic strain on faults defined by the block model. Altogether, the areas of Alaska and western Canada surrounding the Yakutat block likely require some degree of distributed or continuum deformation in response to the rapid collision of the Yakutat oceanic plateau.

Southcentral Alaska and the Alaska Peninsula

Tectonic deformation in southcentral Alaska is dominated by subduction of the shallowly dipping Yakutat slab and the Pacific Plate (Figures 5.5 and 5.6). We discuss the subduction interface in a later section; in this section, we focus on motion of upper-plate blocks and faults in the region south of the Denali Fault as well as along the Alaska Peninsula. In areas over or near the subduction interface, upper-plate motion is usually estimated as part of a block model as the steady-state interseismic GPS velocities result from a combination of block motion and strain accumulation from the interface. A number of published models covered parts of the region and used different upper-plate and fault configurations. Elliott et al. (2013) defined the area north and west of the St. Elias thrust faults (except for a small zone around the Bering Glacier) as the Elias block (Figure 5.8). The eastern boundary of the block was the Fairweather–Totschunda Connector fault while the northern and western boundaries were not explicitly defined. The counterclockwise-rotating Elias block predicted north-northwesterly motion of 10–15 mm/year in the eastern part of the block and westerly velocities of less than 10 mm/year near the eastern edge of Prince William Sound. Focusing on the Prince William Sound to Kodiak region (Figure 5.1), Li et al. (2016) defined the region east of Prince William Sound and north of the Castle Mountain fault to be the counterclockwise-rotating Southern Alaska block of Fletcher (2002), the rotation of which was based on geodetically derived slip rates along the Denali Fault. The area north of the Castle Mountain and Bruin Bay faults was defined to be the southwesterly moving Bering plate of Cross and Freymueller (2008). The region bounded to the east by Prince William Sound and to the north by the Castle Mountain–Bruin Bay system was defined to be the Peninsula block, which moved to the southwest and became more arc parallel along the Alaska Peninsula. Li and Freymueller (2018) used the same configuration of blocks but re-estimated the motion of the Peninsula block using a different set of GPS sites. This resulted in predicted block motion that was slightly faster and more northwesterly than that predicted by the 2016 model. Examining deformation along the Alaska Peninsula, Drooff and Freymueller (2021) adopted the block configuration of Li et al. (2016) as well as that study's estimate of the Peninsula block motion.

The expanded, Alaska-wide GPS data set used in Elliott and Freymueller (2020a) required a re-evaluation and reconfiguration of upper-plate blocks. Overall, the area south of the Denali Fault moves roughly parallel to the Fairweather–Queen Charlotte–Totschunda fault system in the east and gradually undergoes a counterclockwise rotation until the upper plate is moving nearly arc parallel along the Alaska Peninsula (Figures 5.7 and 5.8). The Elias block ends to the east of Prince William Sound and has predominately northwestward motion. The Prince William Sound block shows slower and slightly more westerly velocities. To the west of the Kenai Peninsula, the Bruin Bay block has similar magnitude motion but at a more westerly orientation. West of Kodiak Island, the Peninsula block has significantly smaller velocities oriented parallel to the trench. This updated Peninsula block is similar to but slightly slower than the previous versions discussed above. Outboard of the Bruin Bay block, a block moving more rapidly to the northwest was required to explain the GPS observations on the seaward side of Kodiak Island. The model boundary between the Kodiak Sliver and the Bruin Bay block is consistent with geomorphic and paleoseismological evidence for Holocene deformation (Carver et al., 2008; Ramos et al., 2022). The upper boundary for this series of coastal blocks is a fault system comprised of the Bruin Bay and Castle Mountain faults along with a boundary that runs through the Chitina River Valley to connect to the Duke River–Totschunda system (Figure 5.8). Between this boundary and the Denali system, two blocks divide the region. In the east, the Wrangell block moves northwesterly, with speeds half as large as those displayed by the Elias block. In the western half of the region, the Southern Alaska block undergoes a westward rotation that results in velocities roughly parallel to the Denali Fault. Similar, smaller motion continues into western Alaska, which is discussed further below.

There is a distinct change in the pattern of the predicted block velocities across the region south of the Denali Fault. In the east, the Wrangell and Elias blocks display northwesterly motion. Farther west, blocks undergo increasing amounts of westward rotation. The division between these regimes roughly aligns with the eastern edge of the Alaska subduction interface and, in particular, the eastern edge of the Yakutat flat slab. This suggests that the Yakutat collision, for which the convergence direction is northwest, drives deformation in the east while the flat slab drives counterclockwise rotation of the region to the west (Elliott & Freymueller, 2020a).

Interior Alaska

Geodetic studies of long-term motion in interior Alaska are complicated by the impact of the ongoing postseismic deformation due to the M7.9 2002 Denali Fault earthquake. For that reason, data used in recent studies has been limited to pre-November 2002 data. Pre-2002 GPS velocities throughout most of interior Alaska are smaller than velocities to the north in the Arctic and to the south of the Denali Fault (Figures 5.5 and 5.9), suggesting that interior Alaska may be an inflection point between deformation driving forces in Alaska (Elliott & Freymueller, 2020a). One area of interior Alaska that shows larger velocities is the eastern Alaska Range directly north of the Denali Fault, where northward GPS
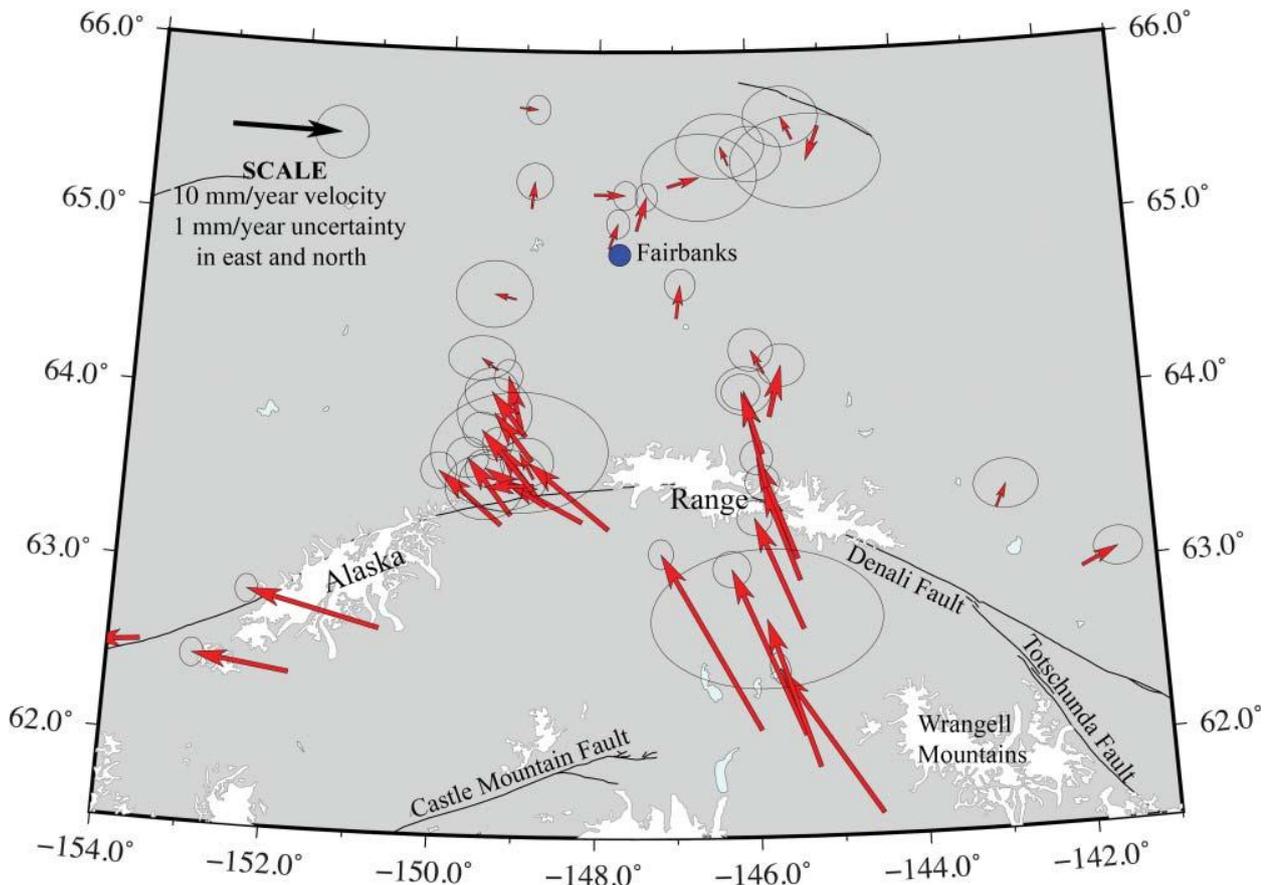
Figure 5.9 Interseismic velocities in interior Alaska from Elliott and Freymueller (2020a). Models and corrections used are the same as those detailed in Figure 5.5.

velocities occur in the same region as high topography, active thrust faults, and high rates of exhumation (e.g., Bemis et al., 2015; Benowitz et al., 2011; Figures 5.8 and 5.9). A major tectonic feature of interior Alaska is the Denali Fault, a right-lateral strike-slip fault. The block model of Elliott and Freymueller (2020a) predicts a slip rate of 6–7 mm/year strike slip and ~1 mm/year of contraction along the west central and central segments of the Denali Fault and smaller amounts of right-lateral transpression on the western and eastern Denali faults. The updated geodetic estimates along the central Denali Fault are quite similar to those of Fletcher (2002), which should not be surprising as both studies used geodetic data collected before the 2002 earthquake. While the general pattern of faster rates along the central fault and lower rates to the west and east agrees with geologic studies (e.g., Haeussler et al., 2017), the geodetic rates along the central Denali are half the geologic rates. There is a question of whether the pre-2002 GPS data represent true interseismic deformation since they were collected in the decade prior to the M7.9 earthquake.

To match the geologic rates, the motion of the region south of the Denali Fault would have to increase significantly and that would be inconsistent with GPS data through southcentral Alaska and the St. Elias orogen (Figure 5.6). Resolving the discrepancy between geodetic and geologic slip rates along the central Denali Fault will ultimately require longer-term interseismic data collected after the Denali postseismic signal has fully decayed. Another notable feature in interior Alaska is the series of northeast-trending, left-lateral seismic zones that have nucleated several M7+ events (Ruppert et al., 2008; Figure 5.1). The sparse pre-2002 GPS data in interior Alaska do not allow slip rates to be resolved across the individual seismic zones, but the bulk deformation across the region is consistent with left-lateral motion on the shear zones (Elliott & Freymueller, 2020a).

Western Alaska and the Eastern Bering Sea Region

Previous geodetic work in western Alaska and the Bering Sea region was based on a sparse network of mainly campaign sites and suggested that a single,

clockwise-rotating Bering block or plate occupied the region (Cross & Freymueller, 2008). The expansion of the PBO/NOTA network into western Alaska added significantly more spatial coverage (Figure 5.2). Using the updated data set and a block modeling technique, Elliott and Freymueller (2020a) found a more complex scenario, with four blocks spanning the region of the Bering plate of Cross and Freymueller (2008) (Figure 5.7). Block motions transition from southerly directed in the north around the Bering Strait area to southwest directed in southwest Alaska to nearly margin parallel along the Aleutian arc. The eastern boundaries of the blocks run along the western edge of the interior seismic zones and the Revelation Mountains (Figures 5.1 and 5.7). Boundaries between the blocks are the Kobuk, Kaltag, western Denali, and Castle Mountain/Bruin Bay fault systems and implied offshore extensions.

As discussed in Elliott and Freymueller (2020a), deformation in western Alaska and the eastern Bering Sea region is explained well by the rotation of several rigid blocks divided by major faults as the residuals between the GPS data velocities and the model predictions are very small. With the exception of three sites that are complicated by signals from the subduction zone, all the residuals fall well within the two-sigma uncertainty limits of the data, and 78% of the residuals are smaller than their respective one-sigma data uncertainty limits. The excellent fit to the data provided by the small number of rigid block rotations supports the idea that additional faults or blocks are not required to explain the data, but this does not preclude the existence of a fault or faults with very low slip rates within a block. To be able to capture the effects of elastic strain along a fault with geodetic data, an adequate density of sites to characterize the deformation across the fault and elastic strain signals higher than data uncertainties are needed. In western Alaska, the GPS network is sparse, making it more difficult to delineate elastic strain along faults unless the slip magnitude is high or there is a notable difference in motion direction between blocks. Based on the formulation of Savage & Burford, (1973), the surface deformation due to a strike-slip fault locked to a depth of 10 km with a slip rate of 1 mm/year would approach a maximum of 0.5 mm/year on each side of the fault far from the fault, with areas closer to the fault slowing lower values with minimum values near 0 next to the fault. The average one-sigma uncertainty in the GPS data in western Alaska is 0.5 mm/year, making it unlikely that elastic deformation from faults with slip rates of ≤1 mm/year would be captured.

Arctic Alaska

GPS data in Arctic Alaska reveal a gentle counterclockwise rotation above the Kobuk fault (Figure 5.5). This is a sharp contrast to the clockwise rotations observed in western Alaska and the Bering Sea region. The hinge line between the two regimes appears to be along or near the Kobuk fault, and the mix of right-lateral strike slip and extension predicted to occur across that boundary is consistent with the series of earthquakes that occurred during 2014 in the area of Noatak, Alaska (Elliott & Freymueller, 2020a). Like the regions of western Alaska discussed above, data-model residuals for the 2020 block model are very small throughout Arctic Alaska, suggesting that the data are fit well by rigid block motion and that further subdivisions of the region are not required by the current data set.

Northern Cordillera of Canada

Based on the GPS data, the region of Canada immediately adjacent to Alaska is divided into two blocks: one in the north, next to the Beaufort Sea, and the other encompassing the Yukon and parts of British Columbia (Figure 5.7). Due to the current extent of the available data, exact boundaries of these blocks are uncertain, but the eastern limit of deformation is likely east of the Mackenzie and Canadian Rocky Mountains (Drooff & Freymueller, 2021; Leonard et al., 2008). In the south, the deformation pattern shows overall northeastward motion, with velocities generally larger as you move north (Figures 5.5 and 5.7). No discernable strain is present across the Tintina fault, and the small data-model residuals suggest that the region is fit adequately by a combination of rigid block motion and elastic strain accumulation along the eastern Denali Fault (Elliott & Freymueller, 2020a; Elliott et al., 2010). The direction and magnitude of the motion in the Northern Cordillera aligns with the counterclockwise rotation north of Glacier Bay and the fan-shaped deformation field around the Yakutat collisional front, suggesting that the motion may be due to strain transfer from the Yakutat collision (Elliott & Freymueller, 2020a; Leonard et al., 2007; Marechal et al., 2015). Although the block modeling concept seems to describe the deformation well, the GPS data do not rule out the possibility that strain is transferred via an orogenic float mechanism where a brittle upper crust moves over viscous lower crust and lithospheric mantle, an idea that is supported by the regional hot geotherm (Mazzotti & Hyndman, 2002; Mazzotti et al., 2008). North of about 65° north, GPS velocities are smaller and are not fit by the block rotation derived from the velocities to the south and so are defined to be on a separate block. Based on the current data set, it cannot be determined if the velocities are a continuation of the deformation across Arctic Alaska or if the velocities are a completely separate regime, perhaps related to the observed seismicity in the Richardson Mountains (Leonard et al., 2008; Mazzotti et al., 2008).

Coupling and Slip Along the Subduction Interface

Interseismic slip along a subduction interface estimated through geodetic data is usually defined by the slip deficit (or slip deficit rate) or coupling. The slip deficit rate is the amount of fault motion that is not happening because the fault sides are stuck or locked together and is the amount of motion that is accumulating toward slip during the next earthquake. Coupling is equal to the slip deficit rate divided by the full rate of plate convergence. Coupling can vary from 0 (fully uncoupled or unlocked, also known as creeping) to 1 or 100% (fully coupled or locked). The estimated slip deficit (and thus coupling) is influenced by a number of factors, including the lower plate motion, upper-plate motion, the distribution of data used, the model geometry of the subducting slab used in the interseismic model, and modeling parameters such as smoothing.

Geodetic coupling estimates along the Alaska–Aleutian subduction interface are highly heterogenous both downdip and along strike as shown in Figure 5.10, which is a composite map based on a number of studies of interseismic coupling. In the paragraphs below, we discuss the studies that have contributed to our understanding of coupling in each region of the interface, the assumptions and reasons for variations between models,

and implications for seismic hazard evaluation using geodetic coupling estimates.

Suito and Freymueller (2009) estimated an interseismic slip model that focused on the region of the interface that ruptured during the M9.2 1964 Prince William Sound earthquake. This model assumed that the Pacific Plate was the subducting plate throughout the region while the upper plate was assumed to be the counterclockwise-rotating Southern Alaska block of Fletcher (2002). Their model predicts a high degree of coupling throughout the Prince William Sound region (the site of one of the major asperities that ruptured during the 1964 earthquake [Suito & Freymueller, 2009; Suleimani & Freymueller, 2020]), with fully coupled patches to the east of Prince William Sound and beneath western Prince William Sound and the eastern Kenai Peninsula (Figure 5.1). A highly coupled interface is also predicted beneath and outboard of Kodiak Island and throughout the Semidi region. The region between western Prince William Sound and Kodiak displays much lower coupling, with an area of almost no coupling along the northern half of the Kenai Peninsula. Li et al. (2016) also focused on the 1964 rupture region but used a block modeling technique with a different configuration of blocks along with an interface geometry defined by the
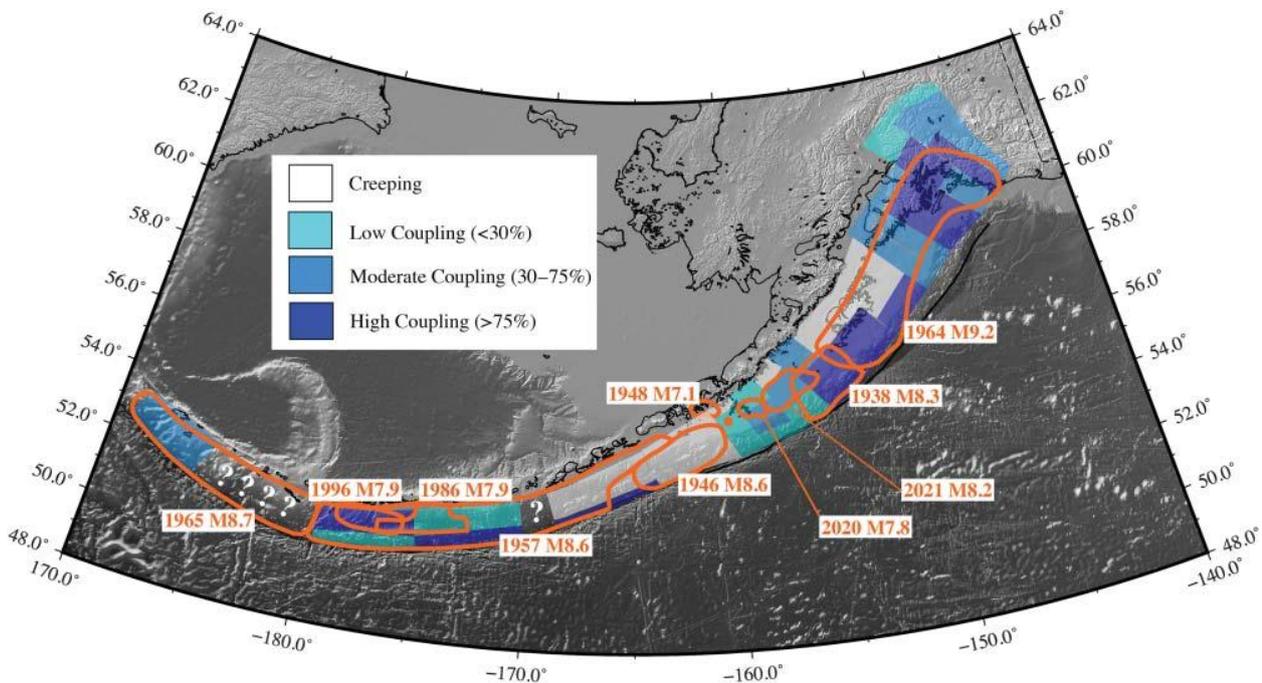

Figure 5.10 Coupling and rupture or aftershock areas of major earthquakes along the Alaska–Aleutian subduction zone. Coupling estimates are a composite from Cross and Freymueller (2008), Xue and Freymueller (2020), Elliott and Freymueller (2020a), Drooff and Freymueller (2021), and Xiao et al. (2021). Orange outlines are aftershock or ruptures areas (Sykes et al., 1980; López & Okal, 2006; Freymueller et al., 2021; Xiao et al., 2021; Elliott et al., 2022).

Slab 1.0 model (Hayes et al., 2012) which was significantly steeper and deeper than the interface geometry used by Suito and Freymueller (2009). The geometry used by Li et al. (2016) also did not extend as far west or east as the earlier model. The subducting plate was assumed to be Pacific Plate throughout while the upper plate was comprised of the Peninsula block (estimated as part of the model inversion) through Prince William Sound and the Alaska Peninsula with the southern Alaska block of Fletcher (2002) to the east and north of the Peninsula block and the Bering block of Cross and Freymueller (2008) to the northwest. Predicted motion of the Peninsula block was to the west–southeast, with nearly arc-parallel motion along the Alaska Peninsula. Despite differences in assumptions and geometries, the best-fit steady-state coupling distribution of Li et al. (2016) shared broad similarities with that of Suito and Freymueller (2009): strong coupling in the Prince William Sound region and offshore and under part of Kodiak Island with significantly lower coupling beneath and outboard of the western Kenai Peninsula.

Moving westward, Li et al. (2018) investigated the interseismic deformation between western Kodiak Island and the Sanak region. The model used the block modeling technique and most modeling parameters of Li et al. (2016), but re-estimated the motion of the Peninsula block using GPS velocities from the western portion of the Alaska Peninsula and excluding some data from the Cook Inlet area that may have biased the motion estimate of that block due to SSEs. The new estimate of the Peninsula block was still roughly arc parallel but of smaller magnitude than that of Li et al. (2016). The estimated coupling distribution displayed an overall westward decrease in the degree of coupling: strong coupling beneath and outboard of Kodiak and Chirkof Islands, moderate coupling in the Semidi region, lower coupling in the region of the Shumagin Islands, and a fully creeping interface in the Sanak region. Sharp transitions in coupling, particularly between the Kodiak and Semidi segments of the interface, provided the best fit to the data. Drooff and Freymueller (2021) used an expanded GPS data set in the Shumagin Islands to re-evaluate the coupling distribution along the Alaska Peninsula region. The upper-plate blocks were set to the block motion used in Li et al. (2018), and the same modeling technique was used. The estimated coupling distribution was very similar to the earlier model in the Kodiak and Semidi segments. Coupling boundaries between the Semidi, Shumagin, and Sanak segments were slightly shifted, and the expanded GPS data set required an additional coupling boundary that divided the Shumagin segment into two segments. The western Shumgain segment showed lower coupling than the eastern segment. Xiao et al. (2021) presented an alternate version of the coupling model of Drooff and

Freymueller (2021). The latter model, along with the models of Li and Freymueller (2018) and Li et al. (2016), used an imposed model smoothing constraint that required the highest coupling to occur at the trench and decreasing degrees of coupling in the downdip direction on the subduction interface. In contrast, the alternative model in Xiao et al. (2021) used a Gaussian smoothing constraint, which put the highest coupling toward the middle of each segment. This difference between the coupling models was particularly consequential in the Semidi segment, where the Gaussian model located the highest coupling in the vicinity of the rupture area of the 2021 M8.2 Chignik earthquake. The Gaussian model provided a similar goodness of fit to the data as the original model.

Elliott et al. (2013) focused on the eastern portion of the Alaska subduction zone and used a different modeling technique than the studies discussed above along with a greatly expanded campaign GPS data set across the Chugach and St. Elias ranges. The downgoing plate in this case was the Yakutat flat slab, with a motion defined by the block model estimate of Elliott et al. (2010). The slab geometry had a very shallow dip of 5° and extended east to the Bering Glacier and through Prince William Sound (Figure 5.1), where the model space ended. The upper plate was the counterclockwise-rotating Elias block, motion for which was estimated as part of the model inversion. Estimated coupling was high beneath and to the northwest of the Bering Glacier region as well as under northeastern Prince William Sound. More moderate coupling was predicted for the region offshore the Bering Glacier and between the Bering Glacier and Prince William Sound Building on this model. Elliott and Freymueller (2020a) presented an Alaska-wide block model that included a subduction interface from the Bering Glacier through the Alaska Peninsula. The upper plate in this model was comprised of a number of different blocks as discussed above, all of which were estimated as part of the model inversion. The model slab geometry was more complex than in any of the previous block models. In the east, the shallowly dipping Yakutat flat slab extended from the Bering Glacier to the Denali Fault in the north to the Kenai Peninsula in the west. The motion of the Yakutat block and slab were estimated as part of the model inversion. The geometry of the flat slab was determined by a combination of seismic data (e.g., Worthington et al., 2012; Eberhart-Phillips et al., 2006) and best fit to the geodetic data. The slab geometry transitioned from Yakutat flat slab to Pacific Plate under the Kenai Peninsula (Kim et al., 2014). Estimated coupling varied widely across the subduction interface (Figure 5.10). The eastern edge of the flat slab showed moderate coupling while the northern edge has low coupling. Areas of the interface outboard of the Bering Glacier and extending through eastern and northern Prince William Sound are

strongly coupled as is the area underlying the southeast Kenai Peninsula to the trench. Areas to the east of Prince William Sound and the rest of the Kenai Peninsula have moderate coupling. The region from the southern half of Kodiak Island to Chirikof Island to the trench is fully coupled while the interface beneath the Semidi Islands is moderately coupled. The Shumagin Islands region has low coupling. Based on the onshore GPS velocities, the Sanak region is fully creeping.

As mentioned during the discussion of the coupling distribution in the Shumagin region, there can be nonuniqueness issues with models using the same geodetic data sets. This is particularly true in regions with uneven or sparse data, such as the Alaska subduction zone where most of the data are onshore while most of the interface is offshore far from the GPS sites. Investigating what coupling distributions are allowed (or not allowed) given a data set is useful for evaluating hazards. Here, we present a series of new alternate coupling distributions using the model geometry of Elliott and Freymueller (2020a) and the data set from that paper augmented by that of Drooff and Freymueller (2021) in the Shumagin region (Figure 5.11). All of the alternate coupling distributions fit the data at an acceptable level given the data uncertainties. In Figure 5.11a, we modify the coupling distribution of Elliott and Freymueller (2020a) to match the coupling distribution of Xiao et al. (2021) to better fit the Shumagin data and place an area of high coupling within the rupture of the 2021 M8.2 Chignik earthquake. We add a band of lower coupling near the trench in the Kodiak segment while a region of moderate coupling has been added near the trench in the Sanak region (Figure 5.11b). This latter region has been estimated to be fully creeping (zero coupling) in all of the models discussed in the paragraphs above due to the fact that the data on the Alaska Peninsula do not require (and is poorly fit by) any significant coupling. As there are no data constraints offshore, the creep has been assumed to continue to the trench. This has created a conundrum, as the Sanak segment of the subduction interface ruptured during the 1946 M8.6 earthquake that also generated an abnormally large tsunami (López & Okal, 2006). The alternate model shows that a narrow band of low-to-moderate coupling can occupy the region near the trench without misfitting the data on the Alaska Peninsula. This band could provide a mechanism for
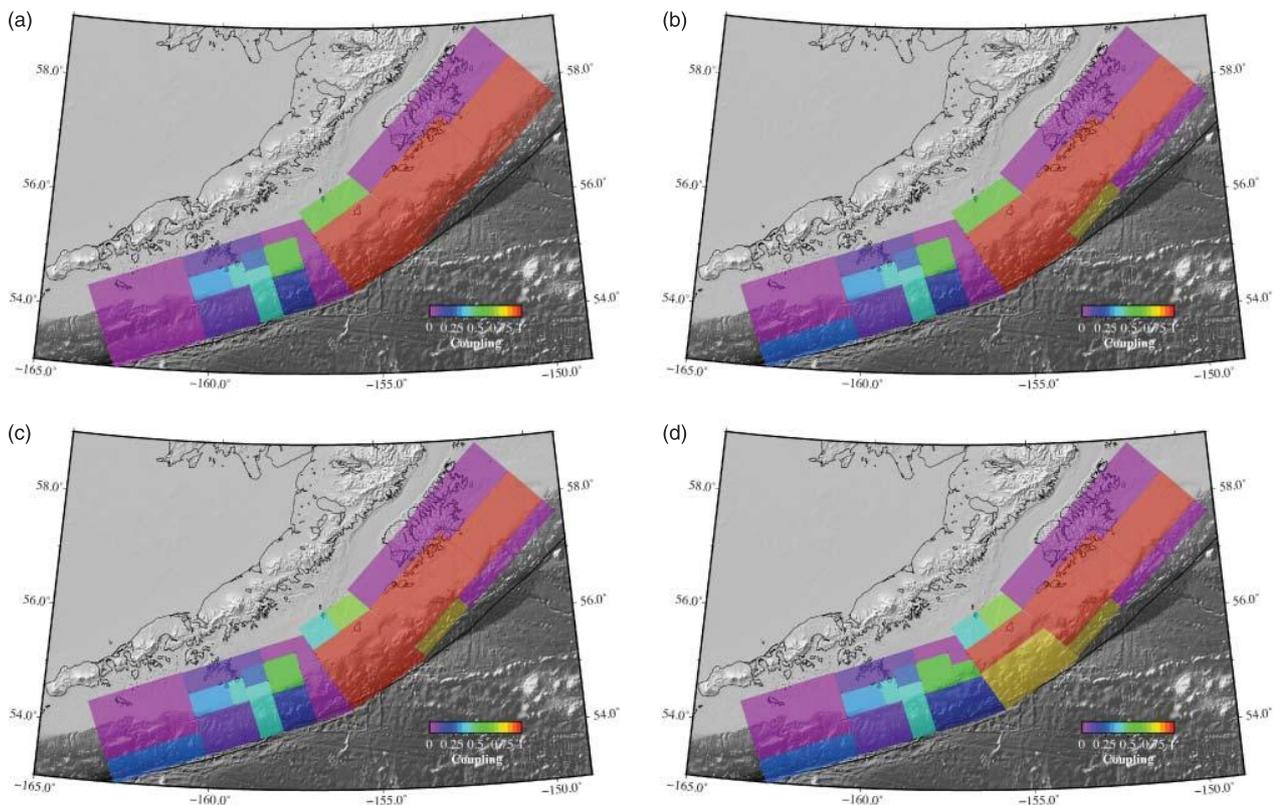

Figure 5.11 (a) Coupling distribution model of Elliott and Freymueller (2020a) modified to match Xiao et al. (2021) in the vicinity of the Shumagins. (b) Model A, modified to have different near-trench values in the Sanak and Kodiak segments. (c) Model B, with varied coupling in the vicinity of the Semidi Islands. (d) Model C, with lower coupling outboard of Chirikof Island.

the generation of tsunamigenic subduction earthquakes along this segment of the interface which could then rupture into surrounding regions. The lack of offshore constraints is also why the near-trench region outboard of Kodiak Island is usually assumed to be fully coupled. Narrow bands of lower coupling near the trench are compatible with the available GPS data set on Kodiak Island. We introduce variable coupling under the Semidi Islands (Figure 5.11c), with low-to-moderate coupling to the west and higher coupling to the east. Finally, we reduce the fully coupled west of Kodiak to a narrower band directly beneath Chirikof Island with lower (but still relatively high) coupling stretching outboard toward the trench (Figure 5.11d). The developing network of seafloor/acoustic GPS stations will provide crucial future constraints for the near-trench region of the subduction zone and will help resolve some of the current ambiguity.

Another important question for subduction zone hazard evaluation is how (or if) the present coupling distribution is related to past earthquakes. The composite coupling distribution for the Alaska subduction zone with rupture areas of historic earthquakes is shown in Figure 5.10. Almost all of the great (M ≥ 8) earthquakes ruptured areas of the interface that exhibit moderate or strong coupling within at least part of the rupture. The two major areas of high slip (asperities) during the 1964 M9.2 earthquake (Suito & Freymueller, 2009; Suleimani & Freymueller, 2020) are strongly coupled now. Most of the area that ruptured during the M8.3 1938 earthquake (e.g., Freymueller et al., 2021) is also strongly coupled in the present day. The exception to this trend is the 1946 M8.6 tsunamigenic earthquake, which ruptured an area generally regarded as fully creeping. But as discussed above, a narrow band of higher coupling is allowed within the rupture area given the current data set, providing a possible explanation. Lateral boundaries in geodetic coupling may be correlated to structural differences and influence earthquake nucleation and propagation (e.g., Elliott et al., 2022; Shillington et al., 2015). The geodetic data require a coupling boundary between the Shumagin (lower coupling) and the Semidi (higher coupling) segments (Figure 5.10). Offshore seismic imaging suggests that the Shumagin segment has a rougher interface while the Semidi segment has an interface smoothed by thick sediment, which may explain the difference in the coupling estimates (Bécel et al., 2017; Li et al., 2018; Shillington et al., 2015). The 2020 M7.8 Simeonof earthquake nucleated near the boundary between this segment and ruptured to the west (Crowell & Melgar, 2020; Xiao et al., 2021) while the 2021 M8.2 Chignik earthquake began near the boundary and ruptured to the east (Elliott et al., 2022; Liu et al., 2022). Several other earthquakes appear to have followed a similar pattern of nucleating near the boundary and rupturing away from the boundary, including the 1938 M8.3 earthquake, suggesting a persistent coupling boundary (Briggs et al., 2014; Freymueller et al. 2021; Nishenko & Jacob, 1990; Witter et al., 2014).

5.5.2. Coseismic Deformation

A large number of earthquakes and SSEs have occurred within Alaska and the surrounding area in recent decades (Figure 5.12; Table 5.1). In this section, we present
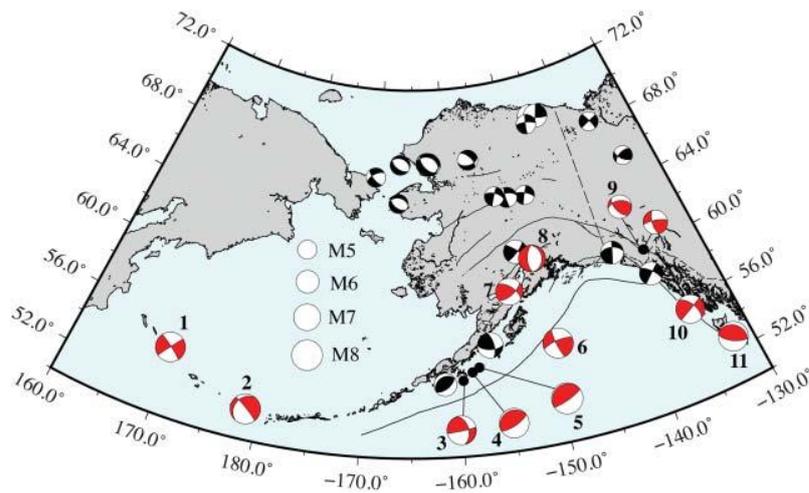

Figure 5.12 Focal mechanisms of M>5 earthquakes in Alaska over the past 15 years. Red focal mechanisms show earthquakes that will be discussed in the paper: 1. 2017 M7.8 Komandorsky, 2. 2014 M7.9 Little Sitkin, 3. 2020 M7.6 Sand Point, 4. 2020 M7.8 Simeonof, 5. 2021 M8.2 Chignik, 6. 2018 M7.9 Offshore Kodiak, 7. 2016 M7.1 Iniskin, 8. 2018 M7.1 Anchorage, 9. 2017 Haines Doublet (M6.2 and M6.3), 10. 2013 M7.5 Craig, and 11. 2012 M7.8 Haida Gwaii. Focal mechanisms are taken from the Global CMT catalog (Dziewonski et al., 1981; Ekström et al., 2012).

Table 5.1 Summary of major earthquakes since 2004 that have useful displacement data from GPS.

Event	Date	M_w	Lat	Long	Depth	Global CMT ID
Haida Gwaii	27 October 2012	7.8	52.79	−132.10	14	201210280304A
Craig	5 January 2013	7.5	55.23	−134.86	8.7	201301050858A
Little Sitkin	23 June 2014	7.9	51.85	178.74	109	201406232053A
Iniskin	24 January 2016	7.1	59.62	−153.34	125.6	201601241030A
Haines doublet 1	1 May 2017	6.2	59.82	−136.71	10	201705011231A
Haines doublet 2	1 May 2017	6.3	59.83	−136.7	2.5	201705011418A
Komandorsky	17 July 2017	7.8	54.44	168.86	10	201707172334A
Offshore Kodiak	23 January 2018	7.9	56.00	−149.17	14.1	201801230931A
Anchorage	30 November 2018	7.1	61.35	−149.96	46.7	201811301729A
Simeonof	22 July 2020	7.8	55.07	−158.60	28	202007220612A
Sand Point	19 October 2020	7.6	54.60	−159.63	28.4	202010192054A
Chignik	29 July 2021	8.2	55.36	−157.89	35	202107290615A

Notes: Locations and depths are taken from the USGS earthquake catalog. Earthquake IDs are from the Global CMT catalog (Dziewonski et al., 1981; Ekström et al., 2012).

updated coseismic displacement estimates and summarize the key findings about most of the significant earthquakes that have occurred since the first deployments of the EarthScope program in 2004. Earlier events were discussed in Freymueller et al. (2008). Except where figures were taken from past publications, the displacements shown here have been recomputed using the approach described in Section 3 from our current solution series (version 4), for continuous sites only. Displacements are available in the data repository linked in the Data Availability section. Some events in remote parts of Alaska are not included here because they were too poorly recorded by the cGPS network. One such event, an M6.4 earthquake in the northern Brooks Range foothills southwest of Kaktovik on 12 August 2018, was the subject of more intensive studies based on InSAR data (Gaudreau et al., 2019; Rollins et al., this volume). Several events in the western Aleutians were recorded only by the GPS site AC66 and are not discussed here. Figures 5.13–5.25 show displacements from cGPS only in most cases, but a few cases are augmented with displacements from campaign sites. In addition to the recent earthquakes, important new insights have been gained into several older earthquakes over the past 15 years, mostly through re-analysis of older data or newly acquired geological data. This work provides important new context for interpreting the newer geophysical data and has revised our picture of the 1938, 1957, and 1964 earthquakes (Figure 5.10).

Haida Gwaii Earthquake (M7.8, 27 October 2012)

Pacific–North America relative motion is obliquely transpressive in the Haida Gwaii region, in part due to the geometry of the margin. Slip partitioning results in largely thrust motion on a low-angle thrust fault beneath the Queen Charlotte terrace seaward of the strike-slip Queen Charlotte transform fault (Cassidy et al., 2014). The 2012 Haida Gwaii earthquake involved slightly oblique thrusting (~20° from pure thrust slip) on the low-angle thrust fault (e.g., Lay et al., 2013; Nykolaishen et al., 2015). It generated a large tsunami with up to ~7 m runup on the Pacific coast of Moresby Island in the Haida Gwaii archipelago (Leonard & Bednarski, 2014). Most of the near-field coseismic displacements came from repeated surveys of campaign GPS sites (Nykolaishen et al., 2015) as there was only one near-field cGPS site, BCSS (Figure 5.13).

Postseismic displacements suggest a component of afterslip or triggered slip on the Queen Charlotte fault, based on observed accelerated right-lateral shear (Nykolaishen et al., 2015). Hayward and Bostock (2017) used repeating earthquakes to infer accelerated postseismic slip on the Queen Charlotte fault. Tian et al. (2021) developed a viscoelastic relaxation and afterslip model for this event and the nearby 2013 M7.5 Craig earthquake (next section). Although constrained mainly by relatively far-field data, they were able to distinguish between the rapid decay of afterslip and the longer-term relaxation of the asthenosphere and estimate the asthenospheric viscosity to be a Burger's body with a Maxwell element viscosity of $(0.8–3) \times 10^{19}$ Pa·s and a Kelvin element viscosity 1 order of magnitude lower.

Craig Earthquake (M7.5, 5 January 2013)

The Craig earthquake struck off the coast of southeast Alaska (Figure 5.14), rupturing an ~150 km long segment of the Queen Charlotte fault, and an ~100 km portion of
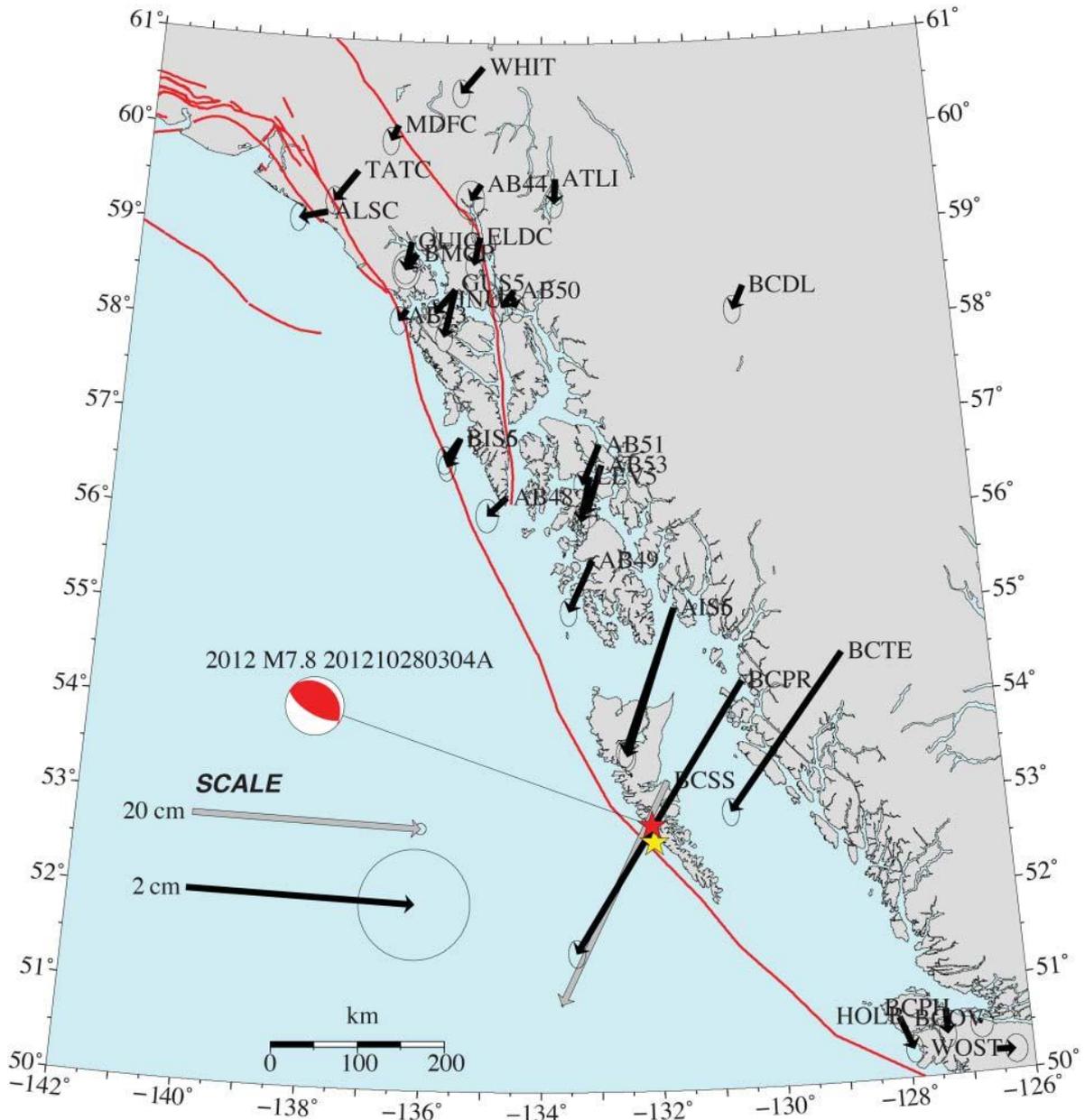
Figure 5.13 Displacements from the 2012 M7.8 Haida Gwaii earthquake, shown by vectors tipped with 95% confidence ellipses. The red star shows the USGS location, the yellow star shows the Global GMT location, and the red beachball shows the focal mechanism from the Global CMT catalog (Dziewonski et al., 1981; Ekström et al., 2012). Displacements were computed in ITRF 2014. Sites with gray vectors are shown at a different scale, in order to fit on the map. Vertical displacements from this event were small and are not shown. Major active faults are shown by red thick lines, from the Alaska Quaternary Faults and Folds database (Koehler et al., 2012).

the fault featured super-shear rupture (Yue et al., 2013). It likely ruptured the gap between the earlier 1949 and 1976 events on the Queen Charlotte fault (Ding et al., 2015). Displacements from this event were predominantly horizontal at all sites, reflecting the strike-slip motion of the

rupture and the distance from the fault of all of the GPS sites.

Ding et al. (2015) modeled the coseismic displacements based on a combination of static GPS displacements and high-rate (1 Hz) kinematic displacement records. Because
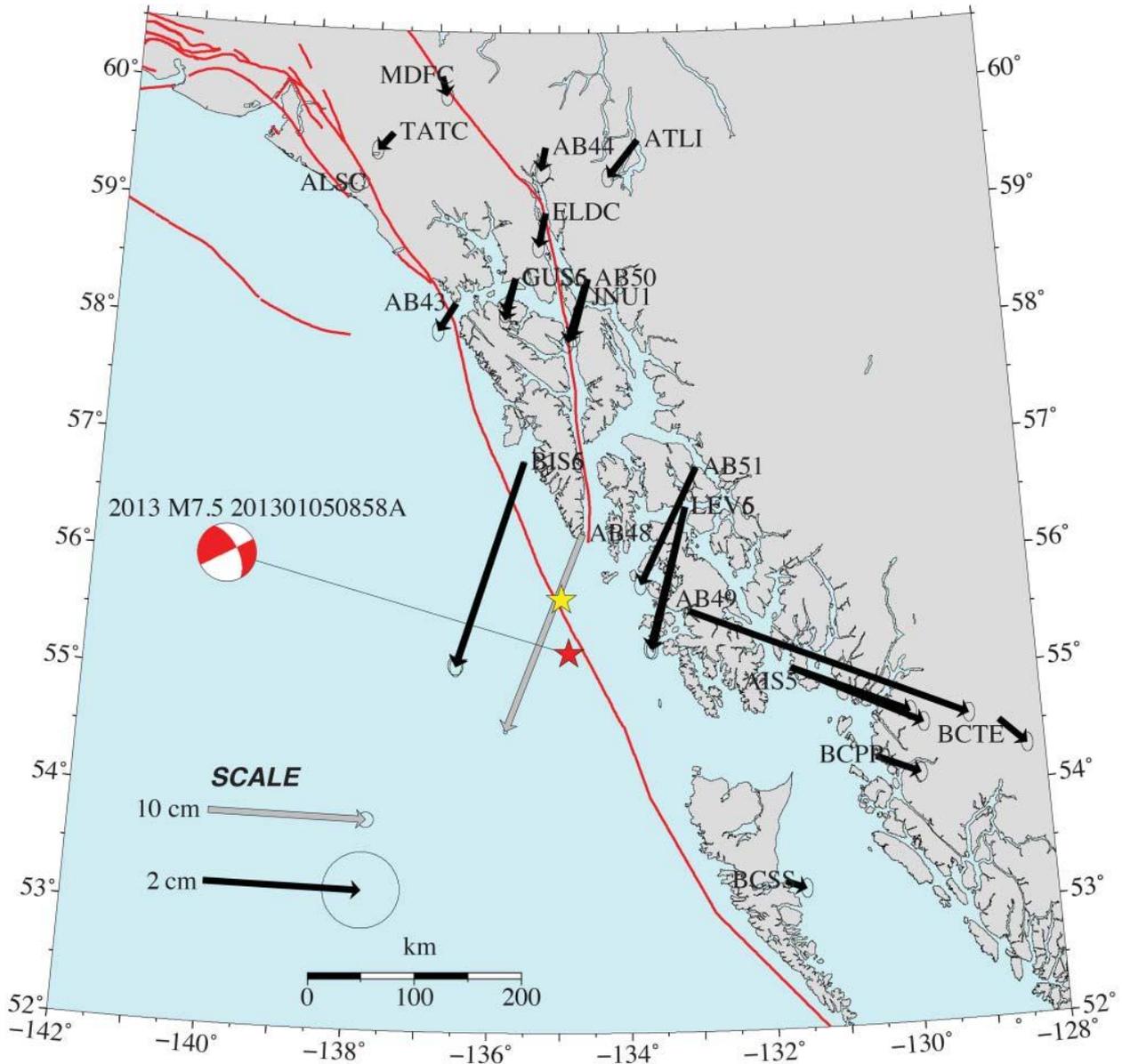
Figure 5.14 Displacements from the 2013 M7.5 Craig earthquake, shown by vectors tipped with 95% confidence ellipses. Displacements were computed in ITRF2014, including regional frame stabilization based on sites located more than 500 km from the epicenter. Other features in the figure are as described in the caption for Figure 5.13. Vertical displacements from this event were small and are not shown.

the event occurred far offshore, only the coarse details of the slip distribution can be determined and the depth distribution of slip was poorly resolved, but the event was clearly shallow. Because of the extensive super-shear rupture (Yue et al., 2013), early coseismic slip distributions based on teleseismic data that had an assumption of subshear rupture velocity, such as the USGS finite fault model, were too compact and thus predicted near-field displacements poorly. Postseismic displacements over the first 1.6 years were as large as ~30 mm (at site AC48, the site closest to the earthquake). The postseismic transient time series could be fit with a logarithmic relaxation with a relaxation time of 56 days. The postseismic displacements could be well fit by a model of afterslip downdip of the coseismic rupture, but the inferred afterslip patch was shifted southward relative to the coseismic slip (Ding
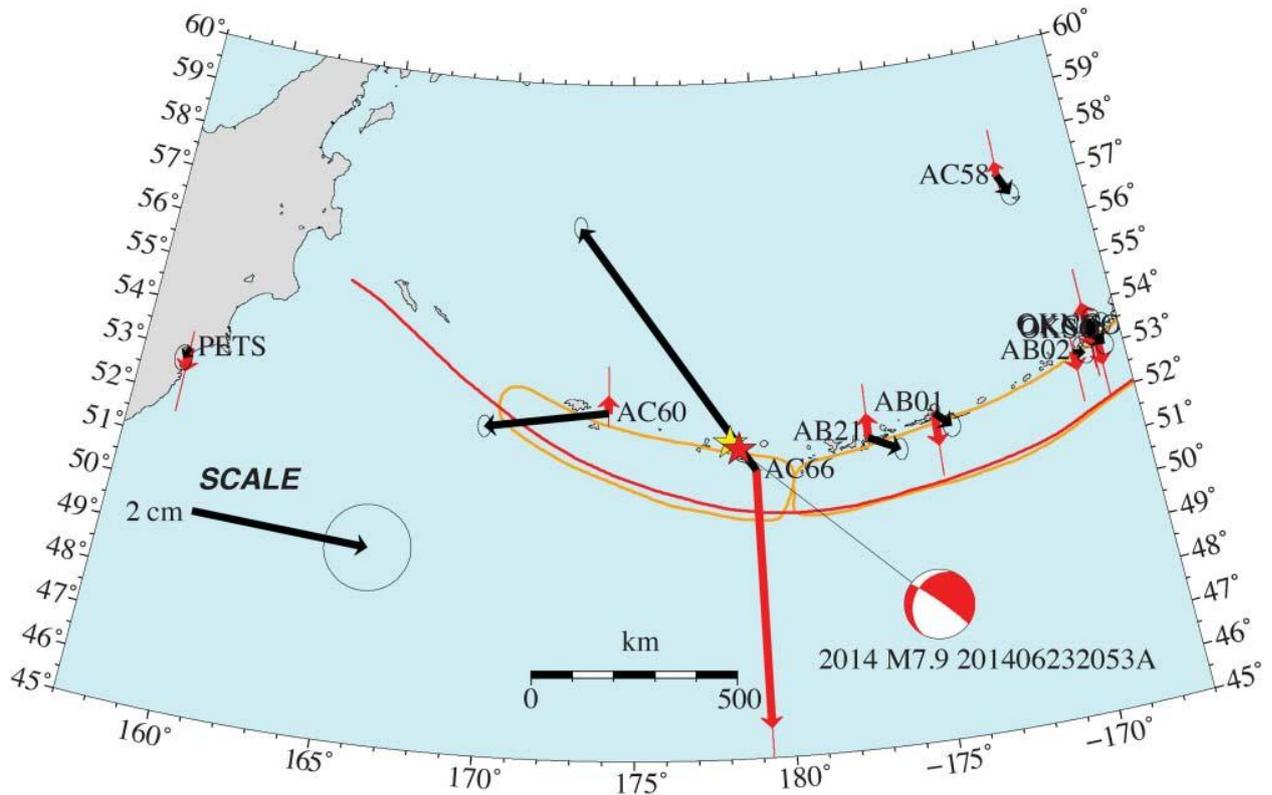
Figure 5.15 Displacements from the 2014 Little Sitkin earthquake, shown by vectors tipped with 95% confidence ellipses. Red vectors indicate vertical displacements, where north-pointing arrows indicate uplift, and vertical displacement 95% confidence uncertainty is shown by a red bar. Displacements are computed in ITRF2014. Other features in the figure are as described in the caption for Figure 5.13. Orange outlines show the approximate rupture areas of the 1957 M8.6 (east) and 1965 M8.7 (west) great earthquakes (Sykes et al., 1980).

et al., 2015). It remains unclear whether this truly reflected an example of along-strike afterslip or was related to some issue with model resolution.

Little Sitkin Earthquake (M7.9, 23 June 2014)

A deep earthquake (~105 km depth) ruptured the subducted Pacific Plate beneath the islands of Little Sitkin and Amchitka in the Western Aleutians (Macpherson & Ruppert, 2015). The PBO/NOTA network is very sparse in that region, but significant displacements were recorded at the sites AC66 (Amchitka), AC60 (Shemya), AB21 (Atka), AB01 (Nikolski), and AC58 (St. Paul, Pribilof Islands) (Figure 5.15). Very small displacements were observed at more distant sites. The horizontal and vertical displacements at the site AC66 on Amchitka exceeded 30 mm, but most observed static displacements were smaller than 10 mm.

For deep events such as this one, it can be difficult to distinguish between the two possible fault planes defined by the focal mechanism as the data resolve a few details of the source. Twardzik and Ji (2015) concluded that the steeply dipping (84°) plane striking 309° was the fault plane, based on a Joint Hypocenter Determination of the mainshock and aftershocks and a finite-fault model using teleseismic data. Ye et al. (2016) combined high-rate and static GPS displacements with teleseismic records to estimate both point source and finite fault slip models for this event. The near-field GPS displacements are better fit by rupture on a shallowly dipping fault plane, but the steeply dipping plane could explain the data if the hypocentral location is shifted by >15 km. Ye et al. (2016) developed a simple five-segment finite rupture model, indicating a slip zone ~50 km long and ~30 km wide on the shallowly dipping plane.

Iniskin Earthquake (M7.1, 24 January 2016)

The 2016 Iniskin earthquake ruptured the subducted plate at a depth of ~110 km beneath the Iniskin Peninsula, Cook Inlet. It produced ~10 mm horizontal and vertical displacements across the whole Cook Inlet region (Figure 5.16) and caused shaking related damage in communities on the Kenai Peninsula and in Anchorage.
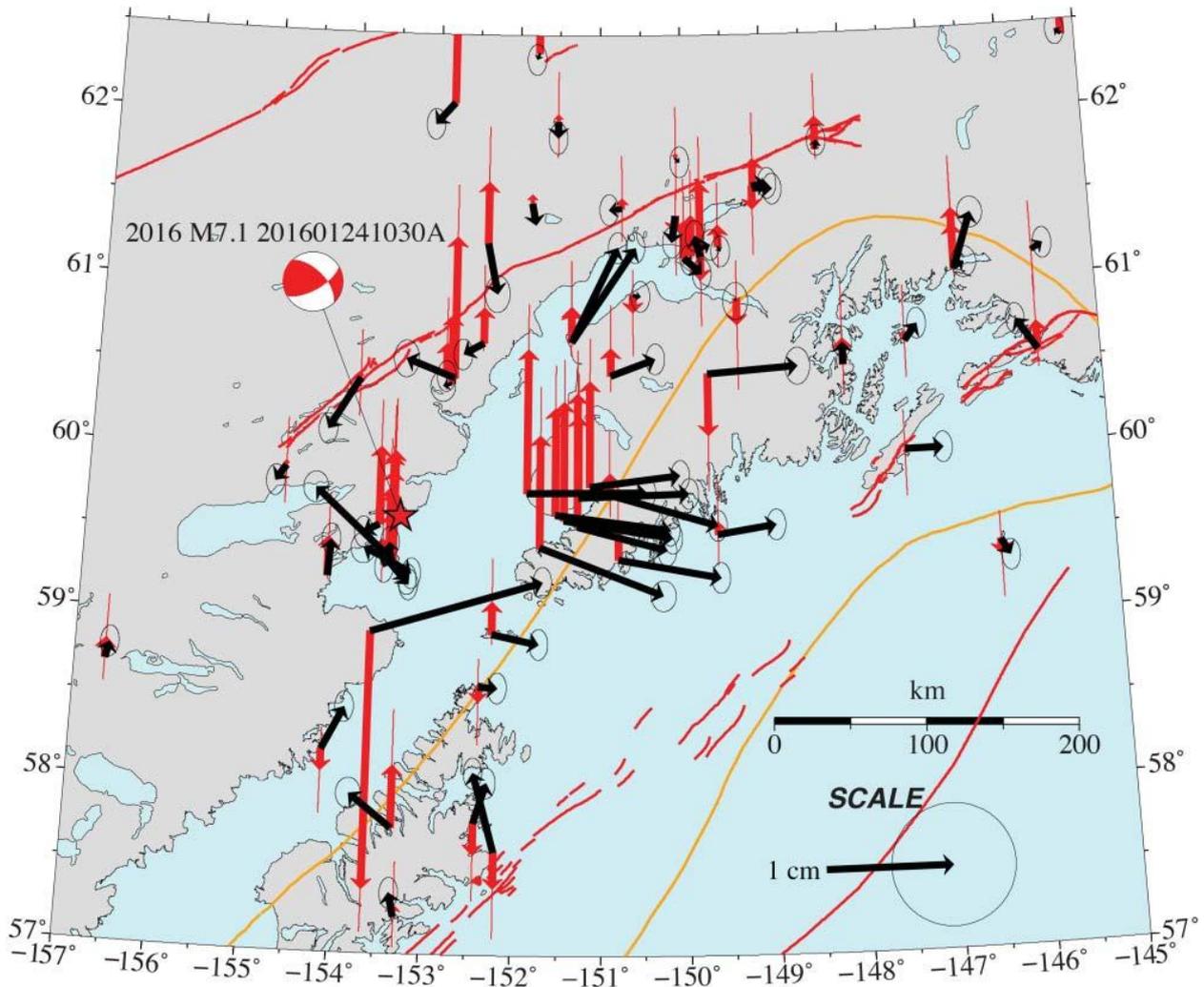
Figure 5.16 Displacements from the 2016 M7.1 Iniskin earthquake, shown by vectors tipped with 95% confidence ellipses. Red vectors indicate vertical displacements, where north-pointing arrows indicate uplift and the 95% confidence interval for the vertical displacement is shown by a red bar. Displacements are computed in ITRF2014. Red star shows the USGS location. Other features in the figure are as described in the caption for Figure 5.13. Orange outlines show the approximate rupture area of the 1964 M9.2 Alaska earthquake (Sykes et al., 1980).

No geodetic slip model has been estimated for this earthquake. Grapenthin et al. (2017) used the event as a case study for the application of GPS data to Earthquake Early Warning. Grapenthin et al. (2018) computed GPS velocity records using single-frequency observations, filtered to isolate the main frequencies of strong ground shaking. They showed that the GPS velocity records faithfully recorded the ground motion amplification within the Cook Inlet Basin, which demonstrated that GPS kinematic solutions can be used effectively and interchangeably with seismic waveforms within their common frequency band.

Haines/Duke River Earthquake Doublet (M6.2 and M6.3, 1 May 2017)

Two earthquakes, M6.2 and M6.3, struck at ~14 km depth about 2 h apart on 1 May 2017 near the eastern Denali Fault in Yukon Territory, BC, Canada. The two hypocenters were located close together, but the focal mechanisms were different, indicating rupture of two different faults. One event had a roughly strike-slip mechanism and the other mainly thrust. A displacement of ~10 mm for the sum of the two events was observed at the near-field site MDFC, and other sites within ~150 km of the events had displacements of a few to several
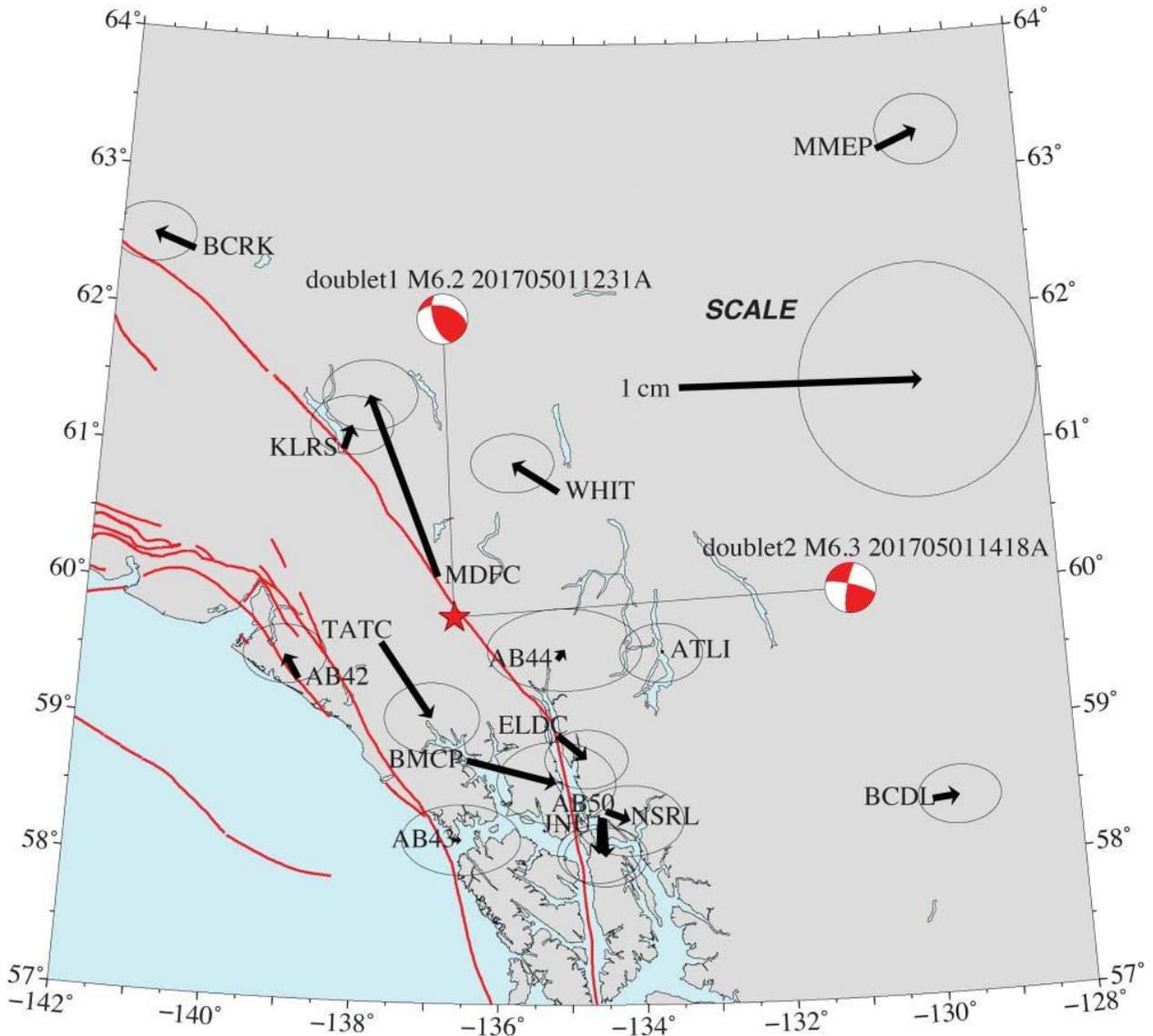
Figure 5.17 Displacements from the 2017 Haines/Duke River earthquake doublet, shown by vectors tipped by 95% confidence ellipses. Displacements are computed in ITRF2014. Vertical displacements from this event were small and are not shown. Red stars show the USGS locations for the earthquakes. Other features in the figure are as described in the caption for Figure 5.13.

millimeters (Figure 5.17). He et al. (2018) analyzed teleseismic and regional seismic waveforms to study the rupture processes of the two events. The near-field GPS displacement at campaign site TRTH, located very close to the epicenters, proved to be critical in distinguishing between the primary and auxiliary fault planes for the two events. The continuous site data shown in Figure 5.17 were not available at the time of the analysis of He et al. (2018) because the sites closest to the rupture (MDFC, TATC, and BMCP) were recording on-site and were

not downloaded until summer 2019. He et al. (2018) determined that the first event ruptured an SW-dipping fault with a primarily thrust mechanism, and the second event ruptured along an unmapped left-lateral strike-slip fault. Thus, neither of these events could have occurred on the (right-lateral) Denali Fault, but instead they represent part of a complex zone of faulting associated with the intersection of the Denali and Duke River faults (Figure 5.1). Feng et al. (2019) analyzed ALOS-2 InSAR interferograms for the events and came to the same
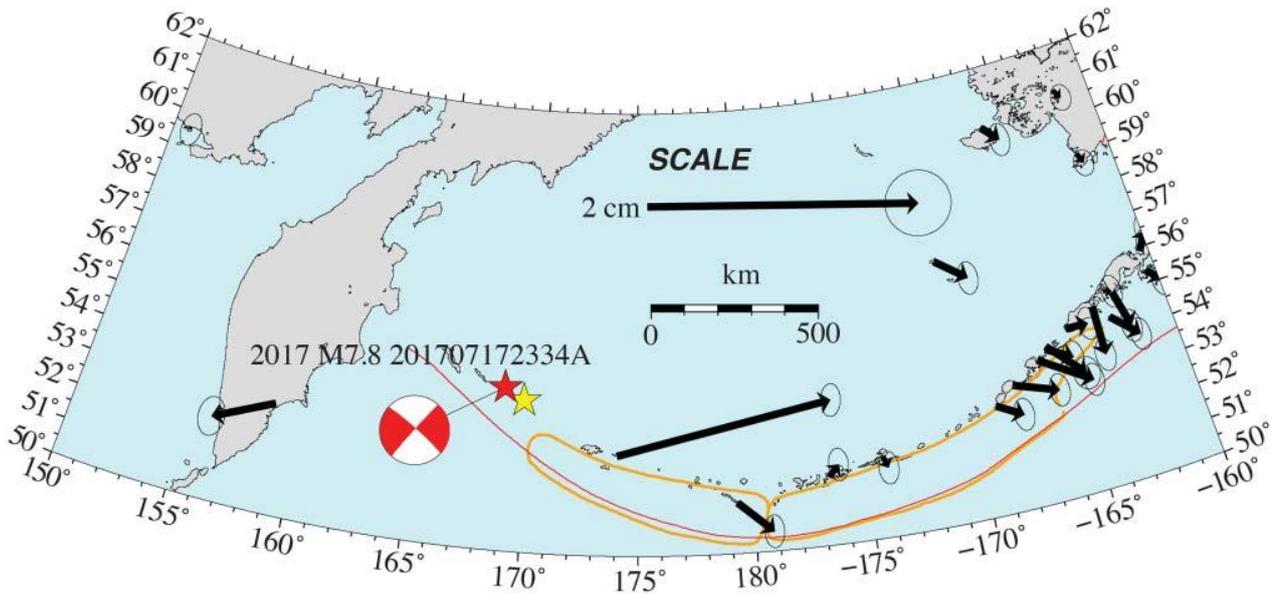
Figure 5.18 Displacements from the 2017 M7.8 Komandorsky earthquake, shown by vectors tipped with 95% confidence ellipses. For clarity, only a few selected sites in the eastern Aleutians are shown. Displacements are computed in ITRF2014. Vertical displacements from this event were small and are not shown. Other features in the figure are as described in the caption for Figure 5.13. Orange outlines show the approximate rupture areas of the 1957 M8.6 (east) and 1965 M8.7 (west) great earthquakes (Sykes et al., 1980).

conclusion. The earthquake doublet mechanisms are in line with the regional GPS velocities and block model predictions of transpression across this area (e.g., Elliott & Freymueller, 2020a; Figure 5.8).

Komandorsky Earthquake (M7.8, 17 July 2017)

A large, shallow, strike-slip earthquake ruptured along the Bering-Kresta trough north of the Komandorsky Islands (Russia), in the westernmost part of the Aleutian arc (Figure 5.18). Slip partitioning in the western Aleutians increases with distance to the west, with the Aleutian arc itself moving in a trench-parallel direction toward Kamchatka at a rate reaching a few centimeters per year (Avé Lallemant & Oldow, 2000; Cross & Freymueller, 2008). Shortly before the earthquake, Kogan et al. (2017) estimated that the Komandorsky arc massif moves 51 mm/year trench-parallel toward Kamchatka, based on modeling of interseismic velocities.

This rapid motion is accommodated on a strike-slip fault north of the islands, which they proposed was located within the Bering-Kresta trough immediately north of the arc (the Bering Fracture Zone). The 2017 event ruptured for 400 km along the Bering Fracture Zone (Lay et al., 2017), exactly as proposed based by Kogan et al. (2017) on the interpretation of the interseismic models. The event ruptured mainly within the upper 15 km and was comparable in length and magnitude to the 1906 San Francisco earthquake. Lay et al. (2017)

estimated that the average slip in the earthquake was comparable to the total accumulated slip deficit since the last earthquakes on the fault in 1849 and 1858, given the 51 mm/year slip rate.

Within Alaska, the earthquake caused a displacement of ~15 mm at site AC60 (Shemya), and smaller but still detectable displacements were observed across the entire Bering Sea region and Kamchatka (Figure 5.18).

Offshore Kodiak Earthquake (M7.9, 23 January 2018)

An intriguing event ruptured a complex network of faults within the Pacific Plate crust in the Gulf of Alaska, offshore of Kodiak Island. The earthquake occurred near the outer rise, outboard of the trench, but did not involve trench-parallel extension or contraction, as would be expected for a plate bending fault. Instead, the earthquake ruptured an array of roughly orthogonal, vertical strike-slip faults that extended over a ~100 × 100 km region (Ruppert et al., 2018; Krabbenhoeft et al., 2018). Displacements from this event were detectable across almost all of Alaska and the adjacent parts of Canada (Figure 5.19). This includes small but coherent displacements across the Mackenzie Mountains (Northwest Territories, Canada; Figure 5.1), at the extreme upper right part of the figure.

The inferred array of faults includes both right-lateral faults striking ~N–S or left-lateral faults striking ~E–W. Aftershocks show predominantly ~N–S lineations
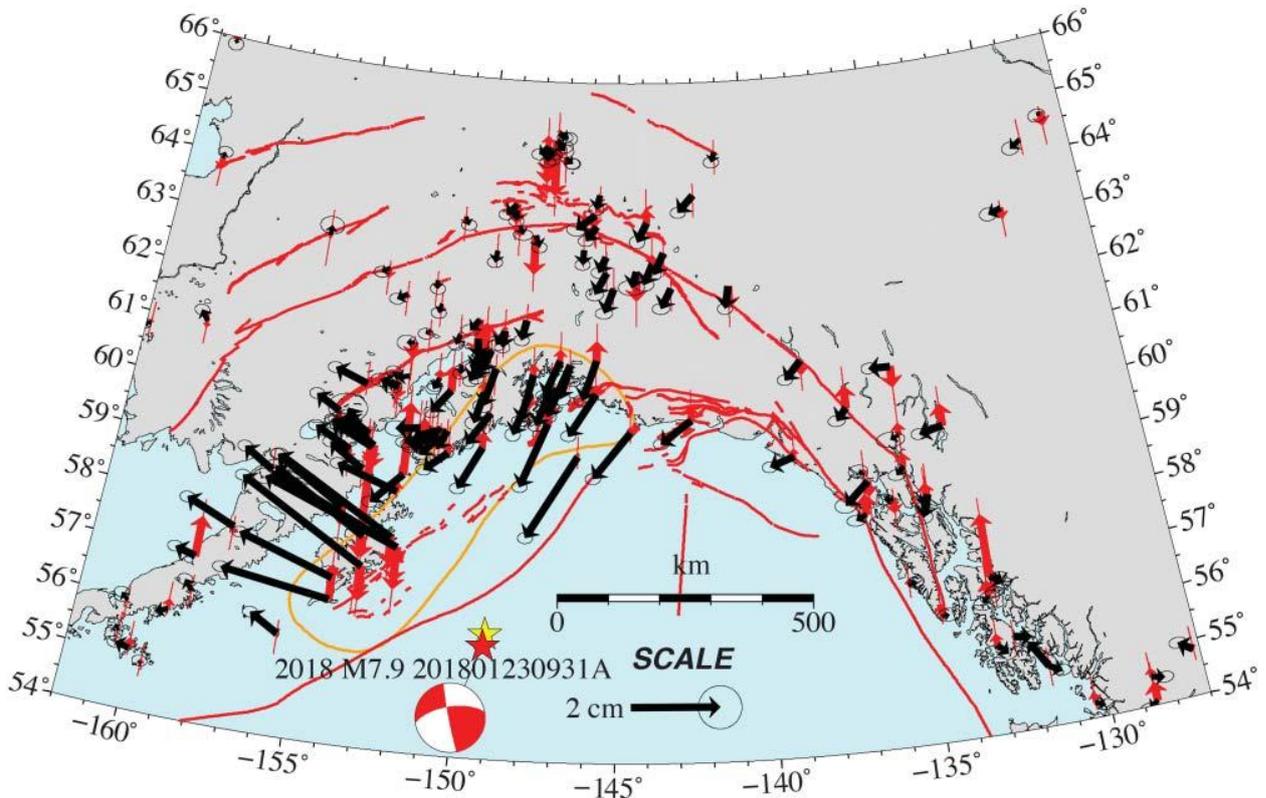
Figure 5.19 Displacements from the 2018 M7.9 Offshore Kodiak earthquake, shown by vectors tipped with 95% confidence ellipses. Red vectors indicate vertical displacements, where north-pointing arrows indicate uplift and vertical displacement 95% confidence uncertainty is shown by a red bar. Displacements are computed in ITRF2014. This figure includes displacements from several remotely recording sites in southeast Alaska and Canada that were not available at the time of the work of Ruppert et al. (2018), because the sites were not downloaded until 2019. Other features in the figure are as described in the caption for Figure 5.13. Orange outlines show the approximate rupture area of the 1964 M9.2 Great Alaska earthquake (Sykes et al., 1980).

(Figure 5.20), but it was not possible to fit the observed GPS displacements with slip only on the ∼N–S faults. A single ∼E–W fault segment could reasonably approximate the observed displacements, but the slip distribution inferred from a single-fault model had the maximum slip at the far northeast end of the model fault, where back projection did not locate any significant high-frequency radiation (Ruppert et al., 2018). The fit to the observations improved with a more complex fault model, and their final fault model included six fault segments in total (Figure 5.20b).

This event has a number of similarities to the 2012 M_W 8.6 and M_W 8.2 Wharton Basin earthquakes, offshore of western Sumatra (Hill et al., 2015; Singh et al., 2017; Wei et al., 2013). Like the Kodiak event, the largest of the Wharton Basin sequence ruptured a set of nearly orthogonal faults, extending over an even larger area than the smaller event offshore of Alaska. The majority of slip occurred on WNW-trending faults rather than the faults

that are more evident in the bathymetry. The seismic moment of the Wharton Basin event was large because of the number of faults ruptured and high slip at lithospheric mantle depths, within high rigidity material. Singh et al. (2017) later used new high-resolution bathymetry and seismic reflection data to identify the WNW-trending faults that had high slip in that event. Unlike the Offshore Kodiak event, the Wharton Basin event had aftershocks that outlined all of the fault traces with major slip.

The Wharton Basin has been interpreted as the location of a nascent plate boundary, part of the process of breakup of the former Indo-Australian plate (Coudurier-Curveur et al., 2020), with estimated slip rates of 0.8–2.5 mm/year on some of the faults that could be identified from bathymetric mapping and seismic imaging. The North Pacific seafloor south of Alaska has not been studied so intensively, but we propose that the Pacific Plate may be deforming internally and perhaps beginning to break apart as well. Internal deformation of
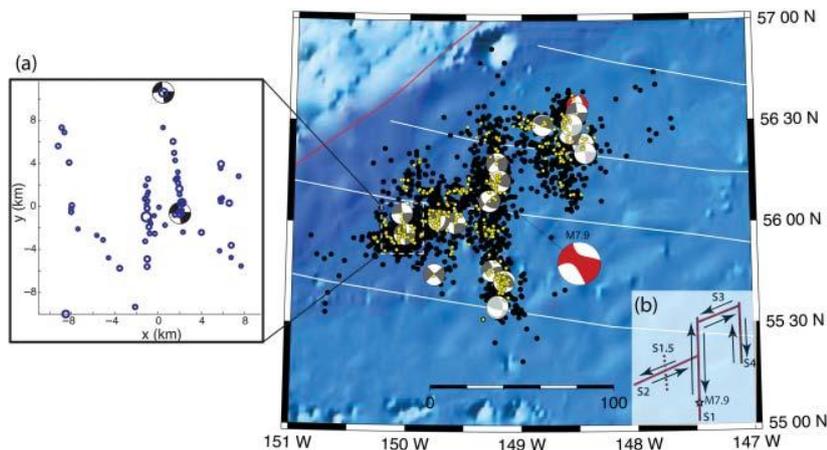
Figure 5.20 Map of aftershocks and moment tensor solutions following the 2018 Offshore Kodiak earthquake, from Ruppert et al. (2018)/John Wiley & Sons. (a) Enlargement of a portion of the aftershock sequence, showing clear N–S-striking faulting. (b) The final fault geometry and sense of slip.

the northeast corner of the Pacific Plate is also seen in the 1987–1988 Gulf of Alaska earthquake sequence, located ~400 km to the northeast (Pegler & Das, 1996; Sauber et al., 1993). The two largest events in the 1987–1988 sequence ruptured N–S-striking right-lateral strike-slip faults, suggestive of a more mature stage of fault development. However, some of the smaller events in the sequence ruptured E–W-trending left-lateral strike-slip faults. This internal deformation of the Pacific Plate may be due to stresses being transmitted outboard from the collision and subduction systems (Elliott et al., 2013; Krabbenhoeft et al., 2018).

Anchorage Earthquake (M7.1, 30 November 2018)

Another large event within the subducted plate struck beneath the Susitna Valley just north of Anchorage in November 2018, at a depth of ~50 km. It is located near the western edge of the subducted Yakutat slab crust (Kim et al., 2014). The earthquake caused roadway and other damage across the region and caused coherent horizontal displacements as much as 200–300 km away (Figure 5.21).

Liu et al. (2019) estimated a slip model based on static and high-rate GPS displacements and near-field strong motion seismic data. They found it difficult to determine the fault plane, with both alternate fault planes producing a similar fit to the data. Ruppert et al. (2020) produced an extensive catalog of aftershocks and relocated 2038 events. They found that the aftershocks were located predominantly in two clusters, a diffuse one to the south and a steeply dipping one to the north. Guo et al. (2020) used this aftershock catalog and near-field strong motion data to infer that both candidate faults had ruptured in the event.

It is not clear whether a single fault plane or rupture of two conjugate planes best explains this event. For example, although the alignments of the two fault planes proposed by Guo et al. (2020) match the alignments of the aftershock clusters, the location of one of the two proposed segments is shifted at least 10 km away from the aftershocks.

Simeonof Earthquake (M7.8, 22 July 2020)

The July 2020 M7.8 Simeonof earthquake (Figure 5.22) began a sequence of events offshore of the Alaska Peninsula that later included the October 2020 M7.6 Sand Point earthquake and the July 2021 M8.2 Chignik earthquake (Figures 5.10, 5.24 and 5.25). The earthquake ruptured beneath the eastern Shumagin Islands and continued with lower slip further to the west, through the eastern part of what had been identified as the Shumagin seismic gap (Crowell & Melgar, 2020; Liu et al., 2020; Xiao et al., 2021; Ye et al., 2021; Zhao et al., 2022). Xiao et al. (2021) included static and kinematic GPS displacements in their slip model, along with InSAR displacements, and regional and teleseismic waveforms. The various finite fault slip models generally agree that most of the slip occurred between 20 and 40 km depth, and the earthquake produced only a minor tsunami. Data from one GPS-Acoustic site offshore the rupture support the land-based data conclusion that coseismic slip was limited to intermediate depths and did not propagate into the shallower region of the megathrust (DeSanto et al., 2023). Measurable displacements extended for at least 700–800 km, with coherent displacements at the ~1 mm level observed as far north as the Seward Peninsula, ~1100 km north of the rupture (Figure 5.22).

This earthquake provided a rare opportunity to develop a slip budget over a complete, century-long earthquake
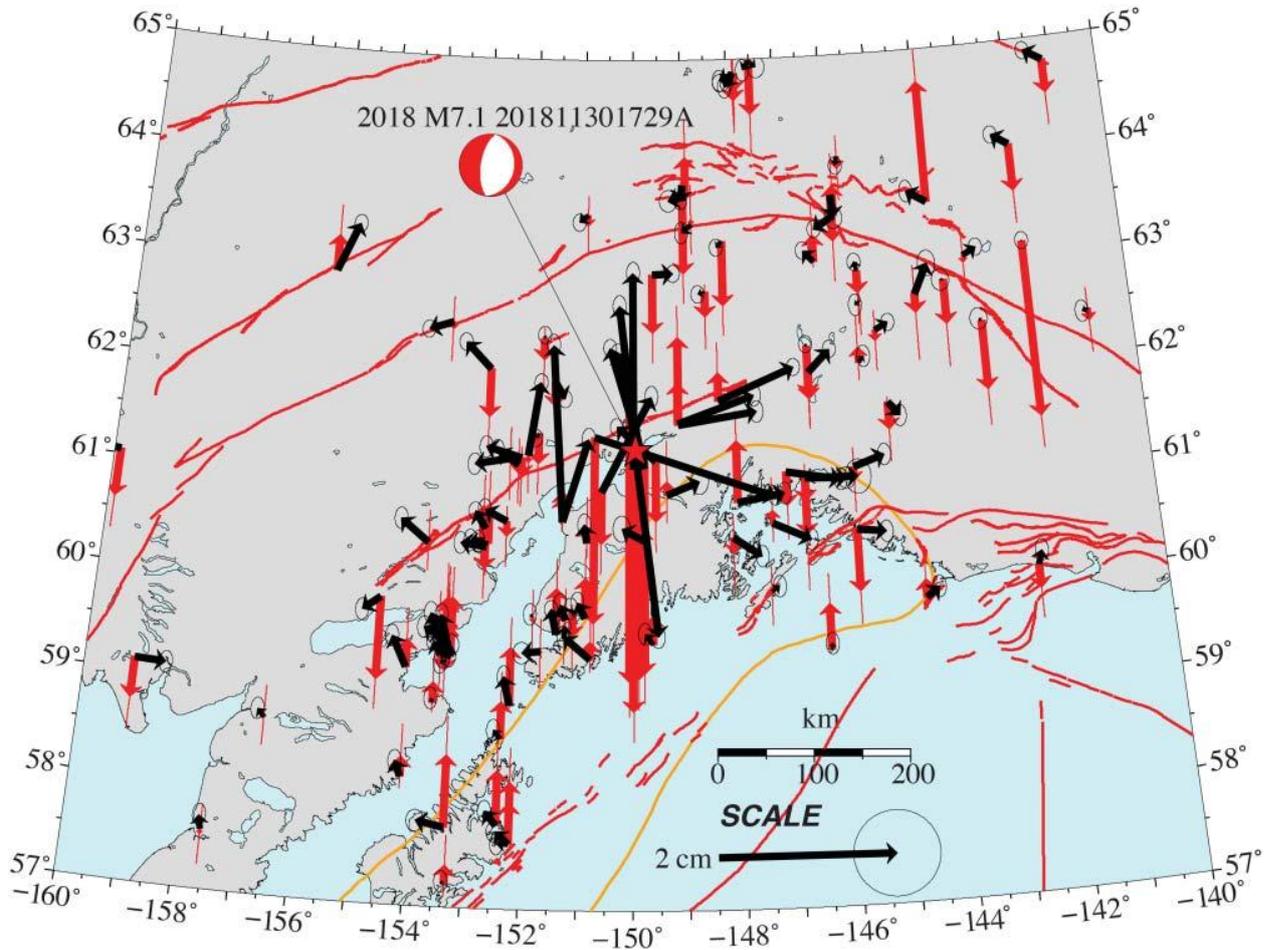
Figure 5.21 Displacements from the 2018 M7.1 Anchorage earthquake, shown by vectors tipped with 95% confidence ellipses. Red vectors indicate vertical displacements, where north-pointing arrows indicate uplift and vertical displacement 95% confidence uncertainty is shown by a red bar. Displacements are computed in ITRF2014. Sites with isolated, large vertical displacements are likely outliers, although these observations persist even with a regional reference frame stabilization. Red star shows USGS location. Other features in the figure are as described in the caption for Figure 5.13. The orange outline shows the approximate rupture area of the 1964 M9.2 Great Alaska earthquake (Sykes et al., 1980).

cycle. The last similar-sized earthquake that likely ruptured the same part of the subduction interface was in 1917, giving an interpreted recurrence interval of 113 years (Ye et al., 2021). Xiao et al. (2021) compared the slip as a function of depth in the Simeonof earthquake with the total century-long accumulated slip deficit, based on two alternative models of interseismic slip deficit (Figure 5.23). The two alternative models differ in the regularization of the inversion. The Drooff and Freymueller (2021) model (Figure 5.23a) assumed that the slip deficit could decrease with depth, but not increase, forcing the maximum slip deficit to be at the trench. The alternative model (Figure 5.23b) assumed a Gaussian shape to the slip deficit distribution with depth, although

the peak could be at any depth. These two models fit the data about equally well, which is a common situation given the lack of model resolution in the near-trench area (e.g., Schmalzle et al., 2014). Although the two models are visually quite different, the slip deficit distributions (blue and green curves in the lower panels) are similar outside of the near-trench area, with the Gaussian model having a 10%–20% higher slip deficit rate at depths below 20 km. Within the depth range of the 2020 main rupture area (25–40 km), the 2020 event slip was essentially equal to the century-long slip deficit. However, at shallow depth both models predict a substantial remaining slip budget, to be released by some mode of slip in the future. It is not yet clear whether shallow afterslip could account for the
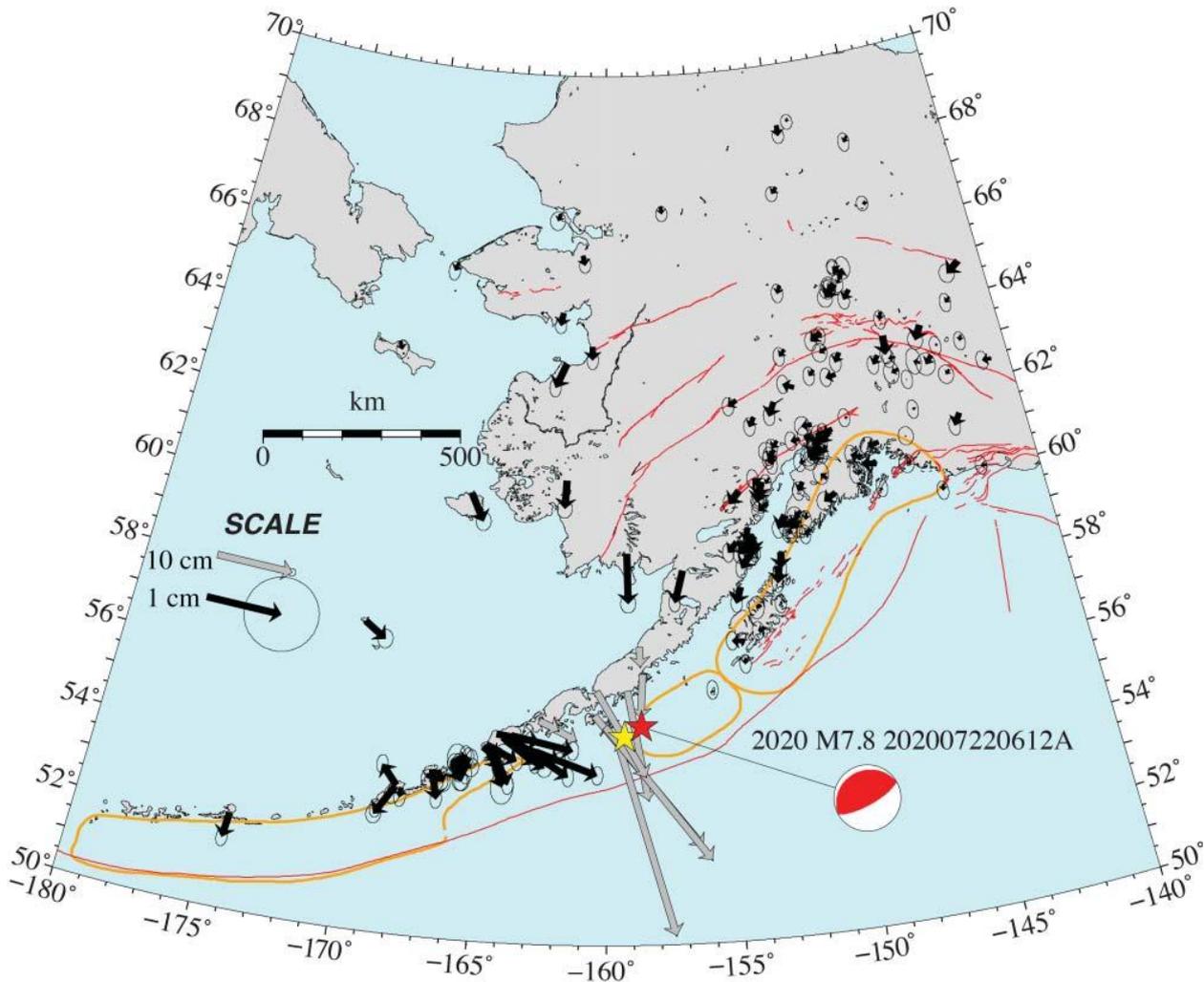
Figure 5.22 Displacements from the 2020 M7.8 Simeonof earthquake, shown by vectors tipped with 95% confidence ellipses. The near-field displacements are shown with gray vectors, at 1/10 the scale of the far-field displacements. Displacements are computed in ITRF2014. Vertical displacements are not shown. Other features in the figure are as described in the caption for Figure 5.13. The orange outlines show the approximate rupture area of the 1964 M9.2 Great Alaska earthquake (east), the 1938 M8.3 Alaska Peninsula earthquake (center), and the 1957 M8.6 Andreanof Islands earthquake (Sykes et al., 1980).

needed slip, or if future large shallow earthquakes would be required.

Sand Point Earthquake (M7.6, 19 October 2020)

Three months after the Simeonof earthquake, the Sand Point earthquake occurred 80 km to the southwest (Figure 5.24). Unlike the Simeonof earthquake, Sand Point was a dominantly strike-slip event that ruptured within the downgoing Pacific slab (Zhou et al., 2022). The M7.6 earthquake caused small displacements at GPS sites in the region, except at AC12 that was closest to the rupture (Figure 5.24). The earthquake was notable for several reasons. It was one of the largest strike-slip

events in oceanic lithosphere to have occurred over the past few decades (e.g., Choy & McCarr, 2002), joining a group that includes the 2012 Wharton Basin earthquakes (Hill et al., 2015; Singh et al., 2017; Wei et al., 2013), the 2018 Offshore Kodiak event discussed above, and the 1987–1992 series of M7+ earthquakes along the Gulf of Alaska shear zone (e.g., Pegler & Das, 1996). While the Global CMT solution suggests a fault plane with a 350° strike and 49° dip, there is not a known structure of that orientation within the Pacific Plate in the region (Herman & Furlong, 2021). While aftershocks are distributed along this geometry, they also extend into the overriding plate. Finally, the Sand Point earthquake generated a larger
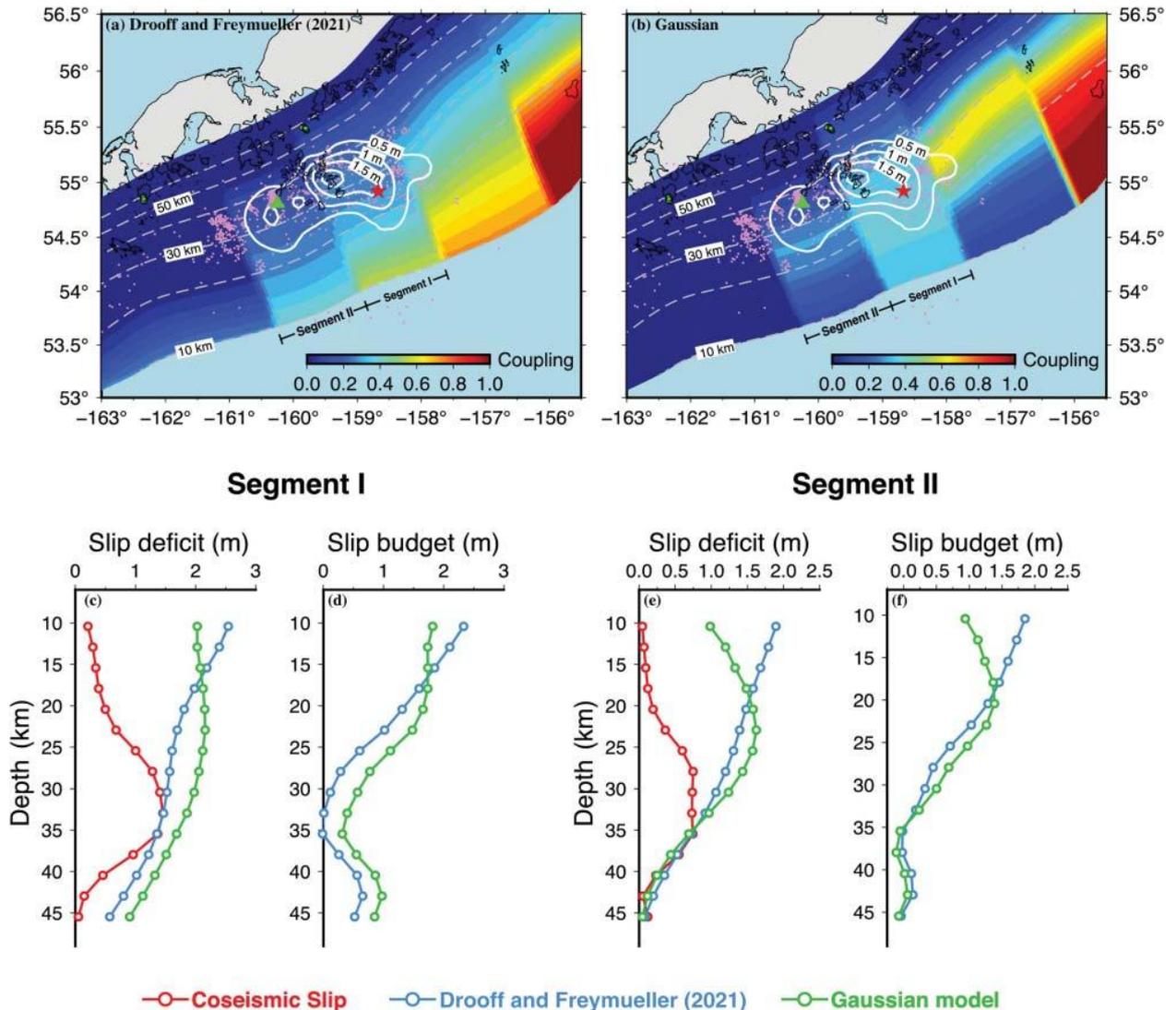
Figure 5.23 Slip model and slip budget from Xiao et al. (2021)/with permission of ELSEVIER.

tsunami than the Simeonof megathrust event despite being strike-slip event (Mulia et al., 2022).

Herman and Furlong (2021) suggested that a coupling boundary, where the coupling was higher to the east than to the west of the boundary, may have led to the occurrence of the earthquake. Coulomb stress modeling showed that the difference in coupling would result in stress loading that would be favorable to right-lateral strike-slip faulting perpendicular to the trench within the oceanic crust. In addition, stresses imposed by the earlier Simeonof earthquake may have promoted the Sand Point earthquake (Herman & Furlong, 2021).

Using a combination of static GPS and teleseismic waveform data as constraints, Elliott et al. (2022) found that strike-slip motion on a dipping fault plane alone

could provide a good fit to the geodetic and seismic data but did not fully explain the tsunami waveforms. Bai et al. (2023) used teleseismic waveforms, regional broadband and strong motion data, GPS offsets, high-rate GPS time series, and tsunami data to evaluate the Sand Point earthquake. They proposed a much more complex fault system, including an eastward dipping north–south striking fault in the Pacific Plate and a north-dipping normal fault in the upper plate below the continental shelf. While this model fit the data and produced a seismic moment equivalent to an M_w 7.5, it did not reproduce the tsunami observations. To better fit the tsunami data, Bai et al. (2023) added a fault with a strike of 190° and a westward dip of 30° under the continental shelf. They proposed that this fault experienced slow rupture lasting over 5 min,
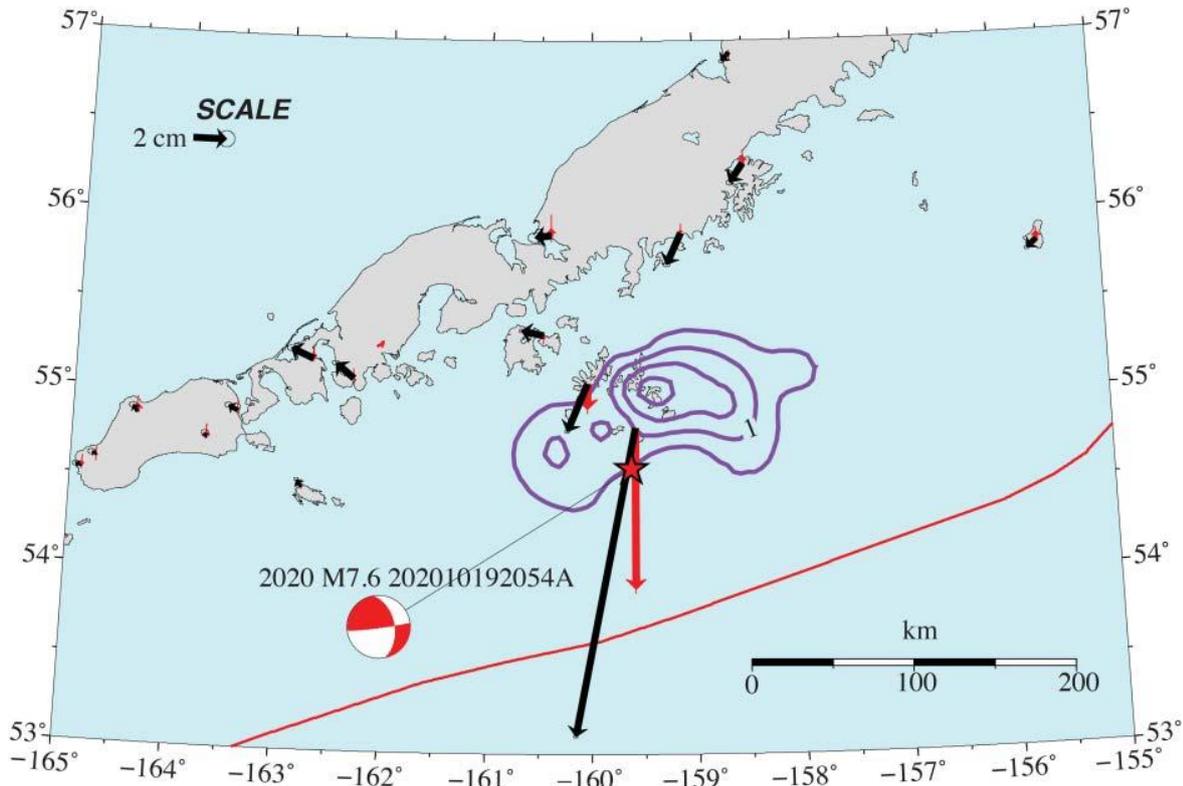
Figure 5.24 Displacements from the 2020 M7.6 Sand Point earthquake, shown by vectors tipped with 95% confidence ellipses. Red vectors indicate vertical displacements, where north-pointing arrows indicate uplift and vertical displacement 95% confidence uncertainty is shown by a red bar. Displacements are computed in ITRF2014. Red star shows USGS location. Other features in the figure are as described in the caption for Figure 5.13. The purple contours show the slip contours for the 2020 M7.8 Simeonof earthquake (Xiao et al., 2021).

which would explain the tsunami data without impacting the geodetic or seismic data that were well fit by fast slip along the other two faults.

Chignik Earthquake (M8.2, 29 July 2021)

The 2021 Chignik earthquake initiated just to the northeast of the hypocenter of the 2020 Simeonof earthquake, making the rupture zones essentially abutting (Figure 5.10). While the 2020 event ruptured to the southwest, the 2021 event ruptured to the northeast with substantially larger slip and a larger rupture area (Elliott et al., 2022). The Chignik earthquake clearly caused measurable displacements across all of NW Alaska, in addition to displacements of a few decimeters in the near-source area (Figure 5.25). Like the Simeonof earthquake, the Chignik earthquake ruptured mainly in the 20–40 km depth range (Elliott et al., 2022; Liu et al., 2022; Ye et al., 2022). More recently, Brooks et al. (2023) used the displacement of a seafloor GPS-Acoustic site on the outer trench wall offshore of this rupture area to suggest that slip may have extended to shallower depth. However, that measurement includes 2.5 months of postseismic

displacements, so it is very possible that this represents a combination of postseismic slip and rapid afterslip. Evidence of rapid afterslip is displayed in the time series of the cGPS site on Chirikof Island, AC13 (Figure 5.3).

Stress changes due to the 2020 Simeonof earthquake promoted the occurrence of the Chignik earthquake, and these two earthquakes partially filled a major gap in the Alaska–Aleutian subduction zone, suggesting that they may be part of an 80-year-long rupture cascade (Elliott et al., 2022).

1938 M8.3 Alaska Peninsula Earthquake

Based on its aftershock area, the 1938 M_W8.3 earthquake was presumed to have ruptured from the eastern edge of the Shumagin Islands in the west to somewhere between the Semidi Islands and Kodiak Island in the east (Figure 5.10). Based on the aftershock distribution, the earthquake had long been presumed to have a very large rupture area for its estimated magnitude, which implied just a few meters average slip. It generated only a modest tsunami, which Johnson and Satake (1994) explained in their model by slip confined to >20 km depth. The recent
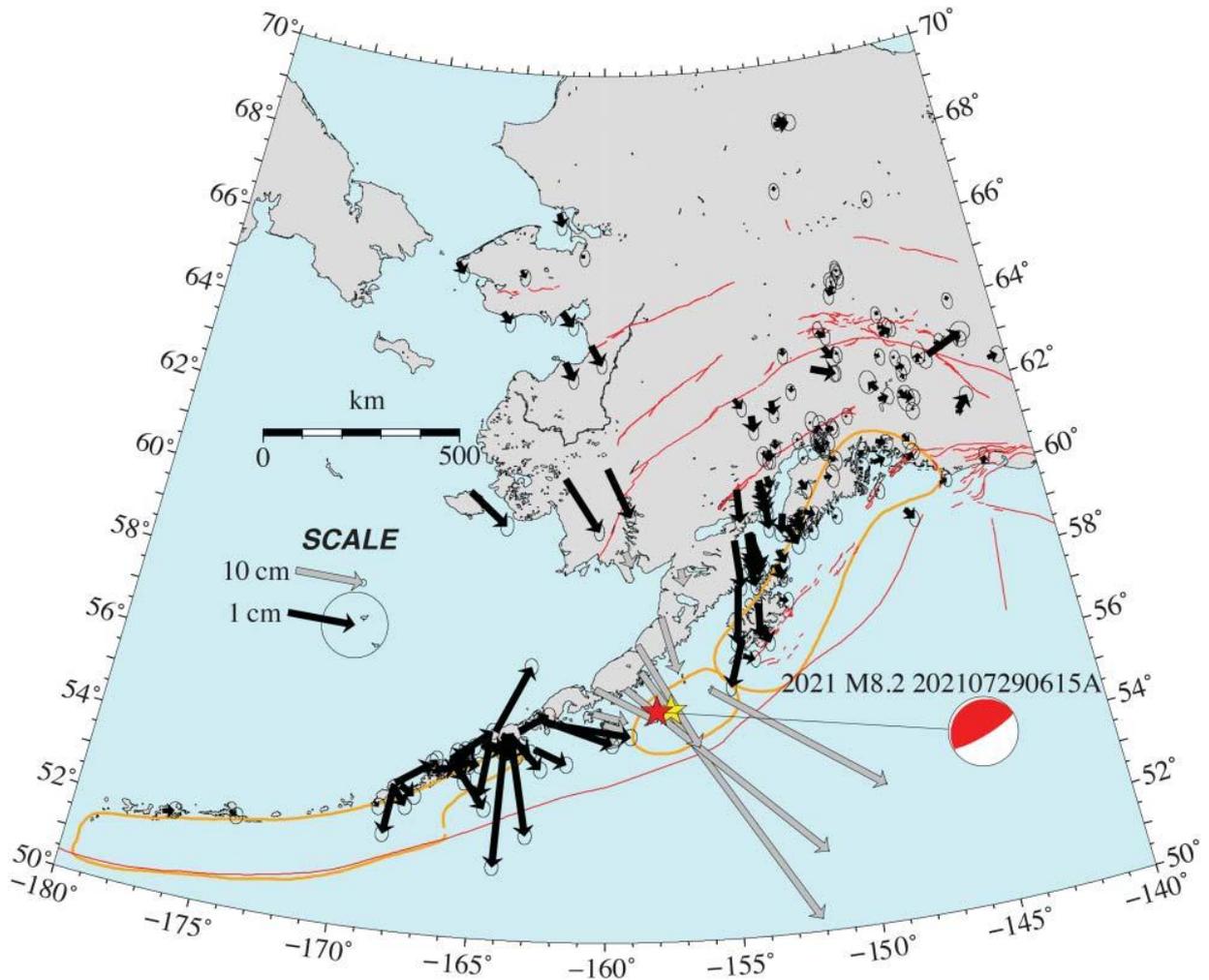
Figure 5.25 Displacements from the 2021 Chignik earthquake, shown by vectors tipped with 95% confidence ellipses. The near-field displacements are shown with gray vectors, at 1/10 the scale of the far-field displacements. Displacements are computed in ITRF2014. Vertical displacements are not shown. Other features in the figure are as described in the caption for Figure 5.13. The orange outlines show the approximate rupture area of the 1964 M9.2 Great Alaska earthquake (east), the 1938 M8.3 Alaska Peninsula earthquake (center), and the 1957 M8.6 Andreanof Islands earthquake (Sykes et al., 1980).

2021 M_W 8.2 Chignik earthquake likely overlapped with the 1938 rupture zone (in along-strike extent), and the 2020 M_W 7.8 Simeonof earthquake rupture fell within the 1938 aftershock zone.

Freymueller et al. (2021) re-analyzed the instrumental tsunami recordings from 1938 earthquake along the Alaska Peninsula. Some of the original mareograms had been lost, and the published figures of Johnson and Satake (1994) lacked key timing information. Freymueller et al. (2021) were able to recover two records with precise timing and amplitudes, from Unalaska and Sitka. They computed synthetic tsunami records from a grid of hypothetical sources and found that the Sitka record was

sensitive to the depth of slip but not along-strike location, while the reverse was true for the Unalaska record. Using this information, they determined that the earthquake ruptured mainly at shallow depth (but with a low average slip), and slip was concentrated in the eastern part of the previously inferred 1938 rupture. While that study was published before the 2021 Chignik event, their conclusions suggest that the 1938 rupture likely was confined to the shallower part of the megathrust updip of the 2021 event and likely entirely to the east of the 2020 event.

1957 M8.6 Andreanof Islands Earthquake

The 1957 Andreanof Islands Earthquake in the Central Aleutians featured one of the longest coseismic ruptures

of any historical earthquake, rupturing an ~1,200 km long stretch of the Aleutian megathrust from Amchitka Pass in the west to approximately Umnak Island in the east (Figure 5.10). Magnitude estimates for this event have fluctuated between M8.6 and M9.1 (International Seismological Centre, 2023; Okal, 1992), with the lower magnitude being used more frequently. Johnson et al. (1994) developed a finite fault rupture model for the earthquake based on teleseismic and tsunami runup observations. Curiously, that model featured slip in the western one-third of the rupture area, a long stretch with zero slip, and then a further rupture patch around Umnak Island. This model was consistent with the lower magnitude estimates. However, the mapping of tsunami runup (Lander, 1996) clearly suggests more substantial and widespread slip in the eastern part of the rupture, with large runups documented along the Pacific coast of most of the eastern Aleutian islands spanning the easternmost 300–400 km of the rupture.

Recent studies of the 1957 and earlier tsunamis from the eastern end of the rupture area have updated our view of this event and demonstrated that large slip near the trench must have occurred throughout much of the eastern part of the rupture (Nicolsky et al., 2016; Witter et al., 2016). Witter et al. (2016) identified seven tsunami sand sheets in multiple cores and trenches at Stardust Bay on the Pacific coast of Sedanka Island (located trench-ward of Unalaska Island), with the upper six of these being datable. The most recent tsunami sand sheet was identified as the 1957 earthquake deposit, and the oldest dated sand sheet (the sixth) was dated to 1,500 years BP. They observed that the 1957 tsunami had runup of at least 18 m. Nicolsky et al. (2016) then modeled the tsunami propagation and runup in the Unalaska Island region from several hypothetical slip models and demonstrated that both the large observed tsunami runups and the Unalaska tide gauge record could only be explained by high slip at shallow depth on the megathrust across the region. Their best-fitting model featured an average slip of 11.4 m over the 5–15 km depth range and a maximum slip of 20 m centered at 10 km depth.

Taken together, these two studies and the historical record (Lander, 1996) make it clear that the Johnson et al. (1994) model severely underestimated the slip in the earthquake. The model of Johnson et al. (1994) truncated the seismic waveform data used in their inversion so that only data before the arrival of the PP phase were used. House et al. (1981) had earlier suggested that significant direct P-wave energy from later parts of the rupture could have been hidden by the later-arriving PP phases and coda from the early parts of the rupture. Johnson et al. (1994) argued that the amplitude of P arrivals was decaying by this time, but the now-extensive tsunami observations from the eastern part of the rupture make

it clear that the assumption of Johnson et al. (1994) was not correct. Indeed, seismic source models for the 2004 Sumatra–Andaman earthquake, with a similar rupture length, also initially limited all slip to the earliest ~1/3 of the rupture until modeling techniques were revised so that the seismograms covering the full rupture duration could be used.

A complete source model for the 1957 earthquake still does not exist, but it will need to incorporate longer-duration seismic waveforms than those used by Johnson et al. (1994) and make fuller use of the tsunami runup observations.

1964 M9.2 Great Alaska Earthquake

Suito and Freymueller (2009) developed an updated coseismic slip model for the 1964 Great Alaska earthquake. The megathrust slip was modified only slightly from the earlier model of Holdahl and Sauber (1994), but the key innovation was to extend the splay fault rupture southwest off the coast of the Kenai Peninsula from Montague Island where it was observed subaerially. Later, Liberty et al. (2019) showed clear evidence for splay fault ruptures during past megathrust earthquakes. Splay faults made it possible to explain the relatively constant along-strike subsidence observed along the Pacific coast despite the large along-strike reduction in the megathrust slip over the same area.

Suleimani and Freymueller (2020) used tsunami modeling to assess the various coseismic models for the earthquake, using historical reported near-field observations on Kodiak Island and the Kenai Peninsula that had not previously been examined. They examined the near-field predictions of the Suito and Freymueller (2009) model along with the models of Ichinose et al. (2007) and Johnson et al. (1996) (another model based heavily on Holdahl and Sauber (1994)). Although the far-field predictions of the various models were similar, the near-field predictions were dramatically different, with the Suito and Freymueller (2009) model performing much better than the others. The key factors in the improvement were in the shallower dip angle used in that model and the modification of the splay fault.

Suleimani and Freymueller (2020) further examined the splay fault's contribution to the tsunami wavefield, which was substantial in the near field due to the high dip angle and substantial slip to the seafloor. Using observations of arrival times and polarities reported from several locations along the coast of the Kenai Peninsula, they concluded that the splay fault must have extended farther to the southwest than its currently mapped extent on the seafloor (Liberty et al., 2019) but not all the way to the tip of the Kenai Peninsula as suggested by Suito and Frey-mueller (2009). Their model put the termination of the splay fault at the approximate location of the substantial

change in dip angle of the megathrust at the western edge of the subducted Yakutat block crust. That location coincides with a major change in 1964 slip, in interseismic coupling (Figure 5.10), and slab dip angle. Evaluating geologic uplift data and a series of dislocation models, Chapman et al. (2014) found that ~3 m of slip on a splay fault in the vicinity of the Suckling Hills just outboard of the Bering Glacier during the 1964 earthquake could explain the high rates of focused coseismic uplift in the region.

5.5.3. Postseismic Deformation

Large earthquakes usually produce measurable post-seismic transient signals due to afterslip on the fault plane, viscoelastic relaxation, and poroelastic relaxation. Several past review papers have reviewed the mechanisms and observations of postseismic deformation in general (e.g., Bürgmann & Dresen, 2008; Freymueller, 2017, 2020) For the largest events, these postseismic transients can last for decades and affect areas hundreds to thousands of kilometers from the fault plane.

Almost no parts of continental Alaska are completely unaffected by ongoing postseismic transients. However, some studies aimed at modeling active tectonics have neglected to account for this despite a long history of theoretical and modeling studies that have demonstrated the impact on Alaska. In this section, we summarize the findings of previous studies for four major earthquakes, the 1964 M9.2 Great Alaska earthquake, the 2002 M7.9 Denali Fault earthquake, the 2012 M7.8 Haida Gwaii earthquake, and the 2013 M7.6 Craig earthquake. We primarily focus on the documented areal extent and temporal history of postseismic deformation in these cases.

1964 M9.2 Great Alaska Earthquake

Postseismic processes were poorly understood prior to the 1970s, and observations from geodetic leveling in the years following the 1964 M9.2 Great Alaska earthquake were important to establishing both the existence of postseismic deformation and providing clues about the underlying mechanisms. Cohen and Freymueller (2004) summarized the near-field postseismic observations for this event and discussed the papers that had been published up to that time. The earliest observations of postseismic deformation following the 1964 earthquake came from repeat leveling observations along Turnagain Arm of Cook Inlet, immediately south of Anchorage (Brown et al., 1977; Small & Wharton, 1972). These studies demonstrated that up to ~50 cm of relative vertical movement had occurred in the first 11 years after the earthquake. Brown et al. (1977) modeled this deformation as being due to afterslip on a downdip extension

of the coseismic rupture. Later studies (e.g., Suito & Freymueller, 2009) demonstrated that afterslip was the dominant contribution to postseismic vertical motions in the Cook Inlet area. Separating the effects of afterslip and viscoelastic relaxation, especially in the near-field data, was a major challenge addressed by a series of papers over the years (e.g., Cohen & Freymueller, 2004).

Some early viscoelastic modeling studies suggested that the effects of viscoelastic relaxation from this event should extend across most of mainland Alaska. Piersanti et al. (1997) presented a global-scale viscoelastic relaxation model for this earthquake and compared the predictions of the model to the deformation observed in the 1980s by VLBI. While their model did not fit the data well, some general features of the model proved to be important. For example, Piersanti et al. (1997) suggested that the southward motion of the VLBI site in Nome, on the Seward Peninsula north of the Bering Sea and ~1000 km away from the earthquake rupture, was due to viscoelastic relaxation. Their model prediction for Nome was about a factor of 2–3 too large, but the later observations and modeling made it clear that the area of effect of the postseismic transient extended even farther (Huang et al., 2020; Suito & Freymueller, 2009).

The most recent model was presented by Huang et al. (2020). That model agreed quite well with the previous model of Suito and Freymueller (2009) in the near-field region, differing mainly in the treatment of afterslip. Suito and Freymueller (2009) estimated afterslip from the available cumulative uplift data from leveling, leveling/GPS combination, tide gauges, and repeat surveys of tidal benchmarks. As a result, their model presumed that there was no afterslip in areas where there was no data to constrain the model. Huang et al. (2020) used an approximation to derive stress-driven afterslip, where the total afterslip is controlled by the stress changes computed from the coseismic slip model. The two afterslip models are in good agreement where there was good data to constrain the Suito and Freymueller (2009) model, but the Huang et al. (2020) model shows significant afterslip extending to the east of Anchorage, where there was a data gap for Suito and Freymueller (2009).

These two models differ more in the far field (Figure 5.26). The Suito and Freymueller (2009) model used a model domain that extended to near the Arctic coast of Alaska, where a zero displacement condition was imposed. That model domain proved to be too small. The model domain used by Huang et al. (2020) extended horizontally for 3000 × 4000 km and extended about twice as far from the rupture as did the Suito and Freymueller (2009) model. Huang et al. (2020) found that ongoing velocities of 1–2 mm/year extended across almost all of continental Alaska (Figure 5.26). In the Seward Peninsula and the Bering Strait region, they showed that removing
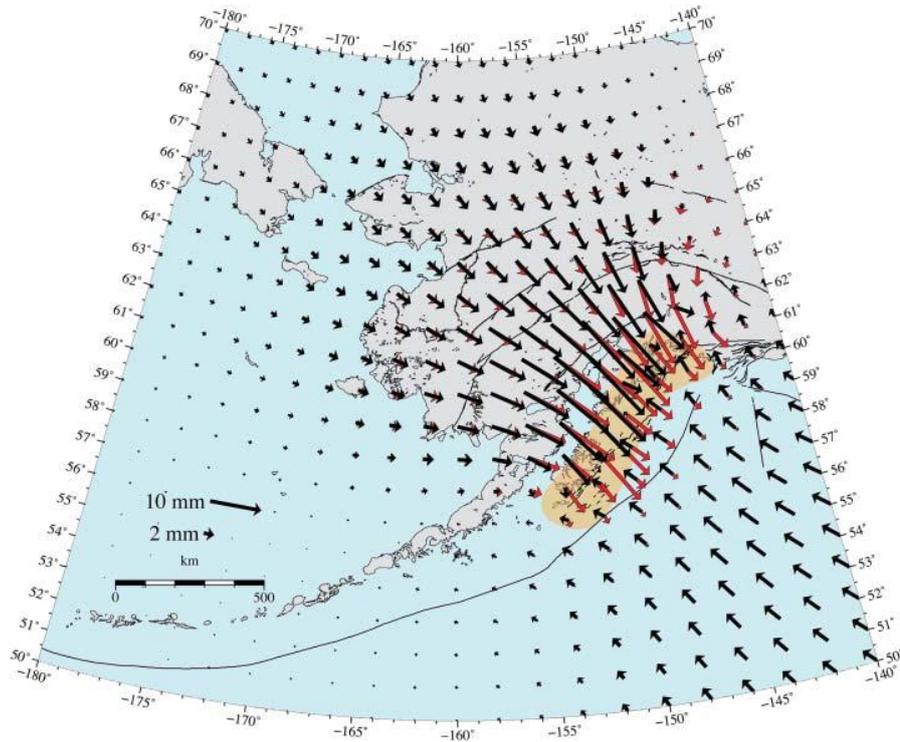
Figure 5.26 Predicted postseismic velocities due to the 1964 M9.2 Great Alaska earthquake, computed as the average for the interval 1995–2004. Red vectors show predictions from the model of Suito et al. (2009) while black vectors show predictions from the model of Huang et al. (2020). Shaded region shows approximate rupture area of the 1964 M9.2 Great Alaska earthquake (Sykes et al., 1980).

this model from the present-day velocities allowed a simple two-block model to be fit to the residual velocities that were consistent with the sense of motion inferred from seismic focal mechanisms and the tectonic model of Mackey et al. (2010).

2002 M7.9 Denali Fault Earthquake

The 2002 M7.9 Denali Fault Earthquake struck central Alaska on 3 November 2002 (Eberhart-Phillips et al., 2003; Hreinsdóttir et al., 2006). The immediate postseismic transient observed velocities were as large as 20–25 cm/year in the first months after the earthquake; despite a rapid decay with time, postseismic displacements continued at a rate of a few to several cm/year for many years after the event, especially for sites located 50–100 km away from the rupture (Figure 5.27). The displacements shown in Figure 5.27 were computed from a mixture of campaign and continuous GPS sites by first subtracting the observed or estimated pre-earthquake velocities from the observed postseismic time series, then fitting a combination of logarithmic and exponential relaxation terms to the corrected time series, and finally evaluating these functions at a set of specific times.

This sampling approach allows for the episodic campaign measurements to combined effectively with the continuous measurements. After the rapid decay of the deformation rate, during the first few years, the campaign measurements contribute nearly as much information as the continuous sites because the campaign measurements were made consistently and the processes decay slowly over time with time constants that can be constrained by the continuous data.

Harper (2017) analyzed the postseismic time series and estimated the optimal time constants for fitting the postseismic time series with a combination of a logarithmic and an exponential relaxation. The optimal time constant for the logarithmic component was 0.12 years, and 20 years for the exponential component. A longer exponential time constant is difficult to rule out given that the postseismic data time span was only ~13 years, but the 20-year relaxation time is the same as that estimated by Suito and Freymueller (2009) for the postseismic deformation following the 1964 earthquake. The presence of separate rapidly decaying and slowly decaying processes is clear in a comparison of panels (a) and (b) of Figure 5.27. In the first several years, at least some
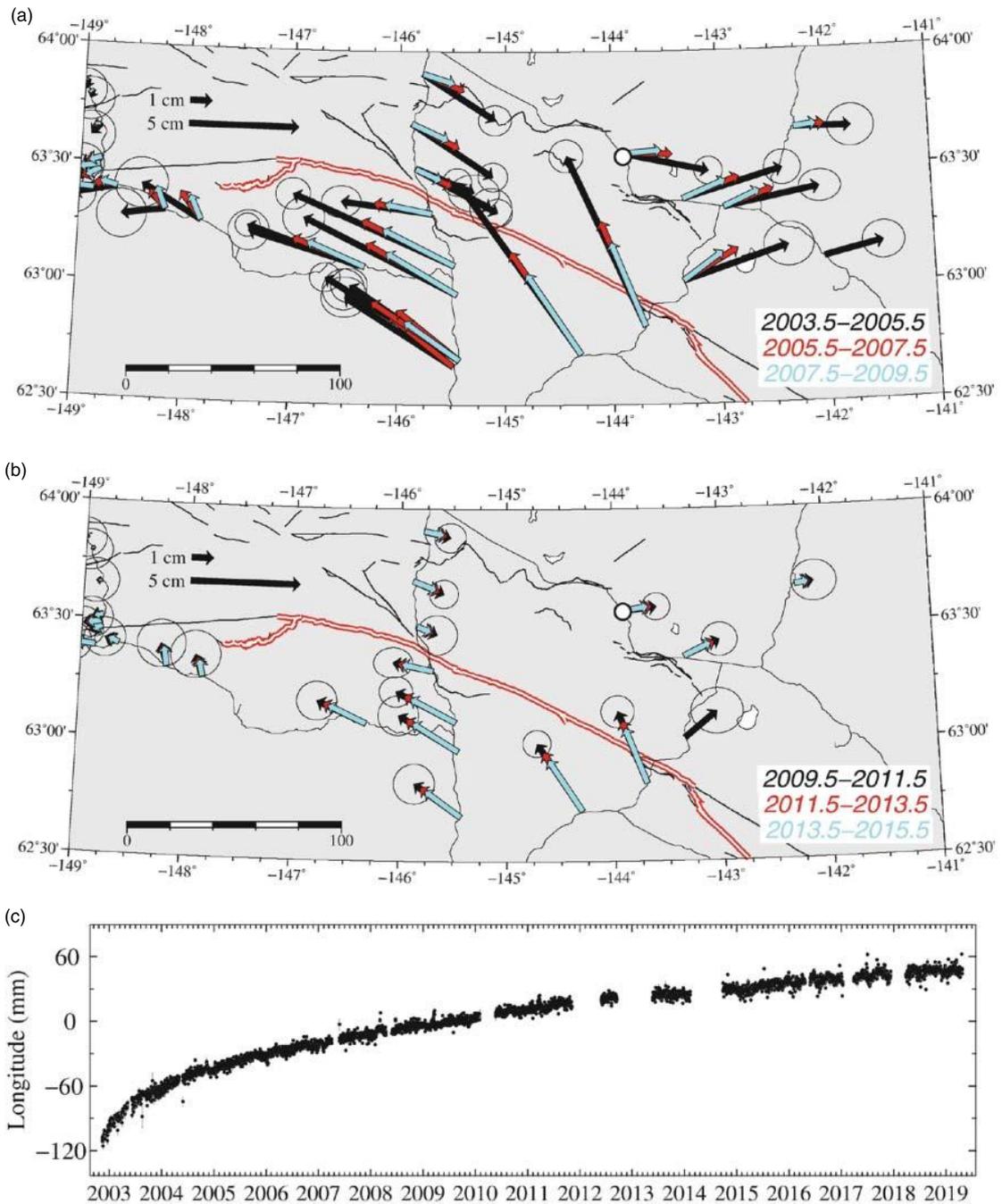
(a)

(b)

(c)

Figure 5.27 Postseismic displacements over time due to the 2002 M7.9 Denali Fault earthquake. Panels (a) and (b) show the transient displacements (relative to the pre-earthquake velocity model) over successive time intervals from 2003.5–2005.5 through 2013.5–2015. For later time periods, some sites would also require corrections for additional earthquakes (Section 5.5.2). Panel (c) shows the east component time series of the site JANL (white dot), located north of the rupture, which shows the long, slow time decay of the postseismic displacements (from Freymueller (2020)/Springer Nature).

of the sites' velocities significantly change orientation, which results when the rapidly decaying logarithmic relaxation process (likely correlated to the afterslip) decays to near-zero. In the later years, the magnitude of the transient decreases but the orientation of the vectors hardly changes, which indicates that the deformation is dominated by the slowly decaying process. The long relaxation time for the exponential relaxation indicates that the postseismic signal will be present across the region for many years to come, although it will be smaller in magnitude at sites that are more distal.

2013 M7.5 Craig and 2012 M7.8 Haida Gwaii Earthquakes

Postseismic deformation from the Haida Gwaii earthquake was first studied by Nykolaishen et al. (2015). They deployed six temporary continuous sites in the near-field of the event on Moresby Island about 2 weeks after the earthquake and presented the cumulative postseismic displacements from the first year after the earthquake from these sites and from two regional continuous sites. The cumulative postseismic displacements were as large as 6 cm. In the northern part of the rupture area, the coseismic and postseismic displacements had a similar orientation, being directed seaward, nearly normal to the strike of the Queen Charlotte fault and the offshore thrust. However, near the south end of the rupture, the postseismic displacements rotated ~90° to become largely parallel to the Queen Charlotte fault. This likely indicated postseismic creep on the Queen Charlotte fault, a conclusion also supported by the analysis of repeating earthquakes by Hayward and Bostock (2017). Tian et al. (2021) used the Nykolaishen et al. (2015) postseismic data along with data from continuous sites across SE Alaska and western British Columbia to estimate postseismic models for both the Haida Gwaii and Craig earthquakes. Their models combined stress-driven afterslip on the deeper part of the fault plane for each event and viscoelastic relaxation assuming a common viscosity model for both events. Sites located between the two events had some sensitivity to the postseismic signals of both events, but the signals were readily separable because they happened to cause displacements in nearly orthogonal directions. Because there was no truly near-field data for the Craig event and near-field data for Haida Gwaii only in the first year, they could not resolve spatial details of the afterslip distribution well. However, the afterslip decayed rapidly while the viscoelastic relaxation decayed much more slowly. The subcontinental mantle was modeled as a Burger's body with a Maxwell element viscosity of $(0.8-3) \times 10^{19}$ Pa·s and a Kelvin element viscosity 1 order of magnitude lower. The Burger's body model fit the time series better than a Maxwell viscosity model. The Maxwell viscosity estimated for the region

was quite similar to the estimates for SE Alaska from GIA models and similar to the estimate for the 1964 Alaska earthquake.

5.5.4. Slow Slip Events

The first observed SSE in Alaska occurred between 1998 and 2001 in Upper Cook Inlet on a partially coupled section of the subduction interface located downdip of the rupture area of the 1964 M9.2 earthquake (Freymueller et al., 2002; Ohta et al., 2006; Figure 5.28). Modeling of the event estimated that 120–165 mm/year of total slip occurred over the 3-year period, equivalent to 5–15 years of slip deficit depending on the area of the slip patch (Ohta et al., 2006). The cumulative seismic moment of 1.1×10^{20} N·m was equal to a moment magnitude of 7.2. Between 2005 and 2006, a smaller event lasting about 6 weeks occurred in roughly the same location as the 1998–2001 event (Ohta et al., 2007). Further analysis of this event and detection of possible other transient events in the region were greatly hampered by the spareness of the continuous GPS network at the time.

The expansion of the GPS networks in Alaska, including PBO/NOTA, significantly changed the situation (Figure 5.2). Another SSE occurred in approximately the same region as the 1998–2001 event between 2008 and 2013 and had a moment magnitude of ~7.6 (Fu & Freymueller, 2013; Fu et al., 2015). The increased density of GPS sites allowed a spatiotemporal evaluation of the evolution of the event. Slip rate accelerated over the first years of the event while slip migrated from the updip edge of the SSE patch to the deeper region before laterally moving east over the course of the event (Fu et al., 2015). Most the strain accumulated since the 1998–2001 event was released during the later event, suggesting that the region of the subduction interface below the 1964 rupture may have accumulated no net slip deficit during the time period of geodetic observations and may not slip in large earthquakes (Fu & Freymueller, 2013; Fu et al., 2015). Rousset et al. (2019), based on decomposition of GPS time series, suggested that the 2008–2013 event could, instead of a single long transient event, be a series of shorter transient slip events associated with tremor. They particularly highlight a pulse spanning September 2010, when ~9% of the total 5-year event moment was released.

Further to the southwest from the repeat SSE described above, Wei et al. (2012) detected and described an at-the-time ongoing SSE in lower Cook Inlet that began in early 2010 (Figure 5.28). Modeling of the GPS data produced a maximum slip of 17 mm beneath Cook Inlet that is broadly distributed between 35 and 80 km depths generating a cumulative moment equivalent to M_w 6.9 between early 2010 and November of 2011. Fu et al. (2015) and Li et al. (2016) also resolved this event,
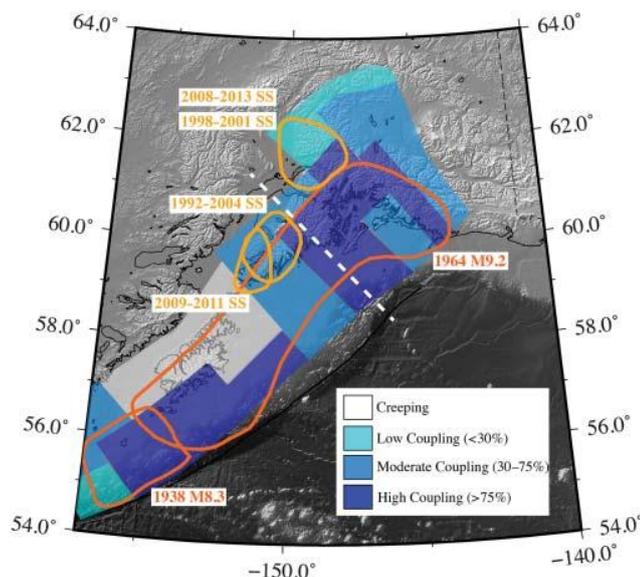
Figure 5.28 Coupling, past earthquakes, and slow slip events along the eastern Alaska subduction zone. Coupling estimates are the same as Figure 5.10. Dark orange outlines show rupture areas of past earthquakes. Light orange outlines show areas of slow slip events. White dashed line shows the western edge of the subducting Yakutat block Kim et al., (2014)/John Wiley & Sons.

determining that the event began in late 2009 and ended between August and November 2011 for a total duration of less than 2 years. This event had a cumulative moment magnitude of 7.2 (Li et al., 2016). Incorporating campaign GPS data, Li et al. (2016) extended the data time series in lower Cook Inlet back to the 1990s. They found evidence of an SSE that was underway when observations began in 1995 and ended in late 2004. This 9+ year event had a minimum cumulative moment magnitude of 7.8 and may have accommodated the entire slip deficit accumulated in the SSE region since the M9.2 1964 earthquake. Through a re-evaluation of the data, Li et al. (2018) suggested that this long event may have been two separate SSEs with a pause during the 2001–2002 time period, but the interpretation is complicated by the offset and postseismic deformation from the 2002 M7.9 Denali earthquake.

As Figure 5.28 shows, the SSEs in Alaska observed to date cluster on either side of the eastern Kenai Peninsula, which is where the shallowly subducting slab portion of the Yakutat block, an oceanic plateau, transitions to the more typical oceanic crust of the Pacific Plate (e.g., Kim et al., 2014). SSEs in upper Cook Inlet occur along the Yakutat interface while SSEs in lower Cook Inlet occur along the Pacific interface. Using numerical modeling, Li et al. (2018) investigated whether this transition could change the effective normal stress on the subduction interface and influence the separation between the SSE patches. They suggested that the normal stress could be affected by either a reduction in pore pressure in Upper Cook Inlet due to less fluid release or the buoyancy of the thickened Yakutat block, with the latter mechanism causing increased normal stress. Although they could not rule out pore pressure changes, buoyancy-related normal stress increase was their preferred explanation.

The relationship between SSEs, slip budget, and large earthquakes is not yet fully understood due to the short time span of dense geodetic measurements in Alaska. SSEs do appear to accommodate all or a significant portion of the accumulated slip deficit in some regions downdip of the M9.2 1964 earthquake rupture (Fu & Freymueller, 2013; Fu et al., 2015; Li et al., 2016). Segou and Parsons (2020) suggested that a combination of postseismic deformation after the 1964 earthquake and the SSEs may have promoted the occurrence of the M7.1 2018 Anchorage earthquake, which was an intraplate event. Gaining a more thorough understanding of the role SSEs play in accommodating relative plate motion and advancing or reducing the likelihood of large, damaging earthquakes will require longer observation time periods for the geophysical data sets. Offshore deformation measurements will also be critical to evaluate whether transient slip occurs in the shallower portions of the interface. Initial deployments of seafloor geodetic instruments near the trench have been shown capable of yielding useful data (e.g., Brooks et al., 2023; Fredrickson et al., 2023), but limited span and spatial sparsity limits resolution.

5.6. GEODYNAMIC MODELS

Both Alaska-wide and regional geodynamic models using geodetic data as constraints or comparison tools have been developed over the past 15 years. Focusing on the area immediately surrounding and south of the Denali Fault, Haynie and Jadamec (2017) developed three-dimensional finite-element models that incorporated detailed slab geometries (including a flat slab), variable upper-plate thickness, and fault shear zones to investigate driving forces. They found that a combination of the shallow subduction geometry, coupling between the upper plate and slab, and a weak (low-viscosity) Denali shear zone could produce surface velocities south of the Denali Fault that are directed northwestward with a slight counterclockwise rotation similar to what is observed with the GPS data. Ali and Freed (2010) used two- and three-dimensional finite-element models with a flat slab geometry, an assumption that all of the slab moves with the Pacific Plate, and locked Denali and Fairweather–Queen Charlotte faults to compare interseismic GPS velocities that had not been corrected for any postseismic signals. This model, with a subduction zone interface locked to a depth of 30 km, could explain GPS velocities in areas not strongly impacted by postseismic deformation, such as southeast Alaska, but could not explain GPS velocities south or north of the Denali Fault. These areas required a combination of the effects of Pacific–North America convergence, viscoelastic deformation due to the M9.2 1964 Great Alaska earthquake, and afterslip along the subduction interface in the region of the 1964 rupture.

Using a surface deformation field constrained by GPS, geologic, and seismicity data along with lithospheric scale geodynamic models covering the entire region from the Bering Sea to the Canadian Cordillera, Finzel et al. (2015) explored how various driving forces contributed to the observed deformation. While plate boundary forces and gravitational potential energy would explain observations south of the Denali Fault, they could not explain the southeast to southwest GPS velocities north of the fault in northern and western Alaska (Figure 5.5). Including mantle tractions in the model helped to produce surface deformation that more closely matched the GPS data. Expanding on this model, McConeghy et al. (2022) used estimates of long-term block motion from Elliott and Freymueller (2020a) as constraints to avoid issues of elastic or other transient tectonic signals in the GPS data. The updated model showed that plate boundary forces, especially the collision and flat slab subduction of the Yakutat block, are the prime drivers of deformation in southeast and southcentral Alaska. North of the Denali Fault, mantle tractions could reproduce the south-southwesterly GPS velocities observed in western Alaska and the southeast-directed velocities in arctic Alaska and the Canadian Cordillera. Uplift in the Mackenize Mountains may be due to a combination of stress transmitted inboard from the Yakutat collisional front and the effects of mantle tractions. The location of the inflection point between plate boundary dominated motion and mantle influenced motion is just north of the Denali Fault and may be controlled by the leading edge of the Yakutat flat slab. Taken together, these geodynamic models show that deformation in Alaska and western Canada does not have a simple explanation but requires a combination of driving forces.

5.7. IMPLICATIONS FOR ALASKA TECTONICS

The significant expansion of GPS data in Alaska and western Canada over the past 15 years has provided a far more detailed picture of active deformation than previously available. One major conclusion that can be drawn is that no part of Alaska or western Canada moves with stable North America. While velocities are small in western Alaska and the Arctic, they show coherent patterns of motion. While most relative plate motion is accommodated along major plate boundary systems such as the Fairweather–Queen Charlotte transform system and the Alaska–Aleutian subduction zone, motion is also accommodated both on discrete structures and across deformation zones in interior Alaska, northern Alaska, and northwest Canada 1,000 km away from the main plate boundary. Some regions appear to behave in a way consistent with rigid block rotation while others, especially in high strain areas, display patterns more consistent with continuum deformation.

Strain from the Yakutat collision is transferred inboard in different ways. It may be transferred through block rotation and distributed deformation into the Northern Cordillera of Canada, north via strike-slip fault systems into interior Alaska, and west through the thrust belt of the St. Elias orogen. Relative motion may be partitioned onto multiple faults and fault systems as evidenced by the 2017 Haines/Duke River earthquake doublet. The influence of the Yakutat block may continue westward as the shallowly subducting Yakutat slab appears to drive the counterclockwise rotation of southcentral Alaska and extrusion of southwestern Alaska toward the Bering Sea region.

Upper-plate motion varies greatly throughout the region, from tight rotations around the Yakutat collisional corner to northwestward motion across the Wrangell Mountains to arc-parallel motion along the Alaska Peninsula to southeastward motion in Arctic Alaska. Taking the varying motion into account is critical for accurate evaluation of seismic hazard and slip

rates along faults. This is especially true along the sub-duction zone, where the combination of Yakutat slab, Pacific Plate, and multiple upper-plate blocks may yield relative motion and slip rates quite different from simple assumptions of Pacific–North America convergence rates.

The northeastern Pacific Plate within the Gulf of Alaska appears to be undergoing internal deformation and may be in the process of breaking up into smaller blocks or deformation zones. Both the Gulf of Alaska shear zone earthquakes and the 2018 M7.9 Offshore Kodiak earthquake may have been triggered by stresses transferred outboard from the convergent margin. A more complete understanding of the northeastern Pacific deformation will require seafloor geodetic instrumentation such as additional acoustic GPS (e.g., Brooks et al., 2023) and repeat bathymetric mapping.

Along the subduction zone, geodetically determined coupling estimates indicate high degrees of coupling in regions that experienced large coseismic slip during past earthquakes, suggesting the presence of persistent asperities in at least some areas. Some lateral coupling boundaries, especially those that are linked to structural differences between interface segments, may be persistent and serve as nucleation points or barriers to earthquake rupture. Given the distribution of GPS sites, there can be multiple coupling distributions that fit the data well. Assessing the range of what is or is not allowed given a data set is important for seismic hazard evaluation, especially in the offshore region of the subduction interface. Existing acoustic GPS sites and new sites that will be installed as part of an NSF community experiment will greatly improve data coverage, but separating signals will take careful consideration and long time series will be needed to fully evaluate the interseismic signal. Slow slip events may accommodate a substantial portion of the slip budget in the partially coupled regions downdip of the 1964 rupture in the Cook Inlet region. Stress loading from earthquakes, coupling contrasts, postseismic deformation, and transient SSEs may play an important role in triggering both interplate and intraplate earthquakes.

5.8. CONCLUSIONS

The expanded networks of both campaign and continuous GPS sites in Alaska and western Canada established over the past 15 years have greatly enhanced spatial and temporal resolution of active surface deformation. This new synoptic view shows that the entire region moves in a way distinct from stable North America. While the majority of the deformation can be attributed to tectonic deformation, the expanded data set shows that nontectonic sources including GIA, seasonal snow loading, volcanic activity, and permafrost change can contribute

significantly to the observed deformation signal and need to be evaluated when tectonic signals are interpreted.

Long-term motion of the upper plate varies greatly, with translation in southeast Alaska and the adjacent part of British Columbia, collision and indentation in the St. Elias and the Yukon, counterclockwise rotation in southcentral Alaska over the subducting Yakutat flat slab and Pacific Plate, extrusion in western Alaska toward the Bering Sea, and southerly to southeasterly motion in northern Alaska that may be related to mantle flow. The subduction interface also shows great variability with geodetic coupling estimates showing significant changes both along strike and downdip, although there is uncertainty due to sparse data in the offshore region. Major earthquakes appear to correlate to areas of moderate-to-high coupling, suggesting persistent asperities. While the segment that generated the 1946 M8.6 tsunamigenic earthquake is usually assumed to be creeping based on the GPS data located along the Alaska Peninsula, a small band of moderate coupling can exist near the trench without misfitting the data.

The geodetic networks captured deformation from earthquakes across the region from Haida Gwaii in British Columbia to the subduction interface along the Alaska Peninsula to the far western Aleutians, shedding new light on tectonic processes and slip behavior. The earthquakes also caused displacements and time-varying signals in geodetic time series across wide swaths of the region, complicating interpretation. The dense networks in Cook Inlet and along the Alaska Peninsula recorded the complex deformation pattern caused by slip along multiple faults within the Pacific Plate during the 2018 M7.9 Offshore Kodiak earthquake, an event that may be an indication of the formation of a new plate boundary. High-rate GPS data from sites around the 2021 M8.2 Chignik and 2020 M7.8 Simeonof ruptures helped determine the spatial and temporal slip evolution during those events. Postseismic deformation from the 1964 M9.2 Great Alaska and 2002 M7.9 Denali Fault earthquakes is still quite evident, with observed rates of motion south of the Denali Fault considerably higher than they were prior to the earthquake. Several SSEs have occurred, some lasting years, downdip of the rupture region of the 1964 earthquake within partially coupled regions of the subduction interface. Spatial clustering of the events may be related to the transition from the Yakutat flat slab to more normal Pacific oceanic crust. Earthquakes may be promoted by stress loading not only from previous earthquakes but also from transient deformation and interseismic coupling, suggesting that all of these processes need to be assessed to fully evaluate seismic hazard.

Looking toward the future, more expansions to the land-based GPS networks are planned. These new sites,

along with longer time series at existing sites, will provide more detailed observations of tectonic deformation and allow a more careful evaluation of tectonic and non-tectonic deformation. The first seafloor geodetic data captured the effects of multiple earthquakes along the subduction zone, and new seafloor geodetic stations will be installed in the coming years as well, providing greatly improved constraints in the near-trench region of the subduction zone. Together with improved processing and modeling techniques, the ever-increasing geodetic data set will provide an even more complete view of tectonic processes in the north Pacific.

ACKNOWLEDGMENTS

AVAILABILITY STATEMENT

Much of the data discussed here are from published works, and data access and citations are available through those publications. The coseismic offsets presented here are derived from raw data archived through the GAGE Facility, operated by the EarthScope Consortium, and are available at https://www.unavco.org/data/gps-gnss/gps-gnss.html.DOIs, and citation information for the data used in the coseismic offsets are listed after the main references. Coseismic displacement files are available at https://doi.org/10.5281/zenodo.10015783.

REFERENCES

Ali, S. T., & Freed, A. M. (2010). Contemporary deformation and stressing rates in Southern Alaska. *Geophysical Journal International*, *183*, 557–571. http://dx.doi.org/10.1111/j.1365-246X.2010.04784.x

Altamimi, Z., Collilieux, X., Legrand, J., Garayt, B., & Boucher, C. (2007). ITRF2005: A new release of the international terrestrial reference frame based on time series of station positions and earth orientation parameters. *Journal of Geophysical Research*, *112*, B09401. http://dx.doi.org/10.1029/2007JB004949

Altamimi, Z., Rebischung, P., Métivier, L., & Collilieux, X. (2016). ITRF2014: A new release of the international terrestrial reference frame modeling nonlinear station motions. *Journal of Geophysical Research*, *121*, 6109–6131.

Argus, D. F., Gordon, R. G., Heflin, M. B., Ma, C., Eanes, R. J., Willis, P., et al. (2010). The angular velocity of the plates and the velocity of Earth's centre from space geodesy. *Geophysical Journal International*, *180*, 913–960. http://dx.doi.org/10.1111/j.1365-246X.2009.04463.x

Argus, D. F., Peltier, W. R., Drummond, R., & Moore, A. W. (2014). The Antarctica component of postglacial rebound model ICE-6G_C (VM5a) based on GPS positioning, exposure age dating of ice thicknesses, and relative sea level histories. *Geophysical Journal International*, *198*, 537–563. http://dx.doi.org/10.1093/gji/ggu140

Avé Lallemant, H. G., & Oldow, J. S. (2000). Active displacement partitioning and arc-parallel extension of the Aleutian volcanic arc based on Global Positioning System geodesy and kinematic analysis. *Geology*, *28*, 739–742.

Bai, Y., Liu, C., Lay, T., Cheung, K. F., & Yamazaki, Y. (2023, 2015). Fast and slow intraplate ruptures during the October 2020 magnitude 7.6 Shumagin earthquake. *Nature*, *14*. https://doi.org/10.1038/s41467-023-37731-2

Bartlow, N., Wallace, L. M., Elliott, J., & Schwartz, S. (2021). Slipping and locking in Earth's earthquake factories. *Eos*, *102*. http://dx.doi.org/10.1029/2021EO155885

Bécel, A., Shillington, D. J., Delescluse, M., Nedimović, M. R., Abers, G. A., Saffer, D. M., et al. (2017). Tsunamigenic structures in a creeping section of the Alaska subduction zone. *Nature Geoscience*, *10*(8), 609–613.

Bemis, S. P., Weldon, R. J., & Carver, G. A. (2015). Slip partitioning along a continuously curved fault: Quaternary geologic controls on Denali fault system slip partitioning, growth of the Alaska Range, and the tectonics of south-central Alaska. *Lithosphere*, *7*(3), 235–224. http://dx.doi.org/10.1130/L352.1

Benowitz, J. A., Layer, P. W., Armstrong, P., Perry, S. E., Haeussler, P. J., Fitzgerald, P. G., & VanLaningham, S. (2011). Spatial variations in focused exhumation along a continental scale strike-slip fault: The Denali fault of the eastern Alaska Range. *Geosphere*, *7*(2), 455–467. http://dx.doi.org/10.1130/GES00589.1

Bertiger, W., Desai, S. D., Haines, B., Harvey, N., Moore, A. W., Owen, S., & Weiss, J. P. (2010). Single receiver phase ambiguity resolution with GPS data. *Journal of Geodesy*, *84*, 327–337. http://dx.doi.org/10.1007/s00190-010-0371-9

Böhm, J., Heinkelmann, R., & Schuh, H. (2007). Short Note: A global model of pressure and temperature for geodetic applications. *Journal of Geodesy*, *81*, 679–683. http://dx.doi.org/10.1007/s00190

Böhm, J., Werl, B., & Schuh, H. (2006). Troposphere mapping functions for GPS and very long baseline interferometry from

European Centre for Medium-Range Weather Forecasts operational analysis data. *Journal of Geophysical Research, 111.* http://dx.doi.org/10.1029/2005JB003629

Briggs, R. W., Engelhart, S. E., Nelson, A. R., Dura, T., Kemp, A. C., Haeussler, P. J., et al. (2014). Uplift and subsidence reveal a nonpersistent megathrust rupture boundary (Sitkinak Island, Alaska). *Geophysical Research Letters, 41,* 2289–2296.

Brooks, B. A., Goldberg, D., DeSanto, J., Ericksen, T. L., Webb, S. C., Nooner, S. L., et al. (2023). Rapid megathrust up-dip afterslip from the 2021 M8.2 Chignik, Alaska earthquake revealed by seafloor geodesy. *Science Advances, 9,* eadf9299. http://dx.doi.org/10.1126/sciadv.adf9299

Brothers, D. S., Elliott, J., Conrad, J. E., Haeussler, P. J., & Kluesner, J. A. (2018). Strain partitioning in Southeastern Alaska: Is the Chatham strain fault active? *Earth and Planetary Science Letters, 481,* 362–371. https://doi.org/10.1130/10.1016/j.epsl.2017.10.017

Brothers, D. S., Miller, N. C., Barrie, J. V., Haeussler, P. J., Greene, H. G., Andrews, B. A., et al. (2020). Plate boundary localization, slip-rates and rupture segmentation of the Queen Charlotte Fault based on submarine tectonic geomorphology. *Earth and Planetary Science Letters, 530.* http://dx.doi.org/10.1016/j.epsl.2019.115882

Brown, L. D., Reilinger, R. E., Holdahl, S. R., & Balazs, E. I. (1977). Postseismic crustal uplift near Anchorage, Alaska. *Journal of Geophysical Research, 92,* 3369–3377.

Bürgmann, R., & Dresen, G. (2008). Rheology of the lower crust and upper mantle: Evidence from rock mechanics, geodesy, and field observations. *Annual Review of Earth and Planetary Sciences, 36,* 531–567. http://dx.doi.org/10.1146/annurev.earth.36.031207.124326

Bürgmann, R., & Thatcher, W. (2013). Space geodesy: A revolution in crustal deformation measurements of tectonic processes. In M. E. Bickford (Ed.), *The web of geological sciences: Advances, impacts, and interactions* (pp. 397–430). Geological Society of America Special Paper 500. https://doi.org/10.1130/2013.2500(12)

Carver, G., Sauber, J., Lettis, W., Witter, R., & Whitney, B. (2008). Active faults on Northeastern Kodiak Island, Alaska. In J. T. Freymueller, P. J. Haeussler, R. L. Wesson, & G. Ekström (Eds.), *Active Tectonics and Seismic Potential of Alaska.* https://doi.org/10.1029/179GM09

Cassidy, F., Rogers, G. C., & Hyndman, R. D. (2014). An overview of the 28 October 2012 Mw 7.7 earthquake in Haida Gwaii, Canada: A Tsunamigenic thrust event along a predominantly strike-slip margin. *Pure and Applied Geophysics, 171.* http://dx.doi.org/10.1007/s00024-014-0775-1

Chadwell, C. D., & Spiess, F. N. (2008). Plate motion at the ridge-transform boundary of the south Cleft segment of the Juan de Fuca Ridge from GPS-Acoustic data. *Journal of Geophysical Research, 113*(B4), B04415. http://dx.doi.org/10.1029/2007JB004936

Chapman, J. B., Elliott, J., Doser, D. I., & Pavlis, T. L. (2014). Slip on the Suckling Hills splay fault during the 1964 Alaska earthquake. *Tectonophysics, 637,* 191–197. https://doi.org/10.1016/j.tecto.2014.10.007

Choy, G. L., & McGarr, A. (2002). Strike-slip earthquakes in the oceanic lithosphere: Observations of exceptionally high apparent stress. *Geophysical Journal International, 150,* 506–523. https://doi.org/10.1046/j.1365-246X.2002.01720.x

Christeson, G. L., Gulick, S. P. S., van Avendonk, H. J. A., Worthington, L. L., Reece, R. S., & Pavlis, T. L. (2010). The Yakutat terrane: Dramatic change in crustal thickness across the Transition fault, Alaska. *Geology, 38*(10), 895–898.

Cohen, S. C., & Freymueller, J. T. (2004). Crustal deformation in southcentral Alaska: The 1964 Prince William sound earthquake subduction zone. *Advances in Geophysics, 47,* 1–63.

Coudurier-Curveur, A., Karakaş, Ç., Singh, S., Tapponnier, P., Carton, H., & Hananto, N. (2020). Is there a nascent plate boundary in the northern Indian Ocean? *Geophysical Research Letters, 47,* e2020GL087362. http://dx.doi.org/10.1029/2020GL087362

Cross, R. S., & Freymueller, J. T. (2008). Evidence for and implications of a Bering plate based on geodetic measurements from the Aleutians and western Alaska. *Journal of Geophysical Research, 113,* B07405. http://dx.doi.org/10.1029/2007JB005136

Crowell, B. W., & Melgar, D. (2020). Slipping the Shumagin Gap: A kinematic coseismic and early afterslip model of the Mw 7.8 Simeonof Island, Alaska, earthquake. *Geophysical Research Letters, 47,* e2020GL090308. http://dx.doi.org/10.1029/2020GL090308

DeGrandpre, K. G., & Freymueller, J. T. (2019). Vertical velocities, glacial isostatic adjustment, and earth structure of northern and western Alaska based on repeat GPS measurements. *Journal of Geophysical Research: Solid Earth, 124,* 9148–9163. http://dx.doi.org/10.1029/2018JB017163

DeSanto, J. B., Webb, S. C., Nooner, S. L., Schmidt, D. A., Crowell, B. W., Brooks, B. A., et al. (2023). Limited shallow slip for the 2020 Simeonof earthquake, Alaska, constrained by GNSS-Acoustic. *Geophysical Research Letters, 50,* e2023GL105045. http://dx.doi.org/10.1029/2023GL105045

Ding, K., Freymueller, J. T., He, P., Wang, Q., & Xu, C. (2019). Glacial isostatic adjustment, intraplate strain, and relative sea level changes in the eastern United States. *Journal of Geophysical Research: Solid Earth, 124,* 6056–6071. https://doi.org/10.1029/2018JB017060

Ding, K., Freymueller, J. T., Wang, Q., & Zou, R. (2015). Coseismic and early postseismic deformation of the 5 January 2013 Mw 7.5 Craig earthquake from static and kinematic GPS solutions. *Bulletin of the Seismological Society of America, 105*(2B), 1153–1164. http://dx.doi.org/10.1785/0120140172

Drooff, C., & Freymueller, J. T. (2021). New constraints on slip deficit on the Aleutian megathrust and inflation at Mt. Veniaminof, Alaska from repeat GPS measurements. *Geophysical Research Letters, 48,* e2020GL091787. http://dx.doi.org/10.1029/2020GL091787

Dziewonski, A. M., T.-A. Chou, and J. H. Woodhouse (1981), Determination of earthquake source parameters from waveform data for studies of global and regional seismicity, *J. Geophys. Res., 86*(B4), 2825–2852, doi:10.1029/JB086iB04p02825.

Eberhart-Phillips, D., Haeussler, P. J., Freymueller, J. T., Frankel, A. D., Rubin, C. M., Craw, P., et al. (2003). The 2002 Denali fault earthquake, Alaska: A large magnitude, slip-partitioned event. *Science, 300,* 113–119.

Eberhart-Phillips, D., Christensen, D. H., Brocher, T. M., Hansen, R., Ruppert, N. A., Haussler, P. J., & Abers, G. A.

(2006). Imaging the transition from Aleutian subduction to Yakutat collision in central Alaska, with local earthquakes and active source data. *Journal of Geophysical Research*, *111*, B11303. https://doi.org/10.1029/2005JB004240

Ekström, G., Nettles, M., and Dziewonski, A.M. (2012), The global CMT project 2004-2010: Centroid-moment tensors for 13,017 earthquakes, Physics of the Earth and Planetary Interiors, 200–201, 1–9, https://doi.org/10.1016/j.pepi.2012.04.002.

Elliott, J., & Freymueller, J. T. (2020a). A block model of present-day kinematics of Alaska and western Canada. *Journal of Geophysical Research: Solid Earth*, *125*, e2019JB018378. https://doi.org/10.1130/10.1029/2019JB018378

Elliott, J., and Freymueller, J. T. (2020b), *Kinematics of the Fairweather–Queen Charlotte transform system and deformation of the northeast Pacific plate*, T050–09, presented at 2020 AGU Fall Meeting, 1–17 December.

Elliott, J., Freymueller, J. T., & Larsen, C. F. (2013). Active tectonics of the St. Elias orogen, Alaska, observed with GPS measurements. *Journal of Geophysical Research – Solid Earth*, *118*, 5625–5642. http://dx.doi.org/10.1002/jgrb.50341

Elliott, J. L., Grapenthin, R., Parameswaran, R., Xiao, Z., Freymueller, J. T., & Fusso, L. (2022). Cascading rupture of a megathrust. *Science Advances*, *8*(18), eabm4131. http://dx.doi.org/10.1126/sciadv.abm4131

Elliott, J. L., Larsen, C. F., Freymueller, J. T., & Motyka, R. J. (2010). Tectonic block motion and glacial isostatic adjustment in Southeast Alaska and adjacent Canada constrained by GPS measurements. *Journal of Geophysical Research*, *115*, B09407. http://dx.doi.org/10.1029/2009JB007139

Feng, W., Samsonov, S., Liang, C., Li, J., Charbonneau, F., Yu, C., & Li, Z. (2019). Source parameters of the 2017 Mw 6.2 Yukon earthquake doublet inferred from coseismic GPS and ALOS-2 deformation measurements. *Geophysical Journal International*, *216*(3), 1517–1528. http://dx.doi.org/10.1093/gji/ggy497

Finzel, E. S., Flesch, L. M., Ridgway, K. D., Holt, W. E., & Ghosh, A. (2015). Surface motions and intraplate continental deformation in Alaska driven by mantle flow. *Geophysical Research Letters*, *42*, 4350–4358. http://dx.doi.org/10.1002/2015GL063987

Fletcher, H. (2002), Crustal deformation in Alaska measured using Global Positioning System, (Ph.D. dissertation). 135 pp., Univ. of Alaska Fairbanks, Fairbanks.

Fredrickson, E. K., Gomberg, J. S., Wilcock, W. S. D., Hautala, S. L., Hermann, A. J., & Johnson, H. P. (2023). Slow slip detectability in seafloor pressure records offshore Alaska. *Journal of Geophysical Research: Solid. Earth*, *128*, e2022JB024767. https://doi.org/10.1029/2022JB024767

Freymueller, J. T. (2017). Geodynamics (Chapter 37). In O. Montenbruck & P. Teunissen (Eds.), *GNSS handbook* (pp. 1063–1106). Springer International.

Freymueller, J. T. (2020). GPS, tectonic geodesy. In H. Gupta (Ed.), *Encyclopedia of solid earth geophysics*, Encyclopedia of Earth Sciences Series. Cham: Springer. http://dx.doi.org/10.1007/978-3-030-10475-7_77-1

Freymueller, J. T., Hreinsdottir, S., Zweck, C., & Haeussler, P. J. (2002). The 1998 – 2002 deep megathrust slip event, Alaska, Eos Trans. *AGU*, *83*(47), Fall Meet. Suppl., Abstract G61A – 0972

Freymueller, J. T., Suleimani, E. N., & Nicolsky, D. J. (2021). Constraints on the slip distribution of the 1938 M_w 8.3 Alaska peninsula earthquake from tsunami modeling. *Geophysical Research Letters*, *48*(9), 2021GL092812.

Freymueller, J. T., Woodard, H., Cohen, S., Cross, R., Elliott, J., Larsen, C., et al. (2008). Active deformation processes in Alaska, based on 15 years of GPS measurements. In J. T. Freymueller, P. J. Haeussler, R. Wesson, & G. Ekstrom (Eds.), *Active tectonics and seismic potential of Alaska*, AGU Geophysical Monograph, 179 (pp. 1–42). Washington, D.C.: AGU.

Fu, Y., & Freymueller, J. T. (2012). Seasonal and long-term vertical deformation in the Nepal Himalaya constrained by GPS and GRACE measurements. *Journal of Geophysical Research*, *117*, B03407. http://dx.doi.org/10.1029/2011JB008925

Fu, Y., & Freymueller, J. T. (2013). Repeated large slow slip events at the southcentral Alaska Subduction zone. *Earth and Planet Science Letters*, *375*, 303–311. https://doi.org/10.1016/j.epsl.2013.05.049

Fu, Y., Freymueller, J. T., & van Dam, T. (2012). The effect of using inconsistent ocean tidal loading models on GPS coordinate solutions. *Journal of Geodesy*, *86*(6), 409–421. http://dx.doi.org/10.1007/s00190-011-0528-1

Fu, Y., Liu, Z., & Freymueller, J. T. (2015). Spatiotemporal variations of the slow slip event between 2008 and 2013 in the southcentral Alaska subduction zone. *Geochemistry Geophysics Geosystems*, *16*, 2450–2461. https://doi.org/10.1002/2015GC005904

Gaudreau, É., Nissen, E. K., Bergman, E. A., Benz, H. M., Tan, F., & Karasözen, E. (2019). The August 2018 Kaktovik earthquakes: Active tectonics in northeastern alaska revealed with InSAR and seismology. *Geophysical Research Letters*, *46*, 14,412–14,420. http://dx.doi.org/10.1029/2019GL085651

Grapenthin, R., Cheng, Y., Angarita, M., Tan, D., Meyer, F. J., Fee, D., & Wech, A. (2022). Return from dormancy: Rapid inflation and seismic unrest driven by transcrustal magma transfer at Mt. Edgecumbe (L'úx Shaa) Volcano, Alaska. *Geophysical Research Letters*, *49*, e2022GL099464. http://dx.doi.org/10.1029/2022GL099464

Grapenthin, R., Freymueller, J. T., & Kaufman, A. M. (2013). Geodetic observations during the 2009 eruption of Reboubt Volcano, Alaska. *Journal of Volcanology and Geothermal Research*, *259*, 115–132. http://dx.doi.org/10.1016/j.volgeores.2012.04.021

Grapenthin, R., West, M., & Freymueller, J. T. (2017). The utility of GNSS for earthquake early warning in regions with sparse seismic networks. *Bull. Seism. Soc. Am.*, *107*. http://dx.doi.org/10.1785/0120160317

Grapenthin, R., West, M., Tape, C., Gardine, M., & Freymueller, J. T. (2018). Single-frequency instantaneous GNSS velocities resolve dynamic ground motion of the 2016 Mw 7.1 Iniskin, Alaska, earthquake. *Seismological Research Letters*, *89*(3), 1040–1048. http://dx.doi.org/10.1785/0220170235

Guo, Y., Miyakoshi, K., & Tsurugi, M. (2020). Simultaneous rupture on conjugate faults during the 2018 Anchorage, Alaska, intraslab earthquake (MW 7.1) inverted from strong-motion waveforms. *Earth, Planets and Space*, *72*, 176. http://dx.doi.org/10.1186/s40623-020-01315-x

Haeussler, P. J., Matmon, A., Schwartz, D. P., & Seitz, G. G. (2017). Neotectonics of interior Alaska and the late Quarternary slip rate along the Denali fault system. *Geosphere*, *13*(5), 1445–1463. http://dx.doi.org/10.1130/GES01447.1

Harper, H. (2017). Modeling the coseismic and postseismic deformation of the 2002 Mw7.9 Denali, AK earthquake, (M. S. Thesis). University of Alaska Fairbanks, 80 pp.

Hayes, G. P., Wald, D. J., & Johnson, R. L. (2012). Slab1.0: A three-dimensional model of global subduction zone geometries. *Journal of Geophysical Research*, *117*, B01302. https://doi.org/10.1130/10.1029/2011JB008524

Haynie, K. L., & Jadamec, M. A. (2017). Tectonic drivers of the Wrangell block: Insights on fore-arc sliver processes from 3-D geodynamic models of Alaska. *Tectonics*, *36*, 1180–1206. http://dx.doi.org/10.1002/2016TC004410

Hayward, T. W., & Bostock, M. G. (2017). Slip behavior of the Queen Charlotte plate boundary before and after the 2012, MW 7.8 Haida Gwaii earthquake: Evidence from repeating earthquakes. *Journal of Geophysical Research: Solid Earth*, *122*, 8990–9011. http://dx.doi.org/10.1002/2017JB014248

He, X., Ni, S., Zhang, P., & Freymueller, J. (2018). The 1 May 2017 British Columbia-Alaska earthquake doublet and implication for complexity near the southern end of Denali fault system. *Geophysical Research Letters*, *45*, 5937–5947. http://dx.doi.org/10.1029/2018GL078014

Herman, M. W., & Furlong, K. P. (2021). Triggering an unexpected earthquake in an uncoupled subduction zone. *Science Advances*, *7*, eabf7590.

Hill, E. M., Yue, H., Barbot, S., Lay, T., Tapponnier, P., Hermawan, I., et al. (2015). The 2012 Mw 8.6 Wharton Basin sequence: A cascade of earthquakes generated by near orthogonal, young, oceanic mantle faults. *Journal of Geophysical Research*, *120*, 3723–3747.

Holdahl, S. R., & Sauber, J. (1994). Coseismic slip in the 1964 Prince William Sound earthquake: A new geodetic inversion. *Pure and Applied Geophysics*, *142*, 55–82.

House, L. S., Sykes, L. R., Davies, J. N., & Jacob, K. H. (1981). Identification of a possible seismic gap near Unalaska Island, eastern Aleutians. In D. W. Simpson & P. G. Richards (Eds.), *Alaska, in earthquake prediction – An international review*, Maurice Ewing Series (Vol. *4*, pp. 81–92). Washington, D. C: AGU.

Hreinsdottir, S., Freymueller, J. T., Burgmann, R., & Mitchell, J. (2006). Coseismic deformation of the 2002 Denali Fault earthquake: Insights from GPS measurements. *Journal of Geophysical Research*, *111*, B03308. https://doi.org/10.1130/10.1029/2005JB003676

Hu, Y., & Freymueller, J. T. (2019). Geodetic observations of time-variable glacial isostatic adjustment in Southeast Alaska and its implications for Earth rheology. *Journal of Geophysical Research: Solid Earth*, *124*, 9870–9889. http://dx.doi.org/10.1029/2018JB017028

Huang, K., Hu, Y., & Freymueller, J. T. (2020). Decadal viscoelastic postseismic deformation of the 1964 Mw9.2 Alaska earthquake. *Journal of Geophysical Research*, *125*(9), e2020JB019649. http://dx.doi.org/10.1029/2020JB019649

Ichinose, G. A., Somerville, P., Thio, H. K., Graves, R., & O'Connell, D. (2007). Rupture process of the 1964 Prince William Sound, Alaska, earthquake from the combined inversion of seismic, tsunami, and geodetic data. *Journal of Geophysical Research*, *112*, B07306. http://dx.doi.org/10.1029/2006JB004728

International Seismological Centre. (2023), On-line Bulletin, https://doi.org/10.31905/D808B830. Event ID 886030.

Johnson, J. M., & Satake, K. (1994). Rupture extent of the 1938 Alaskan earthquake as inferred from tsunami waveforms. *Geophysical Research Letters*, *21*, 733–736. http://dx.doi.org/10.1029/94gl00333

Johnson, J. M., Satake, K., Holdahl, S. R., & Sauber, J. (1996). The 1964 Prince William Sound earthquake: Joint inversion of tsunami and geodetic data. *Journal of Geophysical Research*, *101*, 523–532.

Johnson, J. M., Tanioka, Y., Ruff, L. J., Satake, K., Kanamori, H., & Sykes, L. R. (1994). The 1957 great Aleutian earthquake. *Pure and Applied Geophysics*, *142*, 3–28.

Kim, Y., Abers, G. A., Li, J., Christensen, D., Calkins, J., & Rondenay, S. (2014). Alaska Megathrust 2: Imaging the megathrust zone and Yakutat/Pacific plate interface in the Alaska subduction zone. *Journal of Geophysical Research – Solid Earth*, *119*, 1924–1941. http://dx.doi.org/10.1002/2013JB010581

Koehler, R.D., Farrell, Rebecca-Ellen, Burns, P.A.C., and Combellick, R.A., 2012, *Quaternary faults and folds in Alaska: A digital database*, in Koehler, R.D., Quaternary Faults and Folds (QFF): Alaska Division of Geological & Geophysical Surveys Miscellaneous Publication 141, 31 p., 1 sheet, scale 1 : 3,700,000. http://dx.doi.org/10.14509/23944.

Kogan, M. G., Frolov, D. I., Vasilenko, N. F., Freymueller, J. T., Steblov, G. M., Ekström, G., et al. (2017). Plate coupling and strain in the far western Aleutian arc modeled from GPS data. *Geophysical Research Letters*, *44*, 3176–3183. http://dx.doi.org/10.1002/2017GL072735

Krabbenhoeft, A., von Huene, R., Miller, J. J., Lange, D., & Vera, F. (2018). Strike-slip 23 January 2018 Mw7.9 Gulf of Alaska rare intraplate earthquake: Complex rupture of a fracture zone system. *Nature*, *8*, 13706. https://doi.org/10.1038/s41598-01832071-4

Kreemer, C., Hammond, W. C., & Blewitt, G. (2018). A robust estimation of the 3-D intraplate deformation of the North American plate from GPS. *Journal of Geophysical Research*, *123*. http://dx.doi.org/10.1029/2017JB015257

Lahr, J. C., & Plafker, G. (1980). Holocene Pacific-North American plate interaction in southern Alaska: Implications for the Yakataga seismic gap. *Geology*, *8*, 483–486.

Lander, J.F. (1996). Tsunamis affecting Alaska, U.S. Department of Commerce, National Ocean and Atmospheric Administration, National Environmental Satellite Data and Information Service, National Geophysical Data Center, Boulder, CO, 195 p.

Larsen, C. F., Motyka, R. J., Freymueller, J. T., Echelmeyer, K. A., & Ivins, E. R. (2005). Rapid viscoelastic uplift in southeast Alaska caused by post-Little Ice Age glacial retreat. *Earth and Planetary Science Letters*, *237*, 548–560. http://dx.doi.org/10.1016/j.epsl.2005.06.032

Lay, T., Ye, L., Bai, Y., Cheung, K. F., Kanamori, H., Freymueller, J., et al. (2017). Rupture along 400 km of the Bering fracture zone in the Komandorsky Islands earthquake

(MW 7.8) of 17 July 2017. *Geophysical Research Letters, 44*. http://dx.doi.org/10.1002/2017GL076148

Lay, T., Ye, L., Kanamori, H., Yamazaki, Y., Cheung, K.-F., Kwong, K., & Koper, K. D. (2013). The October 28, 2012 M7.8 Haida Gwaii underthrusting earthquake and tsunami: Slip par- titioning along the Queen Charlotte Fault transpressional plate boundary. *Earth and Planetary Sci. Lett., 375*. http://dx.doi.org/10.1016/j.epsl.2013.05.005

Leonard, L., & Bednarski, J. (2014). Field survey following the 28 October 2012 Haida Gwaii tsunami. *Pure and Applied Geophysics, 171*, 3467–3482. http://dx.doi.org/10.1007/s00024-014-0792-0

Leonard, L. J., Hyndman, R. D., Mazzotti, S., Nykolaishen, L., Schmidt, M., & Hippchen, S. (2007). Current deformation in the northern Canadian Cordillera inferred from GPS measurements. *Journal of Geophysical Research, 112*, B11401. http://dx.doi.org/10.1029/2007JB005061

Leonard, L. J., Mazzotti, S., & Hyndman, R. D. (2008). Deformation rates estimated from earthquakes in the northern Cordillera of Canada and eastern Alaska. *Journal of Geophysical Research, 113*, B08406. http://dx.doi.org/10.1029/2007JB005456

Li, H., Wei, M., Li, D., Liu, Y., Kim, Y., & Zhou, S. (2018). Segmentation of slow slip events in south central Alaska possibly controlled by a subducted oceanic plateau. *Journal of Geophysical Research: Solid Earth, 123*, 418–436. http://dx.doi.org/10.1002/2017JB014911

Li, S., & Freymueller, J. T. (2018). Spatial variation of slip behavior beneath the Alaska Peninsula along Alaska–Aleutian subduction zone. *Geophysical Research Letters, 45*. http://dx.doi.org/10.1002/2017GL076761

Li, S., Freymueller, J., & McCaffrey, R. (2016). Slow slip events and time-dependent variations in locking beneath Lower Cook Inlet of the Alaska–Aleutian subduction zone. *Journal of Geophysical Research – Solid Earth, 121*, 1060–1079. http://dx.doi.org/10.1002/2015JB012491

Liberty, L. M., Brothers, D. S., & Haeussler, P. J. (2019). Tsunamigenic splay faults imply a long-term asperity in southern Prince William Sound, Alaska. *Geophysical Research Letters, 46*, 3764–3772. https://doi.org/10.1029/2018GL081528

Lisowski, M., Savage, J. C., & Buford, R. O. (1987). Strain accumulation across the Fairweather and Totschunda faults, Alaska. *Journal of Geophysical Research, 92*, 11,552–11,560.

Liu, C., Lay, T., Xie, Z., & Xiong, X. (2019). Intraslab deformation in the 30 November 2018 Anchorage, Alaska, MW 7.1 earthquake. *Geophysical Research Letters, 46*, 2449–2457. http://dx.doi.org/10.1029/2019GL082041

Liu, C., Lay, T., & Xiong, X. (2022). The 29 July 2021 MW 8.2 Chignik, Alaska Peninsula earthquake rupture inferred from seismic and geodetic observations: Re-Rupture of the Western 2/3 of the 1938 rupture zone. *Geophysical Research Letters, 49*, e2021GL096004. http://dx.doi.org/10.1029/2021GL096004

Liu, C., Lay, T., Xiong, X., & Wen, Y. (2020). Rupture of the 2020 MW 7.8 earthquake in the Shumagin gap inferred from seismic and geodetic observations. *Geophysical Research Letters, 47*, e2020GL090806. http://dx.doi.org/10.1029/2020GL090806

Liu, L., & Larson, K. M. (2018). Decadal changes of surface elevation over permafrost area estimated using reflected

GPS signals. *The Cryosphere, 12*, 477–489. http://dx.doi.org/10.5194/tc-12-477-2018

López, A. M., & Okal, E. A. (2006). A seismological reassessment of the source of the 1946 Aleutian "tsunami" earthquake. *Geophysical Journal International, 165*, 835–849.

Ma, C., Sauber, J. M., Bell, L. J., Clark, T. A., Gordon, D., Himwich, W. E., & Ryan, J. W. (1990). Measurement of horizontal motions in Alaska using very long baseline interferometry. *Journal of Geophysical Research, 95*(B13), 21,991–22,011.

Mackey, K. G., Fujita, K., Hartse, H. E., Stead, R. J., Steck, L. K., Gunbina, L. V., et al. (2010). Seismicity map of eastern Russia, 1960-2010. *Seismological Research Letters, 81*(5), 761–768. http://dx.doi.org/10.1785/gssrl.81.5.761

Macpherson, K. A., & Ruppert, N. A. (2015). Evidence of Wadati-Benioff zone triggering following the M_w 7.9 Little Sitkin, Alaska intermediate depth earthquake of 23 June 2014. *Geophysical Research Letters, 42*, 6269–6277. http://dx.doi.org/10.1002/2015GL065023

Mao, A., Harrison, C. G. A., & Dixon, T. H. (1999). Noise in GPS coordinate time series. *Journal of Geophysical Research, 104*, 2797–2816.

Marechal, A., Mazzotti, S., Elliott, J. L., Freymueller, J. T., & Schmidt, M. (2015). Indentor corner tectonics in the Yakutat-St. Elias collision constrained by GPS. *Journal of Geophysical Research – Solid Earth, 120*, 3897–3908. http://dx.doi.org/10.1002/2014JB011842

Mazzotti, S., & Hyndman, R. D. (2002). Yakutat collision and strain transfer across the northern Canadian Cordillera. *Geology, 30*(6), 495–498. http://dx.doi.org/10.1130/0091-7613(2002)030%3c0495:YCASTA%3e2.0.CO;2

Mazzotti, S., Leonard, L. J., Hyndman, R. D. and Cassidy, J. F. (2008). *Tectonics, Dynamics, and Seismic Hazard in the Canada-Alaska Cordillera*. In Active Tectonics and Seismic Potential of Alaska (Eds. J.T. Freymueller, P.J. Haeussler, R.L. Wesson and G. Ekström). http://dx.doi.org/10.1029/179GM17

McCaffrey, R. (2002). Crustal block rotations and plate coupling. Plate boundary zones. In S. Stein & J. T. Freymueller (Eds.), *Plate boundary zones* (pp. 101–122). Washington, DC: American Geophysical Union. https://doi.org/10.1029/GD030p0101

McConeghy, J., Flesch, L., & Elliott, J. (2022). Investigating the effect of mantle flow and viscosity structure on surface velocities in Alaska using 3-D geodynamic models. *Journal of Geophysical Research: Solid Earth, 127*, e2022JB024704. http://dx.doi.org/10.1029/2022JB024704

Miller, M. S., & Moresi, L. (2018). Mapping the Alaskan Moho. *Seismological Research Letters, 1–7*. http://dx.doi.org/10.1785/0220180222

Mulia, I. E., Heidarzadeh, M., & Satake, K. (2022). Effects of depth of fault slip and continental shelf geometry on the generation of anomalously long-period tsunami by the July 2020 *M*w 7.8 Shumagin (Alaska) earthquake. *Geophysical Research Letters, 49*, e2021GL094937. http://dx.doi.org/10.1029/2021GL094937

Nicolsky, D. J., Freymueller, J. T., Witter, R. C., Suleimani, E. N., & Koehler, R. D. (2016). Evidence for shallow megathrust slip across the Unalaska seismic gap during the great

1957 Andreanof Islands earthquake, eastern Aleutian Islands, Alaska. *Geophysical Research Letters*, *43*, 10,328–10,337. http://dx.doi.org/10.1002/2016GL070704

Nishenko, S. P., & Jacob, K. H. (1990). Seismic potential of the Queen Charlotte-Alaska–Aleutian seismic zone. *Journal of Geophysical Research*, *95*, 2511–2532.

Nykolaishen, L., Dragert, H., Wang, K., James, T. S., & Schmidt, M. (2015). GPS observations of crustal deformation associated with the 2012 Mw 7.8 Haida Gwaii earthquake. *Bulletin of the Seismological Society of America 2015*, *105*(2B), 1241–1252. http://dx.doi.org/10.1785/0120140177

Ohta, Y., Freymueller, J. T., Hreinsdóttir, S., & Suito, H. (2006). A large slow slip event and the depth of the seismogenic zone in the south central Alaska subduction zone. *Earth and Planetary Science Letters*, *247*(1–2), 108–116.

Ohta, Y., Freymueller, J. T., & Miura, S. (2007). The time constant variations of slow slip events in the south Alaska subduction zone. *Eos, Transactions American Geophysical Union*, *88*(52). Fall Meet. Suppl., Abstract T21A-0364

Okal, E. A. (1992). Use of the mantle magnitude Mm for the reassessment of the moment of historical earthquakes. *Pure and Applied Geophysics*, *139*(1), 17–57.

Pegler, G., & Das, S. (1996). The 1987-1992 Gulf of Alaska earthquakes. *Tectonophysics*, *257*, 111–136.

Peltier, W. R., Argus, D. F., & Drummond, R. (2015). Space geodesy constrains ice-age terminal deglaciation: The global ICE-6G_C (VM5a) model. *Journal of Geophysical Research – Solid Earth*, *120*, 450–487. http://dx.doi.org/10.1002/2014JB011176

Piersanti, A., Spada, G., & Sabadini, R. (1997). Global postseismic rebound of a viscoelastic Earth: Theory for finite faults and application to the 1964 Alaska earthquakes. *Journal of Geophysical Research*, *102*, 477–492.

Plafker, G., & Berg, H. C. (1994). Overview of the goelogy and tectonic evolution of Alaska. In G. Plafker & H. C. Berg (Eds.), *The Geology of Alaska* (pp. 989–1021). Colorado, Boulder: Geological Society of America.

Ramos, M. D., Liberty, L. M., Haeussler, P. J., & Humprehyes, R. (2022). Upper-plate structure and tsunamigenic faults near the Kodiak Islands, Alaska, USA. *Geopshere*, *18*(5), 1473–1491. http://dx.doi.org/10.1130/GES02486.1

Rebischung, P. and Schmid, R. (2016). IGS14/igs14.atx: a new framework for the IGS products. *Am. Geophys.* Union, Fall Meeting 2016. File download at https://files.igs.org/pub/station/general/igs14.atx.

Richter, D. H., & Matson, N. A. (1971). Quaternary faulting in the eastern Alaska Range. *Geological Society of America Bulletin*, *82*, 1529–1540.

Rollins, C., J. T. Freymueller, X. Xue, S. Holtkamp, T. Loga, F. Meyer, and J. Patton (this volume). *The 2018 Kaktovik, Alaska earthquakes: insights from an integrated regional earthquake catalog and InSAR-based deformation models, and implications for the North Slope.*

Rousset, B., Fu, Y., Bartlow, N. M., & Bürgmann, R. (2019). Weeks-long and years-long slow slip and tectonic tremor episodes on the south central Alaska megathrust. *Journal of Geophysical Research: Solid Earth*, *124*, 13392–13403. http://dx.doi.org/10.1029/2019JB018724

Ruppert, N. A., Nayak, A., Thurber, C., & Richards, C. (2020). Aftershock analysis of the 2018 MW 7.1 Anchorage, Alaska, earthquake: Relocations and regional moment tensors. *Seismological Research Letters*, *91*, 114–125. http://dx.doi.org/10.1785/0220190199

Ruppert, N. A., Ridgway, K. D., Freymueller, J. T., Cross, R. S., & Hansen, R. A. (2008). Active Tectonics of Interior Alaska: Seismicity, GPS Geodesy, and Local Geomorphology. In J. T. Freymueller, P. J. Haeussler, R. L. Wesson, & G. Ekström (Eds.), *Active Tectonics and Seismic Potential of Alaska*. AGU Publications. https://doi.org/10.1029/179GM06

Ruppert, N. A., Rollins, C., Zhang, A., Meng, L., Holtkamp, S. G., West, M. E., & Freymueller, J. T. (2018). Complex faulting and triggered rupture during the 2018 MW7.9 offshore Kodiak, Alaska, earthquake. *Geophysical Research Letters*, *45*. http://dx.doi.org/10.1029/2018GL078931

Sauber, J. M., Clark, T. A., Bell, L. J., Lisowski, M., Ma, C., & Caprette, D. S. (1993). Geodetic measurement of static displacement associated with the 1987-1988 Gulf of Alaska earthquakes. In D. E. Smith & D. L. Turcotte (Eds.), *Contributions of space geodesy to geodynamics: Crustal dynamics 23*. American Geophysical Union.

Savage, J. C., & Burford, R. O. (1973). Geodetic determination of relative plate motion in central California. *Journal of Geophysical Research*, *78*(5), 832–845. http://dx.doi.org/10.1029/JB078i005p00832

Savage, J. C., Lisowski, M., & Prescott, W. H. (1981). Strain accumulation across the Denali Fault in the Delta River Canyon. *Alaska. Journal of Geophysical Research*, *86*(B2), 1005–1014. https://doi.org/10.1029/JB086iB02p01005

Schmalzle, G. M., McCaffrey, R., & Creager, K. C. (2014). Central Cascadia subduction zone creep. *Geochemistry, Geophysics, Geosystems*, *15*, 1515–1532. http://dx.doi.org/10.1002/2013GC005172

Scholz, C. (2002). *The mechanics of earthquakes and faulting* (2nd ed.). Cambridge: Cambridge University Press.

Segall, P. (2010). *Earthquake and volcano deformation* (pp. 200–266). Princeton, NJ: Princeton University Press. https://doi.org/10.1515/9781400833856

Segou, M., & Parsons, T. (2020). The role of seismic and slow slip events in triggering the 2018 *M*7.1 Anchorage earthquake in the Southcentral Alaska subduction zone. *Geophysical Research Letters*, *47*, e2019GL086640. http://dx.doi.org/10.1029/2019GL086640

Shillington, D. J., Bécel, A., Nedimovic, M. R., Kuehn, H., Webb, S. C., Abers, G. A., et al. (2015). Link between plate fabric, hydration and subduction zone seismicity in Alaska. *Nature Geoscience*, *8*(12), 961–964.

Sigmundsson, F., Parks, M., Pedersen, R., Jónsdottir, K., Ófeigsson, B. G., Grapenthin, R., et al. (2018). Chapter 11 – Magma Movements in Volcanic Plumbing Systems and their Associated Ground Deformation and Seismic Patterns. In S. Burchardt (Ed.), *Volcanic and Igneous Plumbing Systems* (pp. 285–322). Elsevier.

Singh, S., et al. (2017). The discovery of a conjugate system of faults in the Wharton Basin intraplate deformation zone. *Science Advances*, *3*, e1601689. https://doi.org/10.1126/sciadv.1601689

Small, J. B., & Wharton, L. C. (1972). Vertical displacements. In *The great Alaska earthquake of 1964, seismology and geodesy* (pp. 449–461). Washington, D.C.: National Academy of Sciences.

Suito, H., & Freymueller, J. T. (2009). A viscoelastic and afterslip postseismic deformation model for the 1964 Alaska earthquake. *Journal of Geophysical Research, 114*, B11404. http://dx.doi.org/10.1029/2008JB005954

Suleimani, E., & Freymueller, J. T. (2020). Near-field modeling of the 1964 Alaska tsunami: The role of splay faults and horizontal displacements. *Journal of Geophysical Research: Solid Earth, 125*, e2020JB019620. http://dx.doi.org/10.1029/2020JB019620

Sykes, L. R., Kisslinger, J. B., House, L., Davies, J. N., & Jacob, K. H. (1980). Rupture zones of great earthquakes in the Alaska-Aleutian Arc, 1784 to 1980. *Science, 210*(4476), 1343–1345. https://doi.org/10.1126/science.210.4476.1343

Tian, Z., Freymueller, J. T., & Yang, Z. (2021). Postseismic deformation due to the 2012 Mw 7.8 Haida Gwaii and 2013 Mw 7.5 Craig earthquakes and its implications for regional rheological structure. *Journal of Geophysical Research: Solid Earth, 126*, e2020JB020197. http://dx.doi.org/10.1029/2020JB020197

Twardzik, C., & Ji, C. (2015). The Mw7.9 2014 intraplate intermediate-depth Rat Islands earthquake and its relation to regional tectonics. *Earth and Planetary Science Letters, 431*, 26–35. http://dx.doi.org/10.1016/j.epsl.2015.08.033

Wei, M., McGuire, J. J., & Richardson, E. (2012). A slow slip event in the south central Alaska Subduction Zone and related seismicity anomaly. *Geophysical Research Letters, 39*, L15309. http://dx.doi.org/10.1029/2012GL052351

Wei, S., Helmberger, D., & Avouac, J.-P. (2013). Modeling the 2012 Wharton Basin earthquake off Sumatra; complete lithospheric failure. *Journal of Geophysical Research, 118*, 3592–3609.

Wessel, P., Smith, W. H. F., Scharroo, R., Luis, J., & Wobbe, F. (2013). Generic mapping tools: Improved version released. *Eos, Transactions American Geophysical Union, 94*(45), 409.

Witter, R. C., Briggs, R. W., Engelhart, S. E., Gelfenbaum, G., Koehler, R. D., & Barnhart, W. D. (2014). Little late Holocene strain accumulation and release on the Aleutian megathrust below the Shumagin Islands, Alaska. *Geophysical Research Letters, 41*, 2359–2367. https://doi.org/10.1130/10.1002/2014GL059393

Witter, R. C., Carver, G. A., Briggs, R. W., Gelfenbaum, G., Koehler, R. D., La Selle, S. P., et al. (2016). Unusually large tsunamis frequent a currently creeping part of the Aleutian megathrust. *Geophysical Research Letters, 43*, 76–84. http://dx.doi.org/10.1002/2015GL066083

Worthington, L. L., Van Avendonk, H. J. A., Gulick, S. P. S., Christeson, G. L., & Pavlis, T. L. (2012). Crustal structure of the Yakutat terrane and the evolution of subduction and collision in southern Alaska. *Journal of Geophysical Research, 117*, B01102. https://doi.org/10.1130/10.1029/2011JB008493

Xiao, Z., Freymueller, J. T., Grapenthin, R., Elliott, J. L., Drooff, C., & Fusso, L. (2021). The deep Shumagin gap filled: Kinematic rupture model and slip budget analysis of the 2020 mw 7.8 Simeonof earthquake constrained by GNSS, global seismic waveforms, and floating InSAR. *Earth and Planetary Science Letters, 576*, 117241. http://dx.doi.org/10.1016/j.epsl.2021.117241

Xue, X., & Freymueller, J. T. (2020). A 25-year history of volcano magma supply in the east central Aleutian arc, Alaska. *Geophysical Research Letters, 47*, e2020GL088388. http://dx.doi.org/10.1029/2020GL088388

Xue, X., Freymueller, J., & Lu, Z. (2020). Modeling the post-eruptive deformation at Okmok based on the GPS and InSAR timeseries: Changes in the shallow magma storage system. *Journal of Geophysical Research, 125*, e2019JB017801. https://doi.org/10.1029/2019JB017801

Ye, L., Bai, Y., Si, D., Lay, T., Cheung, K. F., & Kanamori, H. (2022). Rupture model for the 29 July 2021 M_w 8.2 Chignik, Alaska earthquake constrained by seismic, geodetic, and tsunami observations. *Journal of Geophysical Research: Solid Earth, 127*, e2021JB023676. http://dx.doi.org/10.1029/2021JB023676

Ye, L., T. Lay, H. Kanamori, J. Freymueller, and L. Rivera (2016). *Joint inversion of high-rate GPS and teleseismic observations for rupture process of the 23 June 2014 (Mw 7.9) Rat Islands archipelago, Alaska, intermediate-depth earthquake*, Natural Hazards and Plate Boundaries, in Plate Boundaries and Natural Hazards, AGU Geophysical Monograph 219, João C. Duarte and Wouter P. Schellart, editors, 149–166.

Ye, L., Lay, T., Kanamori, H., Yamazaki, Y., & Cheung, K. F. (2021). The 22 July 2020 MW 7.8 Shumagin seismic gap earthquake: Partial rupture of a weakly coupled megathrust. *Earth and Planetary Science Letters, 562*, 116879. http://dx.doi.org/10.1016/j.epsl.2021.116879

Yue, H., Lay, T., Freymueller, J. T., Ding, K., Rivera, L., Ruppert, N. A., & Koper, K. D. (2013). Supershear rupture of the 5 January 2013 Craig, Alaska (Mw 7.5) earthquake. *Journal of Geophysical Research: Solid Earth, 118*, 5903–5919. http://dx.doi.org/10.1002/2013JB010594

Zhao, B., Bürgmann, R., Wang, D., Zhang, J., Yu, J., & Li, Q. (2022). Aseismic slip and recent ruptures of persistent asperities along the Alaska–Aleutian subduction zone. *Nature Communications, 13*. http://dx.doi.org/10.1038/s41467-022-30883-7

Zhou, Y., Wang, W., He, J., et al. (2022). The 19 October 2020 M_w 7.6 earthquake in Shumagin, Alaska: An unusual dextral strike-slip event. *Pure and Applied Geophysics, 179*, 3527–3542. http://dx.doi.org/10.1007/s00024-022-03001-3

Zumberge, J. F., Heflin, M. B., Jefferson, D. C., Watkins, M. M., & Webb, F. H. (1997). Precise point positioning for the efficient and robust analysis of GPS data from large networks. *Journal of Geophysical Research: Solid Earth, 102*(B3), 5005–5017. http://dx.doi.org/10.1029/96JB03860

DATA REFERENCES

Elliott, Julie L., 2020, Wrangells GPS Network – GLNS-Glennallen School P.S., GAGE Facility, GPS/GNSS Observations Dataset, https://doi.org/10.7283/92QD-3322

Elliott, Julie L., 2020, Wrangells GPS Network – MNDA-Mendeltna Lodge P.S., GAGE Facility,

GPS/GNSS Observations Dataset, https://doi.org/10.7283/JV54-VC12

Elliott, Julie L., 2020, Wrangells GPS Network – TPLL-The Point Lodge P.S., GAGE Facility, GPS/GNSS Observations Dataset, https://doi.org/10.7283/A0CB-EJ51

Elliott, Julie L., Freymueller, Jeffrey T., 2020, RAPID Alaska Response GPS Network – FS63-FS63_WAS_USA2019 P.S., GAGE Facility, GPS/GNSS Observations Dataset, https://doi.org/10.7283/ER2B-EM67

Elliott, Julie L., Freymueller, Jeffrey T., 2020, RAPID Alaska Response GPS Network – FS82-FS82_BIG_USA2019 P.S., GAGE Facility, GPS/GNSS Observations Dataset, https://doi.org/10.7283/5A73-XR88

Elliott, Julie L., Freymueller, Jeffrey T., 2020, RAPID Alaska Response GPS Network – PMKZ-PMKZ_PMA_USA2019 P.S., GAGE Facility, GPS/GNSS Observations Dataset, https://doi.org/10.7283/ZPAK-PT10

Elliott, Julie L., Freymueller, Jeffrey T., 2020, RAPID Alaska Response GPS Network – STEM-STEM_WAS_USA2019 P.S., GAGE Facility, GPS/GNSS Observations Dataset, https://doi.org/10.7283/TQPA-R111

Freymueller, Jeffrey T., 1998, Alaska GPS Network – CLGO-College Observatory P.S., UNAVCO, GPS/GNSS Observations Dataset, https://doi.org/10.7283/T5P55KJV

Freymueller, Jeffrey T., 2002, Denali 2000, UNAVCO, GPS/GNSS Observations Dataset, https://doi.org/10.7283/T5GT5KJJ

Freymueller, Jeffrey T., 2003, Denali Fault GPS Network – ATTC-AT&T P.S., UNAVCO, GPS/GNSS Observations Dataset, https://doi.org/10.7283/T55Q4TGB

Freymueller, Jeffrey T., 2003, Denali Highway P.S."–"BITS-Mile 97, UNAVCO, GPS/GNSS Observations Dataset, 10.7283/T5JW8C8X

Freymueller, Jeffrey T., 2003, Denali Fault GPS Network – DH32-Denali Highway Milepost 32 P.S., UNAVCO, GPS/GNSS Observations Dataset, https://doi.org/10.7283/T5F769XC

Freymueller, Jeffrey T., 2003, Denali Fault GPS Network – DLTJ-Delta Junction P.S., UNAVCO, GPS/GNSS Observations Dataset, https://doi.org/10.7283/T5X63K9G

Freymueller, Jeffrey T., 2003, Denali Fault GPS Network – DNLC-Donnelly Continuous P.S., UNAVCO, GPS/GNSS Observations Dataset, https://doi.org/10.7283/T5QN6541

Freymueller, Jeffrey T., 2003, Denali Fault GPS Network – DRMC-Mount Drum Viewpoint Cont. P.S., UNAVCO, GPS/GNSS Observations Dataset, https://doi.org/10.7283/T52Z13XT

Freymueller, Jeffrey T., 2003, Denali Fault GPS Network – FRIG-Refrigerator Rock P.S., UNAVCO, GPS/GNSS Observations Dataset, https://doi.org/10.7283/T5Z60MFV

Freymueller, Jeffrey T., 2003, Denali Fault GPS Network – HIWC-Highway Continuous P.S., UNAVCO, GPS/GNSS Observations Dataset, https://doi.org/10.7283/T56Q1VMQ

Freymueller, Jeffrey T., 2003, Denali Fault GPS Network – HURC-Hurricane Gulch Continuous P.S., UNAVCO, GPS/GNSS Observations Dataset, https://doi.org/10.7283/T5KW5DD9

Freymueller, Jeffrey T., 2003, Denali Fault GPS Network – JANL-Jan Lake P.S., UNAVCO, GPS/GNSS Observations Dataset, https://doi.org/10.7283/T5G44NPW

Freymueller, Jeffrey T., 2003, Denali Fault GPS Network – MENT-Mentasta P.S., UNAVCO, GPS/GNSS Observations Dataset, https://doi.org/10.7283/T5BG2MBF

Freymueller, Jeffrey T., 2003, Denali Fault GPS Network – PAX2-Paxson 2 P.S., UNAVCO, GPS/GNSS Observations Dataset, https://doi.org/10.7283/T59G5K62

Freymueller, Jeffrey T., 2003, Denali Fault GPS Network – SDOU-Sourdough P.S., UNAVCO, GPS/GNSS Observations Dataset, https://doi.org/10.7283/T51Z42SF

Freymueller, Jeffrey T., 2006, Southeast Alaska GPS Network – BMCP-Blue Mouse Cove Permanent P.S., UNAVCO, GPS/GNSS Observations Dataset, https://doi.org/10.7283/GTYV-T296

Freymueller, Jeffrey T., 2006, Southeast Alaska GPS Network – MDFC-Million Dollar Falls Continuous P.S, UNAVCO, GPS/GNSS Observations Dataset, https://doi.org/10.7283/S92T-2737

Freymueller, Jeffrey T., 2006, Southeast Alaska GPS Network – QUIC-Queen Inlet Continuous P.S., UNAVCO, GPS/GNSS Observations Dataset, https://doi.org/10.7283/9YT1-M292

Freymueller, Jeffrey T., 2007, Southeast Alaska GPS Network – ALSC-Alsek Continuous P.S., UNAVCO, GPS/GNSS Observations Dataset, https://doi.org/10.7283/WHEH-8Y14

Freymueller, Jeffrey T., 2007, Southeast Alaska GPS Network – ELDC-Eldred Rock Continuous P.S., UNAVCO, GPS/GNSS Observations Dataset, https://doi.org/10.7283/684D-Y361

Freymueller, Jeffrey T., 2007, Southeast Alaska GPS Network – TATC-TATS Continuous P.S., UNAVCO, GPS/GNSS Observations Dataset, https://doi.org/10.7283/2XTN-4T38

Freymueller, Jeffrey T., 2013, Alaska Volcano Observatory GPS Network – DUTC-Dutch Harbor AVO P.S., GAGE Facility, GPS/GNSS Observations Dataset, https://doi.org/10.7283/T51G0JPJ

Freymueller, Jeffrey T., 2014, Southeast Alaska GPS Network – KLRS-Kluane Lake Research Station 1 Hz P.S., UNAVCO, GPS/GNSS Observations Dataset, https://doi.org/10.7283/GKDS-QM56

Freymueller, Jeffrey T., 2015, Denali Fault GPS Network – HAAR-HAARP P.S., UNAVCO, GPS/GNSS Observations Dataset, https://doi.org/10.7283/T5J101JQ

Freymueller, Jeffrey T., 2015, Denali Fault GPS Network – ZINA-Nizina P.S., UNAVCO, GPS/GNSS Observations Dataset, https://doi.org/10.7283/T5NP22TZ

Freymueller, Jeffrey T., 2015, MacKenzie Mountains GPS Network – MMEP-MacMillan Pass P.S., UNAVCO, GPS/GNSS Observations Dataset, https://doi.org/10.7283/T54Q7SCD

Freymueller, Jeffrey T., 2016, MacKenzie Mountains GPS Network – CJOU-Carcajou Lake P.S., UNAVCO, GPS/GNSS Observations Dataset, https://doi.org/10.7283/T58G8J34

Freymueller, Jeffrey T., 2016, MacKenzie Mountains GPS Network – HAYL-Hay Lake P.S., UNAVCO, GPS/GNSS Observations Dataset, https://doi.org/10.7283/T5D798TF

Freymueller, Jeffrey T., Grapenthin, Ronni, 2003, Alaska Volcano Observatory GPS Network Okmok – OKCE-Okmok

Cone E P.S., UNAVCO, GPS/GNSS Observations Dataset, https://doi.org/10.7283/T5TX3CR4

Freymueller, Jeffrey T., Grapenthin, Ronni, 2003, Alaska Volcano Observatory GPS Network Okmok – OKFG-Okmok Fort Glenn P.S., UNAVCO, GPS/GNSS Observations Dataset, https://doi.org/10.7283/T5Q81BFF

Freymueller, Jeffrey T., Grapenthin, Ronni, 2004, Alaska Volcano Observatory GPS Network Okmok – OKSO-Okmok South P.S., UNAVCO, GPS/GNSS Observations Dataset, https://doi.org/10.7283/T5FQ9V0V

Freymueller, Jeffrey T., Grapenthin, Ronni, 2004, Alaska Volcano Observatory GPS Network Spurr – SPBG-Barrier Glacier P.S., UNAVCO, GPS/GNSS Observations Dataset, https://doi.org/10.7283/T5DR2SVM

Freymueller, Jeffrey T., Grapenthin, Ronni, 2004, Alaska Volcano Observatory GPS Network Spurr – SPCG-Capps Glacier P.S., UNAVCO, GPS/GNSS Observations Dataset, https://doi.org/10.7283/T55719D8

Freymueller, Jeffrey T., Grapenthin, Ronni, 2004, Alaska Volcano Observatory GPS Network Spurr – SPCR-Chakachatna River P.S., UNAVCO, GPS/GNSS Observations Dataset, https://doi.org/10.7283/T5902240

Freymueller, Jeffrey T., Grapenthin, Ronni, 2010, Alaska Volcano Observatory GPS Network Okmok – OKNC-Okmok Cone B P.S., UNAVCO, GPS/GNSS Observations Dataset, https://doi.org/10.7283/T5KH0KQQ

Freymueller, Jeffrey T., Grapenthin, Ronni, 2010, Alaska Volcano Observatory GPS Network Redoubt – RDJH-Redoubt Jurgen's Hut P.S., UNAVCO, GPS/GNSS Observations Dataset, https://doi.org/10.7283/T5P84992

Freymueller, Jeffrey T., Grapenthin, Ronni, 2011, Alaska Volcano Observatory GPS Network Makushin – MSWB-MSWB P.S., UNAVCO, GPS/GNSS Observations Dataset, https://doi.org/10.7283/T5668BJ3

Freymueller, Jeffrey T., Grapenthin, Ronni, 2011, Alaska Volcano Observatory GPS Network Redoubt – RDSO-Redoubt South P.S., UNAVCO, GPS/GNSS Observations Dataset, https://doi.org/10.7283/T5T1521S

Freymueller, Jeffrey T., Grapenthin, Ronni, 2011, Alaska Volcano Observatory GPS Network Redoubt – RDWB-Redoubt West B P.S., UNAVCO, GPS/GNSS Observations Dataset, https://doi.org/10.7283/T5XP7391

Freymueller, Jeffrey T., Grapenthin, Ronni, 2011, Alaska Volcano Observatory GPS Network Spurr – SPCP-Spurr Crater Peak P.S., UNAVCO, GPS/GNSS Observations Dataset, https://doi.org/10.7283/T5JH3JKB

Freymueller, Jeffrey T., Grapenthin, Ronni, 2012, Alaska Volcano Observatory GPS Network Redoubt – REDC-Redoubt RED Continuous P.S., UNAVCO, GPS/GNSS Observations Dataset, https://doi.org/10.7283/T52F7KSX

Freymueller, Jeffrey T., Grapenthin, Ronni, Paskievitch, John, 2012, Alaska Volcano Observatory GPS Network – MAPS-Makushin Pakushin SE P.S., GAGE Facility, GPS/GNSS Observations Dataset, https://doi.org/10.7283/T5T151S7

Grapenthin, Ronni, 2023, Alaska GPS Network – SUAF-UAF College of Natural Sciences Roof P.S., GAGE Facility, GPS/GNSS Observations Dataset, https://doi.org/10.7283/TGJD-BM44

Grapenthin, Ronni, West, Michael, Freymueller, Jeffrey T., 2013, Alaska Earthquake Center GPS Network – WAT1-Watana 1 P.S., GAGE Facility, GPS/GNSS Observations Dataset, https://doi.org/10.7283/K2PC-S124

Murray, Tom, Freymueller, Jeffrey T., Grapenthin, Ronni, Power, John, 2003, Akutan Volcano GPS Network – AKGG-Akutan Green Grass P.S., GAGE Facility, GPS/GNSS Observations Dataset, https://doi.org/10.7283/SPFZ-W130

Murray, Tom, Freymueller, Jeffrey T., Grapenthin, Ronni, Power, John, 2003, Akutan Volcano GPS Network – AKLV-Akutan Long Valley P.S., GAGE Facility, GPS/GNSS Observations Dataset, https://doi.org/10.7283/Z5CG-PH64

Murray, Tom, Freymueller, Jeffrey T., Grapenthin, Ronni, Power, John, 2003, Akutan Volcano GPS Network – AKMO-Akutan Morgan P.S., GAGE Facility, GPS/GNSS Observations Dataset, https://doi.org/10.7283/TXN2-W085

Murray, Tom, Freymueller, Jeffrey T., Grapenthin, Ronni, Power, John, 2003, Akutan Volcano GPS Network – AKRB-Akutan Reef Bight P.S., GAGE Facility, GPS/GNSS Observations Dataset, https://doi.org/10.7283/9NSF-ZY90

Paskievitch, John, 2012, Alaska Volcano Observatory GPS Network – MREP-Makushin Repeater P.S., UNAVCO, GPS/GNSS Observations Dataset, https://doi.org/10.7283/T5P8492X

Stuckey, Jason, 2013, Arctic PI Continuous – TOOL-Toolik Field Station 1HZ P.S., GAGE Facility, GPS/GNSS Observations Dataset, https://doi.org/10.7283/FC88-3J27

UNAVCO Community, 1998, Alaska GPS Network – CLGO-College Observatory P.S., UNAVCO, GPS/GNSS Observations Dataset, https://doi.org/10.7283/T5DR2SJK

UNAVCO Community, 2000, Alaska GPS Network – ATW2-Alaska Tsunami Warning Centr 2 P.S., GAGE Facility, GPS/GNSS Observations Dataset, https://doi.org/10.7283/7CQA-XE18

UNAVCO Community, 2000, Alaska GPS Network – SELD-Seldovia Airport P.S., GAGE Facility, GPS/GNSS Observations Dataset, https://doi.org/10.7283/QP73-4318

UNAVCO Community, 2002, SuomiNet-G GPS Network – SG27-Barrow SuomiNet P.S., GAGE Facility, GPS/GNSS Observations Dataset, https://doi.org/10.7283/4SCP-AJ10

UNAVCO Community, 2004, PBO GPS Network – AB07-SandPoint_AK2004 P.S., UNAVCO, GPS/GNSS Observations Dataset, https://doi.org/10.7283/T59W0CDH

UNAVCO Community, 2004, PBO GPS Network – AC27-AC27MNeil_AK2004 P.S., UNAVCO, GPS/GNSS Observations Dataset, https://doi.org/10.7283/T5PR7T1N

UNAVCO Community, 2004, PBO GPS Network – AC59-AC59Ursus_AK2004 P.S., UNAVCO, GPS/GNSS Observations Dataset, https://doi.org/10.7283/T5FB510M

UNAVCO Community, 2004, PBO GPS Network – AV01-AV01AUGST_AK2004 P.S., UNAVCO, GPS/GNSS Observations Dataset, https://doi.org/10.7283/T5BZ641Z

UNAVCO Community, 2004, PBO GPS Network – AV02-AV02AUGST_AK2004 P.S., UNAVCO, GPS/GNSS Observations Dataset, https://doi.org/10.7283/T5MG7MH2

UNAVCO Community, 2004, PBO GPS Network – AV04-AV04AUGST_AK2004 P.S., UNAVCO, GPS/GNSS Observations Dataset, https://doi.org/10.7283/T5GQ6VRW

UNAVCO Community, 2004, UNAVCO GPS Network – BASC-Barrow Community Base Station P.S., UNAVCO, GPS/GNSS Observations Dataset, https://doi.org/10.7283/T5JH3JB6

UNAVCO Community, 2004, Alaska GPS Network – GRNX-Garner, AK Existing Networks P.S., GAGE Facility, GPS/GNSS Observations Dataset, https://doi.org/10.7283/PB82-6P80

UNAVCO Community, 2004, PBO GPS Network – AV09-Haystack__AK2004 P.S., UNAVCO, GPS/GNSS Observations Dataset, https://doi.org/10.7283/T5GQ6VP0

UNAVCO Community, 2005, PBO GPS Network – AB06-FalsePass_AK2005 P.S., UNAVCO, GPS/GNSS Observations Dataset, https://doi.org/10.7283/T5MC8X0D

UNAVCO Community, 2005, PBO GPS Network – AB44-SkagwayUSCAK2005 P.S., UNAVCO, GPS/GNSS Observations Dataset, https://doi.org/10.7283/T5DV1GT3

UNAVCO Community, 2005, PBO GPS Network – AB50-MendenhallAK2005 P.S., UNAVCO, GPS/GNSS Observations Dataset, https://doi.org/10.7283/T5B27S7X

UNAVCO Community, 2005, PBO GPS Network – AB51-PetersburgAK2005 P.S., UNAVCO, GPS/GNSS Observations Dataset, https://doi.org/10.7283/T55H7D79

UNAVCO Community, 2005, PBO GPS Network – AB48-PortAlexanAK2005 P.S., UNAVCO, GPS/GNSS Observations Dataset, https://doi.org/10.7283/T54J0C21

UNAVCO Community, 2005, PBO GPS Network – AC02-AkhiokCorpAK2005 P.S., UNAVCO, GPS/GNSS Observations Dataset, https://doi.org/10.7283/T5Z60M01

UNAVCO Community, 2005, PBO GPS Network – AC06-BradleyLakAK2005 P.S., UNAVCO, GPS/GNSS Observations Dataset, https://doi.org/10.7283/T5610X8S

UNAVCO Community, 2005, PBO GPS Network – AC11-ChickaloonAK2005 P.S., UNAVCO, GPS/GNSS Observations Dataset, https://doi.org/10.7283/T5Q81B12

UNAVCO Community, 2005, PBO GPS Network – AC15-CooperLndgAK2005 P.S., UNAVCO, GPS/GNSS Observations Dataset, https://doi.org/10.7283/T52J68SV

UNAVCO Community, 2005, PBO GPS Network – AC20-Gridwood__AK2005 P.S., UNAVCO, GPS/GNSS Observations Dataset, https://doi.org/10.7283/T5C53HSM

UNAVCO Community, 2005, PBO GPS Network – AC25-King_Cove_AK2005 P.S., UNAVCO, GPS/GNSS Observations Dataset, https://doi.org/10.7283/T5SF2T4X

UNAVCO Community, 2005, PBO GPS Network – AC38-Quartz_CrkAK2005 P.S., UNAVCO, GPS/GNSS Observations Dataset, https://doi.org/10.7283/T5VH5KS0

UNAVCO Community, 2005, PBO GPS Network – AV06-AKU_AkutPtAK2005 P.S., UNAVCO, GPS/GNSS Observations Dataset, https://doi.org/10.7283/T5028PFN

UNAVCO Community, 2005, PBO GPS Network – AV07-AKU_NWSlopAK2005 P.S., UNAVCO, GPS/GNSS Observations Dataset, https://doi.org/10.7283/T5V98606

UNAVCO Community, 2005, PBO GPS Network – AV08-AKU_WSlopeAK2005 P.S., UNAVCO, GPS/GNSS Observations Dataset, https://doi.org/10.7283/T5QJ7F8G

UNAVCO Community, 2005, PBO GPS Network – AV10-AKU_SESlopAK2005 P.S., UNAVCO, GPS/GNSS Observations Dataset, https://doi.org/10.7283/T5KW5CZ2

UNAVCO Community, 2005, PBO GPS Network – AV12-AKU_OpenBtAK2005 P.S., UNAVCO, GPS/GNSS Observations Dataset, https://doi.org/10.7283/T5G44N72

UNAVCO Community, 2005, PBO GPS Network – AV13-AKUFumarolAK2005 P.S., UNAVCO, GPS/GNSS Observations Dataset, https://doi.org/10.7283/T5BC3WGW

UNAVCO Community, 2005, PBO GPS Network – AV14-AKU_HarborAK2005 P.S., UNAVCO, GPS/GNSS Observations Dataset, https://doi.org/10.7283/T56M34RJ

UNAVCO Community, 2005, PBO GPS Network – AV15-AKU_EastPtAK2005 P.S., UNAVCO, GPS/GNSS Observations Dataset, https://doi.org/10.7283/T52V2D17

UNAVCO Community, 2005, Alaska GPS Network – EYAC-Eyak Ski Area Continuous P.S., GAGE Facility, GPS/GNSS Observations Dataset, https://doi.org/10.7283/ZW9M-JD12

UNAVCO Community, 2006, PBO GPS Network – AB11-Nome_AnvilAK2006 P.S., UNAVCO, GPS/GNSS Observations Dataset, https://doi.org/10.7283/T5PC30BF

UNAVCO Community, 2006, PBO GPS Network – AB13-ChignikLgnAK2006 P.S., UNAVCO, GPS/GNSS Observations Dataset, https://doi.org/10.7283/T5HQ3WW8

UNAVCO Community, 2006, PBO GPS Network – AB15-Nyac_Gold_AK2006 P.S., UNAVCO, GPS/GNSS Observations Dataset, https://doi.org/10.7283/T5B56GQ4

UNAVCO Community, 2006, PBO GPS Network – AB21-AdakIAleutAK2006 P.S., UNAVCO, GPS/GNSS Observations Dataset, https://doi.org/10.7283/T56Q1V6B

UNAVCO Community, 2006, PBO GPS Network – AB22-IlliamnaHPAK2006 P.S., UNAVCO, GPS/GNSS Observations Dataset, https://doi.org/10.7283/T58G8HNW

UNAVCO Community, 2006, PBO GPS Network – AB28-Rainy_PassAK2006 P.S., UNAVCO, GPS/GNSS Observations Dataset, https://doi.org/10.7283/T56H4FD4

UNAVCO Community, 2006, PBO GPS Network – AB33-Coldfoot__AK2006 P.S., UNAVCO, GPS/GNSS Observations Dataset, https://doi.org/10.7283/T53F4MKT

UNAVCO Community, 2006, PBO GPS Network – AB36-Manley_HotAK2006 P.S., UNAVCO, GPS/GNSS Observations Dataset, https://doi.org/10.7283/T56D5QZZ

UNAVCO Community, 2006, PBO GPS Network – AB41-EagleAirptAK2006 P.S., UNAVCO, GPS/GNSS Observations Dataset, https://doi.org/10.7283/T5Q81B2H

UNAVCO Community, 2006, PBO GPS Network – AB42-Akwe_Peak_AK2006 P.S., UNAVCO, GPS/GNSS Observations Dataset, https://doi.org/10.7283/T5RB72K6

UNAVCO Community, 2006, PBO GPS Network – AB49-KlawockAirAK2006 P.S., UNAVCO, GPS/GNSS Observations Dataset, https://doi.org/10.7283/T5H41PDW

UNAVCO Community, 2006, PBO GPS Network – AC17-DriftRiverAK2006 P.S., UNAVCO, GPS/GNSS Observations Dataset, https://doi.org/10.7283/T5CZ354W

UNAVCO Community, 2006, PBO GPS Network – AC21-PerryvilleAK2006 P.S., UNAVCO, GPS/GNSS Observations Dataset, https://doi.org/10.7283/T5KK98RJ

UNAVCO Community, 2006, PBO GPS Network – AC31-Bald_Head_AK2006 P.S., UNAVCO, GPS/GNSS Observations Dataset, https://doi.org/10.7283/T5MK69VG

UNAVCO Community, 2006, PBO GPS Network – AC32-Mt_SusitnaAK2006 P.S., UNAVCO, GPS/GNSS Observations Dataset, https://doi.org/10.7283/T5ST7MSN

UNAVCO Community, 2006, PBO GPS Network – AC34-OldHarbor_AK2006 P.S., UNAVCO, GPS/GNSS Observations Dataset, https://doi.org/10.7283/T5028PG3

UNAVCO Community, 2006, PBO GPS Network – AC35-PetrofLakeAK2006 P.S., UNAVCO, GPS/GNSS Observations Dataset, https://doi.org/10.7283/T5NK3C08

UNAVCO Community, 2006, PBO GPS Network – AC39-ShuyakIsSPAK2006 P.S., UNAVCO, GPS/GNSS Observations Dataset, https://doi.org/10.7283/T5TT4NX1

UNAVCO Community, 2006, PBO GPS Network – AC41-PortMollerAK2006 P.S., UNAVCO, GPS/GNSS Observations Dataset, https://doi.org/10.7283/T5FX77D3

UNAVCO Community, 2006, PBO GPS Network – AC45-SitkinakIsAK2006 P.S., UNAVCO, GPS/GNSS Observations Dataset, https://doi.org/10.7283/T5JS9NDC

UNAVCO Community, 2006, PBO GPS Network – AC46-Skwentna_RAK2006 P.S., UNAVCO, GPS/GNSS Observations Dataset, https://doi.org/10.7283/T5HH6H1K

UNAVCO Community, 2006, PBO GPS Network – AC53-Willow_CrkAK2006 P.S., UNAVCO, GPS/GNSS Observations Dataset, https://doi.org/10.7283/T5MG7MGM

UNAVCO Community, 2006, PBO GPS Network – AC57-ThompsonPaAK2006 P.S., UNAVCO, GPS/GNSS Observations Dataset, https://doi.org/10.7283/T5FN145P

UNAVCO Community, 2006, PBO GPS Network – AC61-ChickenM61AK2006 P.S., UNAVCO, GPS/GNSS Observations Dataset, https://doi.org/10.7283/T5WS8R73

UNAVCO Community, 2006, PBO GPS Network – AC66-AmchitkaIsAK2006 P.S., UNAVCO, GPS/GNSS Observations Dataset, https://doi.org/10.7283/T5DZ069Q

UNAVCO Community, 2006, PBO GPS Network – AC67-PillarMtn_AK2006 P.S., UNAVCO, GPS/GNSS Observations Dataset, https://doi.org/10.7283/T5Q23X61

UNAVCO Community, 2006, UNAVCO GPS Network – ATQK-Atqasuk P.S., UNAVCO, GPS/GNSS Observations Dataset, https://doi.org/10.7283/T55X2744

UNAVCO Community, 2006, PBO GPS Network – AV11-Augs_MoundAK2006 P.S., UNAVCO, GPS/GNSS Observations Dataset, https://doi.org/10.7283/T52J68T9

UNAVCO Community, 2006, PBO GPS Network – AV16-AugvLagoonAK2006 P.S., UNAVCO, GPS/GNSS Observations Dataset, https://doi.org/10.7283/T5862DDG

UNAVCO Community, 2006, PBO GPS Network – AV17-AugustinNWAK2006 P.S., UNAVCO, GPS/GNSS Observations Dataset, https://doi.org/10.7283/T54F1NPR

UNAVCO Community, 2006, PBO GPS Network – AV18-AugvNorth_AK2006 P.S., UNAVCO, GPS/GNSS Observations Dataset, https://doi.org/10.7283/T50P0X0W

UNAVCO Community, 2006, PBO GPS Network – AV19-AugustinSEAK2006 P.S., UNAVCO, GPS/GNSS Observations Dataset, https://doi.org/10.7283/T5VX0DHK

UNAVCO Community, 2006, PBO GPS Network – AV20-Augs_SouthAK2006 P.S., UNAVCO, GPS/GNSS Observations Dataset, https://doi.org/10.7283/T5KH0K9B

UNAVCO Community, 2007, PBO GPS Network – AB01-AtkaIslandAK2007 P.S., UNAVCO, GPS/GNSS Observations Dataset, https://doi.org/10.7283/T59C6VCZ

UNAVCO Community, 2007, PBO GPS Network – AB02-Nikolski__AK2007 P.S., UNAVCO, GPS/GNSS Observations Dataset, https://doi.org/10.7283/T5X63JX4

UNAVCO Community, 2007, PBO GPS Network – AB04-Savoonga__AK2007 P.S., UNAVCO, GPS/GNSS Observations Dataset, https://doi.org/10.7283/T5X06510

UNAVCO Community, 2007, PBO GPS Network – AB09-Razorback_AK2007 P.S., UNAVCO, GPS/GNSS Observations Dataset, https://doi.org/10.7283/T53J39ZP

UNAVCO Community, 2007, PBO GPS Network – AB12-Platinum__AK2007 P.S., UNAVCO, GPS/GNSS Observations Dataset, https://doi.org/10.7283/T5S75D98

UNAVCO Community, 2007, PBO GPS Network – AB14-DillinghamAK2007 P.S., UNAVCO, GPS/GNSS Observations Dataset, https://doi.org/10.7283/T5HT2M90

UNAVCO Community, 2007, PBO GPS Network – AB18-Kotzebue__AK2007 P.S., UNAVCO, GPS/GNSS Observations Dataset, https://doi.org/10.7283/T51834GZ

UNAVCO Community, 2007, PBO GPS Network – AB27-Kobuk_VallAK2007 P.S., UNAVCO, GPS/GNSS Observations Dataset, https://doi.org/10.7283/T5KK98S0

UNAVCO Community, 2007, PBO GPS Network – AB35-Yakataga__AK2007 P.S., UNAVCO, GPS/GNSS Observations Dataset, https://doi.org/10.7283/T5930R4J

UNAVCO Community, 2007, PBO GPS Network – AB43-CapeSpenceAK2007 P.S., UNAVCO, GPS/GNSS Observations Dataset, https://doi.org/10.7283/T5SF2T6T

UNAVCO Community, 2007, PBO GPS Network – AB46-ArcticVilgAK2007 P.S., UNAVCO, GPS/GNSS Observations Dataset, https://doi.org/10.7283/T5K07285

UNAVCO Community, 2007, PBO GPS Network – AC03-AnchorPnt_AK2007 P.S., UNAVCO, GPS/GNSS Observations Dataset, https://doi.org/10.7283/T5ST7MT3

UNAVCO Community, 2007, PBO GPS Network – AC07-Buckland__AK2007 P.S., UNAVCO, GPS/GNSS Observations Dataset, https://doi.org/10.7283/T5ZS2TGD

UNAVCO Community, 2007, PBO GPS Network – AC08-CapDouglasAK2007 P.S., UNAVCO, GPS/GNSS Observations Dataset, https://doi.org/10.7283/T5HH6H21

UNAVCO Community, 2007, PBO GPS Network – AC14-EstherIsleAK2007 P.S., UNAVCO, GPS/GNSS Observations Dataset, https://doi.org/10.7283/T5T43R2S

UNAVCO Community, 2007, PBO GPS Network – AC16-DeepWater_AK2007 P.S., UNAVCO, GPS/GNSS Observations Dataset, https://doi.org/10.7283/T5PC30CW

UNAVCO Community, 2007, PBO GPS Network – AC23-Soldotna__AK2007 P.S., UNAVCO, GPS/GNSS Observations Dataset, https://doi.org/10.7283/T5000035

UNAVCO Community, 2007, PBO GPS Network – AC24-KingSalmonAK2006 P.S., UNAVCO, GPS/GNSS Observations Dataset, https://doi.org/10.7283/T53R0QX4

UNAVCO Community, 2007, PBO GPS Network – AC37-LakeClark_AK2007 P.S., UNAVCO, GPS/GNSS Observations Dataset, https://doi.org/10.7283/T5RX9920

UNAVCO Community, 2007, PBO GPS Network – AC40-PortHeidenAK2007 P.S., UNAVCO, GPS/GNSS Observations Dataset, https://doi.org/10.7283/T50G3H4S

UNAVCO Community, 2007, PBO GPS Network – AC42-SanakIslndAK2007 P.S., UNAVCO, GPS/GNSS Observations Dataset, https://doi.org/10.7283/T5VX0DJ1

UNAVCO Community, 2007, PBO GPS Network – AC43-Seal_RocksAK2007 P.S., UNAVCO, GPS/GNSS Observations Dataset, https://doi.org/10.7283/T5NC5Z6P

UNAVCO Community, 2007, PBO GPS Network – AC47-SlopeMtn__AK2007 P.S., UNAVCO, GPS/GNSS Observations Dataset, https://doi.org/10.7283/T5N58JC1

UNAVCO Community, 2007, PBO GPS Network – AC48-NakedIsl__AK2007 P.S., UNAVCO, GPS/GNSS Observations Dataset, https://doi.org/10.7283/T5959FKR

UNAVCO Community, 2007, PBO GPS Network – AC50-BaldyMtn__AK2007 P.S., UNAVCO, GPS/GNSS Observations Dataset, https://doi.org/10.7283/T5W093W6

UNAVCO Community, 2007, PBO GPS Network – AC51-StrandlineAK2007 P.S., UNAVCO, GPS/GNSS Observations Dataset, https://doi.org/10.7283/T5GM859H

UNAVCO Community, 2007, PBO GPS Network – AC52-PilotPointAK2007 P.S., UNAVCO, GPS/GNSS Observations Dataset, https://doi.org/10.7283/T5ZP444C

UNAVCO Community, 2008, PBO GPS Network – AB17-UnalakleetAK2008 P.S., UNAVCO, GPS/GNSS Observations Dataset, https://doi.org/10.7283/T5PR7T06

UNAVCO Community, 2008, PBO GPS Network – AB25-Tatalina__AK2008 P.S., UNAVCO, GPS/GNSS Observations Dataset, https://doi.org/10.7283/T58G8HPB

UNAVCO Community, 2008, PBO GPS Network – AB39-FortYukon_AK2008 P.S., UNAVCO, GPS/GNSS Observations Dataset, https://doi.org/10.7283/T5SB43R1

UNAVCO Community, 2008, PBO GPS Network – AB45-SagRivrDOTAK2007 P.S., UNAVCO, GPS/GNSS Observations Dataset, https://doi.org/10.7283/T5PR7SZB

UNAVCO Community, 2008, PBO GPS Network – AC10-CpSarichefAK2008 P.S., UNAVCO, GPS/GNSS Observations Dataset, https://doi.org/10.7283/T51N7Z4Q

UNAVCO Community, 2008, PBO GPS Network – AC12-ChernaburaAK2008 P.S., UNAVCO, GPS/GNSS Observations Dataset, https://doi.org/10.7283/T5NV9G7P

UNAVCO Community, 2008, PBO GPS Network – AC13-ChirikofIsAK2008 P.S., UNAVCO, GPS/GNSS Observations Dataset, https://doi.org/10.7283/T5F18WRV

UNAVCO Community, 2008, PBO GPS Network – AC18-Ushagat_IsAK2008 P.S., UNAVCO, GPS/GNSS Observations Dataset, https://doi.org/10.7283/T57H1GKZ

UNAVCO Community, 2008, PBO GPS Network – AC19-FarewellMtAK2008 P.S., UNAVCO, GPS/GNSS Observations Dataset, https://doi.org/10.7283/T5HQ3WXQ

UNAVCO Community, 2008, PBO GPS Network – AC26-Cape_Gull_AK2008 P.S., UNAVCO, GPS/GNSS Observations Dataset, https://doi.org/10.7283/T58P5XJF

UNAVCO Community, 2008, PBO GPS Network – AC28-NagaiIslndAK2008 P.S., UNAVCO, GPS/GNSS Observations Dataset, https://doi.org/10.7283/T53N21DV

UNAVCO Community, 2008, PBO GPS Network – AC33-TokoDenaliAK2007 P.S., UNAVCO, GPS/GNSS Observations Dataset, https://doi.org/10.7283/T5JD4TSP

UNAVCO Community, 2008, PBO GPS Network – AC36-MoosePointAK2008 P.S., UNAVCO, GPS/GNSS Observations Dataset, https://doi.org/10.7283/T5RV0KQQ

UNAVCO Community, 2008, PBO GPS Network – AC44-ArcticVly_AK2008 P.S., UNAVCO, GPS/GNSS Observations Dataset, https://doi.org/10.7283/T5HT2MBF

UNAVCO Community, 2008, PBO GPS Network – AC58-StPaulIsldAK2008 P.S., UNAVCO, GPS/GNSS Observations Dataset, https://doi.org/10.7283/T55D8PV1

UNAVCO Community, 2008, PBO GPS Network – AC60-Westeast__AK2008 P.S., UNAVCO, GPS/GNSS Observations Dataset, https://doi.org/10.7283/T5CZ355B

UNAVCO Community, 2008, PBO GPS Network – AC76-LogCabin__AK2008 P.S., UNAVCO, GPS/GNSS Observations Dataset, https://doi.org/10.7283/T5RN35VM

UNAVCO Community, 2008, PBO GPS Network – AV24-WestdahlNWAK2008 P.S., UNAVCO, GPS/GNSS Observations Dataset, https://doi.org/10.7283/T5F769KW

UNAVCO Community, 2008, PBO GPS Network – AV25-WestdahlW_AK2008 P.S., UNAVCO, GPS/GNSS Observations Dataset, https://doi.org/10.7283/T51Z42DH

UNAVCO Community, 2008, PBO GPS Network – AV26-WestdahlNEAK2008 P.S., UNAVCO, GPS/GNSS Observations Dataset, https://doi.org/10.7283/T59G5JTQ

UNAVCO Community, 2008, PBO GPS Network – AV27-WestdahlSWAK2008 P.S., UNAVCO, GPS/GNSS Observations Dataset, https://doi.org/10.7283/T55Q4T3D

UNAVCO Community, 2008, PBO GPS Network – AV29-WestdahlSEAK2008 P.S., UNAVCO, GPS/GNSS Observations Dataset, https://doi.org/10.7283/T5X63JZK

UNAVCO Community, 2008, PBO GPS Network – AV34-IsanotskiSAK2008 P.S., UNAVCO, GPS/GNSS Observations Dataset, https://doi.org/10.7283/T5V122T8

UNAVCO Community, 2008, PBO GPS Network – AV35-TugamakRngAK2008 P.S., UNAVCO, GPS/GNSS Observations Dataset, https://doi.org/10.7283/T5K0729M

UNAVCO Community, 2008, PBO GPS Network – AV36-ShshldinNWAK2008 P.S., UNAVCO, GPS/GNSS Observations Dataset, https://doi.org/10.7283/T53F4MNQ

UNAVCO Community, 2008, PBO GPS Network – AV37-ShshldinSWAK2008 P.S., UNAVCO, GPS/GNSS Observations Dataset, https://doi.org/10.7283/T5ZS2THV

UNAVCO Community, 2008, PBO GPS Network – AV38-IsanotskiNAK2008 P.S., UNAVCO, GPS/GNSS Observations Dataset, https://doi.org/10.7283/T5765CB0

UNAVCO Community, 2008, PBO GPS Network – AV39-ShishaldinAK2008 P.S., UNAVCO, GPS/GNSS Observations Dataset, https://doi.org/10.7283/T5Q81B3Z

UNAVCO Community, 2008, PBO GPS Network – AV40-BrownPeak_AK2008 P.S., UNAVCO, GPS/GNSS Observations Dataset, https://doi.org/10.7283/T5NS0RWD

UNAVCO Community, 2008, PBO GPS Network – WIKR-Wicker84K_AK2008 P.S., UNAVCO, GPS/GNSS Observations Dataset, https://doi.org/10.7283/T52805NS

UNAVCO Community, 2009, PBO GPS Network – AB08-Mekoryuk__AK2008 P.S., UNAVCO, GPS/GNSS Observations Dataset, https://doi.org/10.7283/T5D50K09

UNAVCO Community, 2009, PBO GPS Network – AC09-KayakIsl__AK2007 P.S., UNAVCO, GPS/GNSS Observations Dataset, https://doi.org/10.7283/T59Z92W5

UNAVCO Community, 2009, PBO GPS Network – AC78-Tetlin_2__AK2009 P.S., UNAVCO, GPS/GNSS Observations Dataset, https://doi.org/10.7283/T5862DFX

UNAVCO Community, 2010, PBO GPS Network – AC79-Montague2_AK2010 P.S., UNAVCO, GPS/GNSS Observations Dataset, https://doi.org/10.7283/T54F1NRN

UNAVCO Community, 2010, PBO GPS Network – AC80-YentnaRvr2AK2010 P.S., UNAVCO, GPS/GNSS Observations Dataset, https://doi.org/10.7283/T50P0X2S

UNAVCO Community, 2011, PBO GPS Network – AB53-CrystalMtnAK2011 P.S., UNAVCO, GPS/GNSS Observations Dataset, https://doi.org/10.7283/T5W37TB0

UNAVCO Community, 2014, PBO GPS Network – AC29-middleton_AK2014 P.S., UNAVCO, GPS/GNSS Observations Dataset, https://doi.org/10.7283/T5VH5M6S

UNAVCO Community, 2014, UNAVCO GPS Network – BARO-Barrow_Arctic_RC P.S., UNAVCO, GPS/GNSS Observations Dataset, https://doi.org/10.7283/T5CF9NDC

UNAVCO Community, Freymueller, Jeffrey T., 1998, Alaska GPS Network – CLGO-College Observatory P.S., UNAVCO, GPS/GNSS Observations Dataset, https://doi.org/10.7283/T5JH3J7V